QUANTUM TRANSPORT IN SEMICONDUCTOR NANOSTRUCTURES

by

Shicheng Lu

Bachelor of Science, Nanjing University, 2006

Master of Science, Nanjing University, 2009

Submitted to the Graduate Faculty of

the Kenneth P. Dietrich School of Arts and Sciences in partial fulfillment

of the requirements for the degree of

Doctor of Philosophy

University of Pittsburgh

2016

UNIVERSITY OF PITTSBURGH

KENNETH P. DIETRICH SCHOOL OF ARTS AND SCIENCES

This thesis was presented

by

Shicheng Lu

It was defended on

November. 4, 2015

and approved by

Andrew Daley, Professor, Department of Physics

Brian D'Urso, Assistant Professor, Department of Physics and Astronomy

Geoffrey Hutchison, Assistant Professor, Department of Chemistry

Vittorio Paolone, Associate Professor, Department of Physics and Astronomy

Thesis Director: Jeremy Levy, Professor, Department of Physics and Astronomy

QUANTUM TRANSPORT IN SEMICONDUCTOR NANOSTRUCTURES

Shicheng Lu, PhD

University of Pittsburgh, 2016

QUANTUM TRANSPORT IN SEMICONDUCTOR NANOSTRUCTURES

Shicheng Lu, PhD

University of Pittsburgh, 2016

Advances in complex oxide heterostructures have opened up a novel era in material sciences, and subsequently driven extensive physical research efforts to explore the underlying mechanisms. Material systems show a wide variety of phenomena such as superconductivity, magnetism, ferroelectricity, and spin-orbit coupling, all of which are gate-tunable. This facet demonstrates their significant importance, not only for science and research, but also for their substantial technological applications. One of the most promising systems is the $LaAlO_3/SrTiO_3$ heterostructure in which several unit cells of $LaAlO_3$ are deposited on TiO_2-terminated $SrTiO_3$, giving rise to a two dimensional electron liquid (2DEL) at the interface region. In the case of 3-unit-cell (3 u.c.) $LaAlO_3/SrTiO_3$ interfaces, a conductive atomic force microscope (c-AFM) tip can be utilized to "write" and "erase" nanoscale devices, making $LaAlO_3/SrTiO_3$ a highly flexible platform application in novel nanoelectronics. In this thesis, the c-AFM lithography technique was employed to create various nanostructures at the $LaAlO_3/SrTiO_3$ interface. In parallel, their corresponding properties were also thoroughly investigated using quantum transport methods. Specifically, the mobility of these created nanostructures was investigated, and it was found that the mobility could be significantly enhanced in a 1D constrain configuration compared to the scenario of 2D structures. Nonlocal transport measurements were also performed on $LaAlO_3/SrTiO_3$ Hall bar structures in both normal state, and superconducting state. A novel transport property was revealed, and this property could be due to the spin and quasi-particles. Additionally, it is of note that quantum dot-like and quantum point-contact-like structures can be

created via intentionally introducing barriers at the interface in $LaAlO_3/SrTiO_3$ nanowires. This can lead to various phenomena, such as electron paring without superconductivity, and conductance plateaus in transport measurements. The demonstrated c-AFM technique was also applied to a similar $Al_2O_3/SrTiO_3$ material system, in which conducting channels were created at the interface. These channels show extremely high mobility at low temperature(s).

TABLE OF CONTENTS

LIST OF TABLES

LIST OF FIGURES

PREFFACE

This thesis is submitted for the degree of Doctor of Philosophy at the University of Pittsburgh. The research described here was conducted under the supervision of Professor Jeremy Levy in the department of Physics & Astronomy, University of Pittsburgh between May 2011 and November 2015.

This thesis is also the summary of my five years' physics Ph.D. life which has been a challenging trip. Fortunately, I was not alone on this road, as I was accompanied by an excellent team of experts who were and are always willing to help, sponsor and motivate me. For this, I would like to kindly thank them.

The most important person throughout all these years was Jeremy Levy. He is full of knowledge and ideas, and always willing to share them. I really appreciate the opportunity to work in his laboratory. I would never have arrived at this point without his patient guidance, hand-by-hand help, and five years of support.

I also would like to thank all my lab mates including Patrick Irvin, Guanglei Cheng, Dongyue Yang, Anil Annadi, Feng Bi, Mengchen Huang, Michelle Tomczyk, and Megan Kirkendall. They worked with me on various projects, helped me to learn lab instruments, taught me lab skills and gave me comments on my manuscripts. It was such as nice lab environment that allowed me to advance to graduation.

I also want to express my gratitude to my committee members, Andrew Daley, Brian D'Urso, Geoffrey Hutchison, and Vittorio Paolone. Their comments and suggestions guided me on my path of PhD studies.

Finally, I owe special thanks to my parents for their support and encouragement during my PhD studies.

1.0 INTRODUCTION

The semiconductor device-based modern electronic industry has been growing rapidly for decades. Semiconductor devices include different kinds of transistors, solar cells, diodes, and digital and analog integrated circuits. The keystone for all of these devices are III-V semiconductors such as silicon and germanium, which contain band structures that can be manipulated by doping with impurities. An external electrical field can also be used to change their conductivity, making these semiconductors ideal for fabricating electronic devices. However, the feature size of current semiconductor devices (~14 nm) is approaching the limitation of Moore's Law. Hence, there is the demand for alternative material systems with the capabilities of larger integration densities and more functionality.

One candidate for these next-generation electronic platforms is complex oxides, which possess a great variety of emergent properties such as a tunable metal-insulator transitions, superconductivity, spin-orbit coupling, ferroelectricity, ferromagnetism, high dielectric constants, and colossal magnetoresistance. Oxide material systems may exhibit some or all of these exotic properties which makes them not only an exciting research material system, but also attractive for industrial applications.

This thesis focuses on one of the most interesting complex-oxide material systems: $LaAlO_3/SrTiO_3$ ($LaAlO_3/SrTiO_3$). The background regarding the methods and mechanisms used to create nanodevices on a $LaAlO_3/SrTiO_3$ interface, and the resulting nanodevice transport properties, will be presented in the following sections. Additionally, studies on another similar material system, $Al_2O_3/SrTiO_3$, will also be discussed.

1.1 LAAlO$_3$/SRTIO$_3$ INTERFACE

Two wide, indirect-band, gap-insulators, $LaAlO_3$ ($E_{gap}^{LAO} = 5.6$ eV) and $SrTiO_3$ ($E_{gap}^{STO} = 3.2$ eV), have close lattice constants ($LaAlO_3 \approx 3.789$ Å and $SrTiO_3 \approx 3.905$ Å) which allow them to match with each other when grown on top of one another. A high-mobility, two-dimensional electron liquid (2DEL) can form at the interface of polar $LaAlO_3$ when grown on a non-polar $SrTiO_3$ substrate, first reported by Ohtomo *et al.* (2004)[1]. Such a conducting interface shows a typical 2D carrier density[2,3] of 10^{12}-10^{13} cm^{-2}, higher than that in III-V semiconductor heterostructures (10^{10}-10^{12} cm^{-2}). Additionally, the mobility of electrons at the $LaAlO_3/SrTiO_3$ interface can be as high as 10,000 cm^2/Vs at low temperature (T = 4 K)[1]. And, confining the 2DEL into a 1D conducting channel[4] can enhance the mobility to ~ 20,000 cm^2/Vs at low temperature.

1.2 MATERIAL GROWTH

Advances in new material growth techniques such as pulsed laser deposition[5] (PLD) and molecular beam epitaxy[6] now allow precisely-tailored complex-oxide heterostructures to be possible. In 2004, Ohtomo *et al.*[1] first successfully synthesized a $LaAlO_3/SrTiO_3$ heterostructure in an ultrahigh vacuum chamber with PLD[1], the primary method used to grow $LaAlO_3$ thin films on $SrTiO_3$ substrates. $LaAlO_3/SrTiO_3$ heterostructures have also been fabricated by other methods such as molecular beam epitaxy[7], sputtering[8], and atomic layer deposition[9]. $LaAlO_3/SrTiO_3$

samples for this thesis were grown via PLD by our collaborator Chang Beom Eom's group at the University of Wisconsin-Madison (Wisconsin, United States) and Yuri Suzuki's group at the University of California, Berkeley (Berkeley, United States). The detailed sample growth steps are described below.

Before deposition TiO_2-terminated $SrTiO_3$ substrates with low-angle (<0.1°) miscuts are etched with buffered hydrofluoric (HF) acid. Then the substrates are annealed at 1000 °C for several hours to create atomically flat surfaces. During the deposition, ultrathin layers of epitaxial $LaAlO_3$ are grown on $SrTiO_3$ substrates by a PLD equipped with reflection high-energy electron diffraction (RHEED), which allows the precise control of the growth thickness. A high power (λ = 248 nm) KrF exciter laser beam is focused on a single stoichiometric $LaAlO_3$ target crystal with an energy density of 1.5 J/cm^2. The laser pulses ablate the $LaAlO_3$ target, and the ejected material is deposited onto the $SrTiO_3$ substrates. Figure 1-1a shows the RHEED intensity plot during $LaAlO_3/SrTiO_3$ sample growth, where the three oscillations in the curve indicate that the $LaAlO_3$ thickness is three unit cells. Two different growth conditions are used: (1) the substrate growth temperature at T = 550 °C and the chamber background partial oxygen pressure at $P(O_2) = 10^{-3}$ mbar; and (2) T = 780 °C and $P(O_2) = 10^{-5}$ mbar. (2) after deposition they are annealed at 600 °C in $P(O_2)$ = 300 mbar for one hour to minimize oxygen vacancies. After this treatment, the grown $LaAlO_3/SrTiO_3$ sample exhibits an atomically flat surface as shown in Figure 1-1b, where the terraces are the single unit cell height steps. Figure 1-1c shows the surface height profile along the red line cut, from which the step height can be estimated as ~ 4 Å.

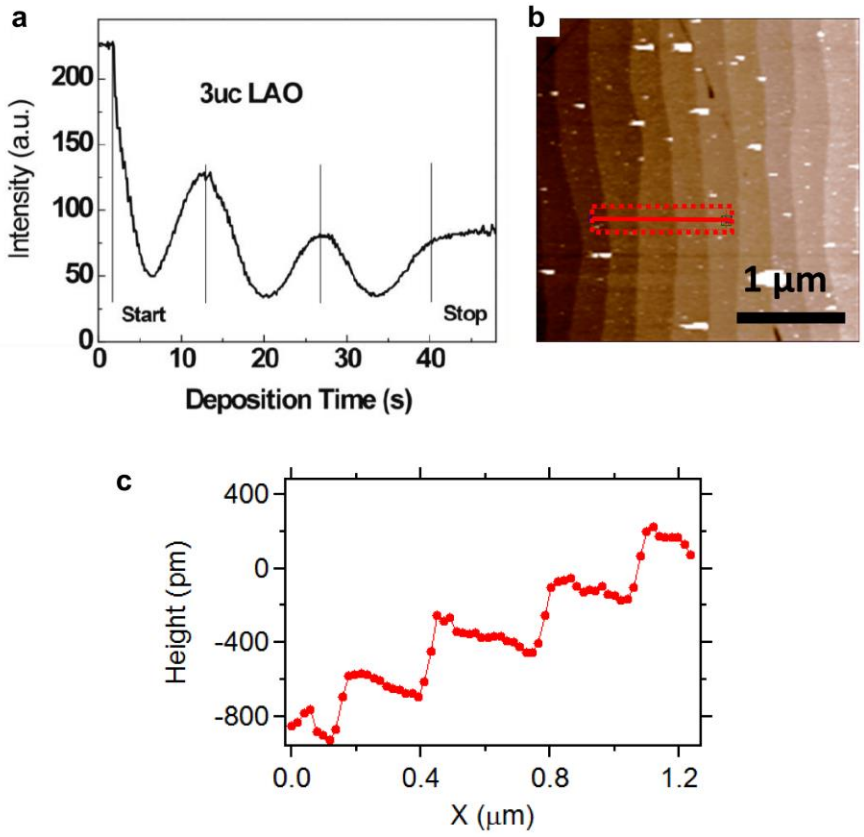

Figure 1-1 PLD growth of $LaAlO_3$ layers on $SrTiO_3$ substrate. (a), RHEED intensity oscillations during $LaAlO_3$ film growth. The peaks marked by the vertical lines indicate each complete $LaAlO_3$ unit cell is deposited (Data provided by collaborator Prof. Chang-Beom Eom's group). (b), AFM height image of $LaAlO_3$ surface, showing the surface is atomically flat. (c), Height profile along the red line cut in (b).

1.3 POSSIBLE ORIGIN OF QUASI-2DEL

Although at the writing of this thesis, it has been roughly twelve years since the first $LaAlO_3/SrTiO_3$ conducting interface was reported, the origin of the observed 2DEL is still debated. Several mechanisms have been proposed to explain the formation of the 2DEL.

A very popular mechanism called "polar catastrophe" describes an intrinsic electron reconstruction process within $LaAlO_3/SrTiO_3$.[10] As shown in Figure 1-2a, the $SrTiO_3$ substrate is a non-polar material with the $Ti^{4+}O^{2-}{}_2$ and $Sr^{2+}O^{2-}$ planes at charge neutral. However, when polar material $LaAlO_3$ is epitaxially grown on $SrTiO_3$, net charge +e/-e formed at $La^{3+}O^{2-}$ and $Al^{3+}O^{2-}{}_2$ planes respectively. When they alternatively stack together, the polar discontinuity at the interface leads to a built-in electric potential which diverges with increasing $LaAlO_3$ thickness. When the $LaAlO_3$ thickness reaches a critical value, in order to screen the built-in polarization, electrons transfer from the $LaAlO_3$ surface to the interface. Figure 1-2a also shows a schematic of the $LaAlO_3/SrTiO_3$ band diagram. The potential difference of the valance band across $LaAlO_3$ increases with $LaAlO_3$ thickness. When a critical thickness is reached, the valance band crosses the Fermi level, and a conducting 2DEL form at the interface.

Another popular mechanism is related the defects in $LaAlO_3/SrTiO_3$. One explanation regards the oxygen vacancies formed in $LaAlO_3$ and $SrTiO_3$ (Figure 1-2b), mostly during the material growth and post annealing. [1,11,12] The oxygen vacancies could serve as donors and provide electrons to form the conducting interface.[12] Another possible explanation is that cations intermix across the interface (Figure 1-2c). The equivalent exchange of La^{3+} and Sr^{2+} near the interface locally dopes the $SrTiO_3$ and could generate the 2DEL.[13] Interfacial sharpness studies by TEM[10] and XRD[14] indicate such intermixing could play an important role in the 2DEL formation.

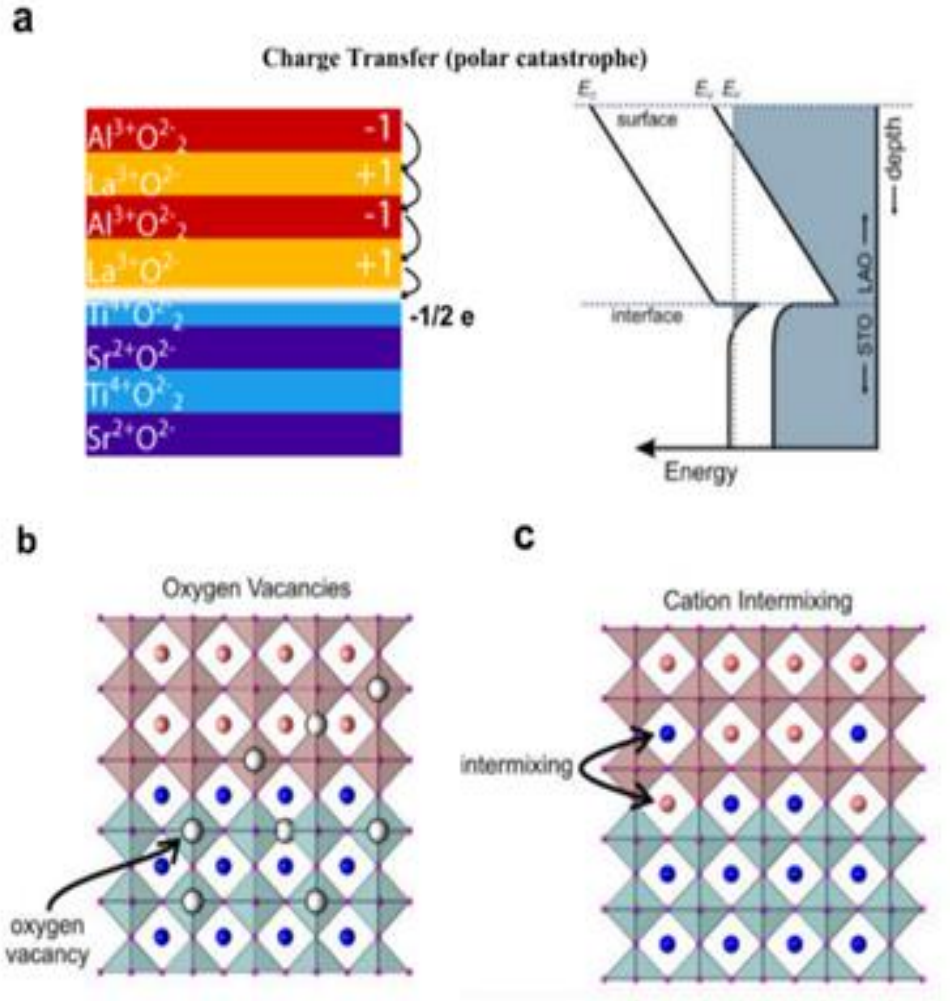

Figure 1-2 Mechanism for interfacial conductivity in $LaAlO_3/SrTiO_3$ (Adapted from Ref. 10 and Ref. 15). (a), polar catastrophe: for $LaAlO_3$ grown on a (100) TiO_2–terminated $SrTiO_3$ substrate, each LaO^{+1} and AlO^{-1} layer has net charge (+*e* and –*e* respectively). Such a stack of the polar layers (LaO^{+1} and AlO^{-1}) increases the built-in potential as the $LaAlO_3$ thickness increases. When the $LaAlO_3$ layer exceeds a critical thickness (3 u.c.), electron reconstruction occurs under a sufficiently large built-in potential, resulting in electrons transferring from the surface to the interface. The left figure in (a) shows the charge transfer process, where a half electron per unit cell transfers to the interface. The right figure in (a) is the schematic of the energy bands, showing the 2DEL confined at the interface between $LaAlO_3$ and $SrTiO_3$. (b), oxygen vacancies act as donors, providing charge to populate the

conducting interface. (c), cation intermixing: the Sr atoms and La atoms near the interface could swap positions, and dope the interface.

1.4 PROPERTIES OF $LAALO_3/SRTIO_3$ HETEROSTRUCTURE

Emergent properties found at $LaAlO_3/SrTiO_3$ interface include a tunable metal-insulator transition[16,17], strong Rashba-like spin-orbit coupling[18,19], superconductivity[20,21] and ferromagnetism, covering almost all the fascinating and exotic functionalities in oxide semiconductors, which makes $LaAlO_3/SrTiO_3$ interface attract widespread interest.

1.4.1 Tunable Metal-Insulator Transition

The modulation of the $LaAlO_3/SrTiO_3$ interface conductivity can be achieved by changing the $LaAlO_3$ thickness or the external electric field which is called tunable metal-insulator transition. [16] Figure 1-3a shows the $LaAlO_3$ thickness dependence of the $LaAlO_3/SrTiO_3$ interfacial conductivity. Below critical thickness value d_c= 3 u.c., the interface is insulating, while above d_c, the interface becomes conducting. Interestingly, for 3 u.c. $LaAlO_3/SrTiO_3$, this metal-insulator transition can be tuned by applying a sufficiently large d_c bias to the back of the $SrTiO_3$ substrate (Figure 1-3b). Gate-tuned metal-insulator transitions show hysteretic behavior which means such a transition can persist even after the back-gating is removed.

1.4.2 Interfacial Superconductivity

In 2007, N. Reyren *et al.*[20] reported a superconducting phase in a $LaAlO_3/SrTiO_3$ heterostructure (Figure 1-3c) with a measured transition temperature, $T_c \approx 200$ mK, and an estimated thickness of the superconducting layer at ~ 10 nm. Further research by Caviglia *et al.*[21] showed that an electric field can control the transition of the interfacial superconductor-insulator quantum phase.

1.4.3 Strong Rashba Spin-orbit Coupling

Rashba Spin-orbit Coupling[22] in two-dimensional electron systems is a momentum dependent spin splitting, usually caused by symmetry breaking which is predicted to occur along the direction perpendicular to the two-dimensional plane. Large spin-orbit coupling was found at the $LaAlO_3/SrTiO_3$ interface in 2010,[19] and its magnitude can be modulated by an external electric field (Figure 1-3d). The study also revealed a steep rise in Rashba interaction, where a quantum critical point separates the insulating and superconducting states of the system.

1.4.4 Interfacial Magnetism and Its Coexistence with Superconductivity

Brinkman *et al.*[23] initiated the magnetism study of $LaAlO_3/SrTiO_3$ by performing magneto-transport measurements, he found that although both $LaAlO_3$ and $SrTiO_3$ are non-magnetic materials, the $LaAlO_3/SrTiO_3$ interface shows magnetic signatures in many experiments, like their transport measurements show a Kondo-like temperature dependence of the resistance (Figure 1-3e) demonstrating the presence of magnetic scattering at the interface. Following experiments which

utilized DC scanning quantum interference device (SQUID) magnetometry[24,25], torque magnetometry[26] and X-ray circular dichroism measurements[27], the data suggest such magnetism is intrinsic, and even persists at temperatures up to and including standard room temperature.

More interestingly, in the $LaAlO_3/SrTiO_3$ system, evidence shows that superconductivity and ferromagnetism can coexist (Figure 1-3f) [24,26,28], It is most likely that magnetism and superconductivity can coexist at the interface but in different areas.

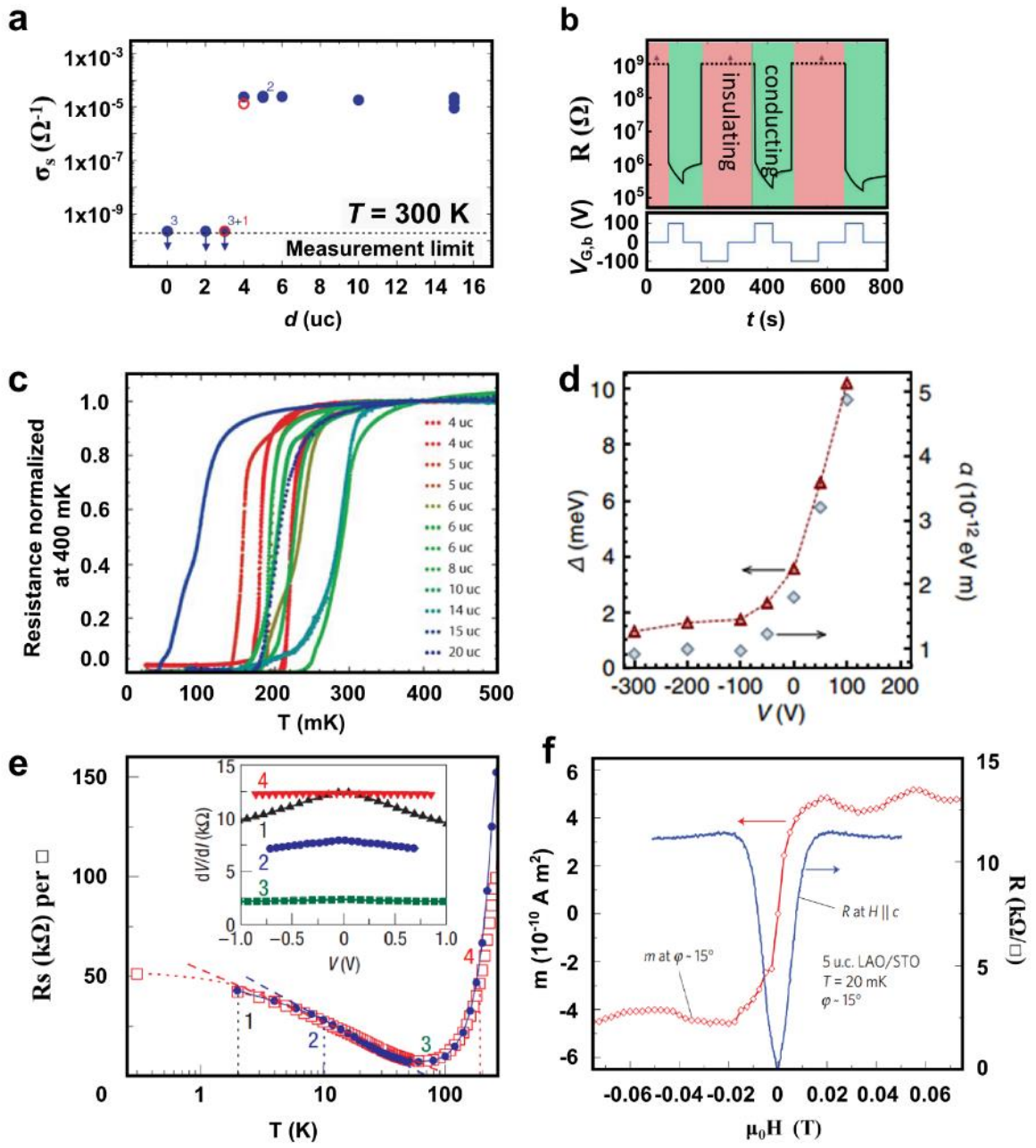

Figure 1-3 Emergent properties of $LaAlO_3/SrTiO_3$ interface. (a), Thickness dependence of interfacial conductivity (Adapted from Ref. 16). (b), Back gate tuning of a 3 u.c. $LaAlO_3/SrTiO_3$ interface through metal-insulator transitions (Adapted from Ref. 16). (c), Superconductivity of the $LaAlO_3/SrTiO_3$ interface at low temperature. (Adapted from Ref. 20). (d), The red curve represents the spin-orbit energy versus the gate voltage, showing that the

size of spin-orbit splitting can be tuned by an electric field. The grey curve shows the field effect modulation of the Rashba coupling constant α (Adapted from Ref. 19). (e), Temperature dependence of the $LaAlO_3/SrTiO_3$ sheet resistance. (Adapted from Ref. 23). (f), Coexistence of superconductivity and magnetic ordering in a 5 u.c. $LaAlO_3/SrTiO_3$ interface. (Adapted from Ref. 26).

2.0 EXPERIMENTAL METHOD

In this section, I will introduce some routinely used experimental techniques during our study of $LaAlO_3/SrTiO_3$ interface structures.

2.1 LAALO$_3$/SRTIO$_3$ SAMPLE FABRICATION

The $LaAlO_3/SrTiO_3$ samples used in this work were grown using pulsed-laser deposition (PLD). Photolithography, ion etching, and DC sputtering techniques are used to pattern electrode contacts on $LaAlO_3/SrTiO_3$ samples.

Figure 2-1 illustrates all steps associated with the fabrication of samples. The electrode design is patterned by the conventional photolithography method (Figure 2-1a-c). During the process, the photoresist (AZ P4210) is first coated uniformly (~2 μm thickness) on the $LaAlO_3/SrTiO_3$ surface using the spin-coat method (Figure 2-1a), and then soft baked for one minute at 90°C. The sample, with photoresist and a covered photomask, is then exposed in UV light (λ = 365 nm) (Figure 2-1b), which can transfer the predesigned pattern onto the photoresist layer. After UV exposure, the pattern can be developed by soaking the sample in the developer (AZ 400k), and dissolves the exposed area (Figure 2-1c). The sample with the patterned photoresist is then etched by a high energy (2 keV) Ar-ion beam to remove the $SrTiO_3$ outside the pattern area with the help of the photoresist (Figure 2-1d). After ion milling, metal deposition is performed using the DC sputtering deposition method (Figure 2-1e). First, a thin Ti layer (5 nm) is deposited on sample surface, which serves as an adhesive layer. Then a thicker Au layer (25 nm) is added

above Ti layer, making an Ohmic contact to the $LaAlO_3/SrTiO_3$ interface. After the sputtering deposition, the sample is immersed in acetone and experiences ultrasonic cleaning for several minutes. The metal that rests on the photoresist is washed away since the photoresist dissolves in acetone, leaving only the patterned electrodes (Figure 2-1f).

Figure 2-2 shows a typical processed 5mm × 5mm sample. The electrodes on the sample surface contact the $LaAlO_3/SrTiO_3$ interface and define the 30 μm × 30 μm canvas for conductive AFM lithography experiments. Gold wires are used to make connections with a wire bonding machine to obtain electrical access to the sample[29]. (Figure 2-2b).

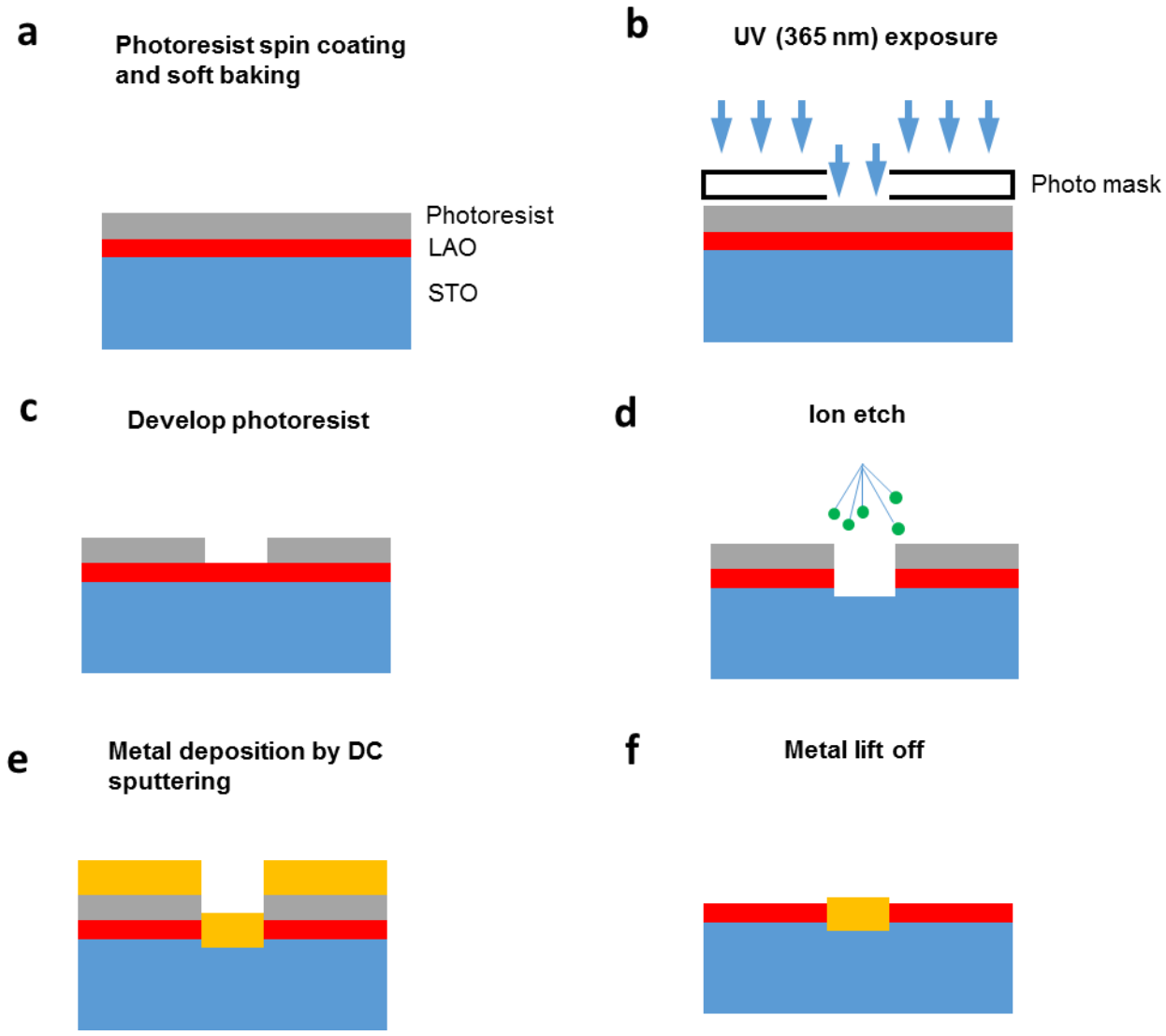

Figure 2-1 Illustration of the steps to make electrodes that contact to the $LaAlO_3/SrTiO_3$ interface. (a), Photoresist spin coat and soft bake. (b), UV exposure using Hg lamp I-line (365 nm). (c), Photoresist development step: for positive photoresist, the exposed areas will dissolve in developer. (d), Ion milling step: high energy Ar^+ etches away the material. (e), Metal deposition using DC sputtering deposition method. (f), Photoresist lift off step: strips off the photoresist and the metal upon it.

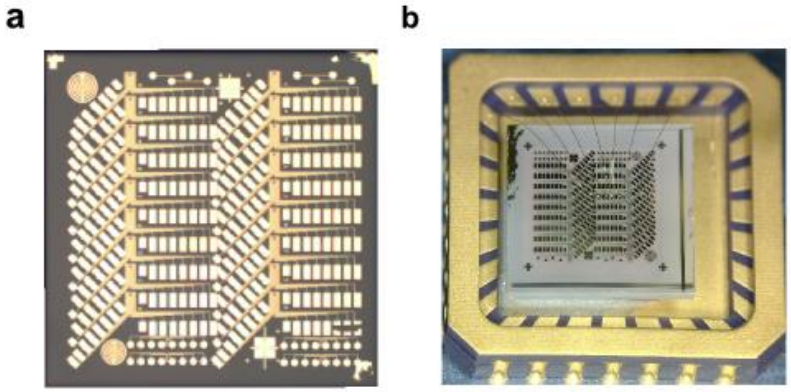

Figure 2-2 Fabricated devices on $LaAlO_3/SrTiO_3$. (Adapted from Ref. 29) (a), Fabricated electrodes on a 3 u.c. $LaAlO_3/SrTiO_3$: the $LaAlO_3/SrTiO_3$ size is 5 mm by 5 mm. (b), Sample, with devices, is glued on the chip carrier using silver epoxy and the electrical connections to the fabricated patterns are made by gold wires by using wire bonding machine.

2.2 ATOMIC FORCE MICROSCOPY (AFM)

Atomic force microscopy (AFM) was invented by Binnig, Quate and Gerber in 1986[30]. Since then AFM become a very powerful and high-resolution type of scanning probe microscopy. It can resolve molecules[31] on a sample surface and even achieve atomic resolution[32] by the fact that AFM tip can interact with an individual atom. Now, AFM is a very important tool to nano-scale science not only because it's imaging capability, but also it can be used for other variety of force sensing, lithography, nanomanipulation, and nanoindentation. Additionally, ultra-fast scanning (>100 Hz/line[33]), and multi-probe techniques (>10 million tips[34]) were also developed to increase the throughput of AFM, providing wider applications for industry.

2.3 AFM WORKING PRINCIPLE

AFM uses a cantilever where laser beam focused and reflected with a sharp tip (the radius of curvature ρ ~ nm affects the AFM resolution) at its end to scan the surface. When the tip is scanning the sample surface, forces between the tip and the sample cause the cantilever to deflect; this deflection can be detected by measuring the reflection laser by a quad photodiode. The analog output of the photodiodes is then input to a digit signal processor (DSP) that generates real time feedback signals. Depending on the tip-sample interaction, AFM can measure the mechanical contact, electrostatic forces, van der Waals forces, magnetic forces, capillary forces, chemical bonding, Casimir forces, and solvation forces. Two types of scanning mode are common, contact mode and non-contact mode. Contact-mode AFM was developed for one of the AFM basic functions: to measure the topography of a sample. In contact mode, the cantilever is usually soft and the tip directly contacts the sample surface. The overall force between tip and sample is repulsive, and is indicated as the red region in the force-distance curve (Figure 2-3).

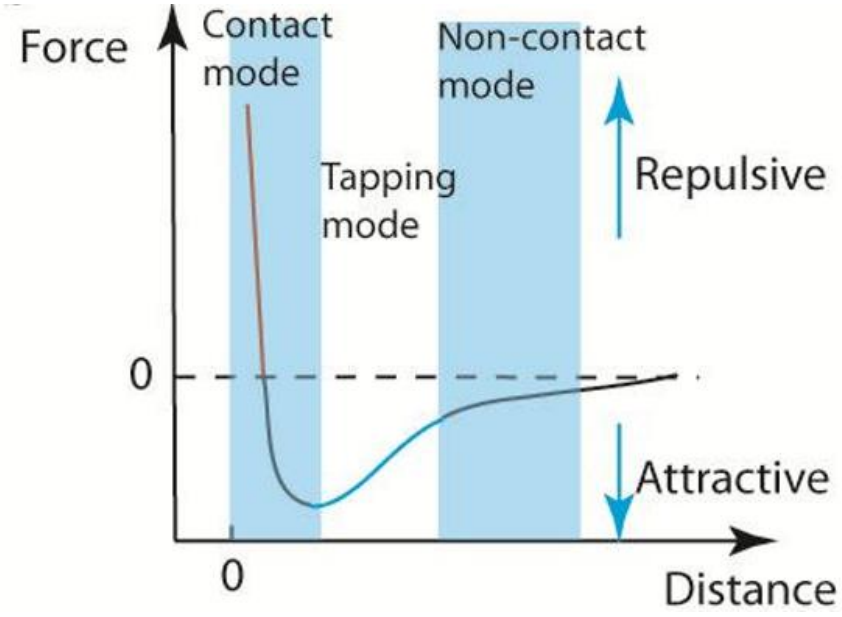

Figure 2-3 Illustration of force-distance curve and corresponding AFM image modes.

Figure 2-4 shows the schematic diagram of the contact-mode AFM operation. When the tip engages on a sample surface, according to Hooke's law, the force between the tip and the sample is:

$$F = -k \cdot D \tag{2-1}$$

where k is the cantilever's spring constant and D is the deflection distance. During the scan, F is kept constant by adjusting the height using the deflection signal as a feedback. Then the surface topography is constructed by spatially mapping the Z piezo height change during the scan.

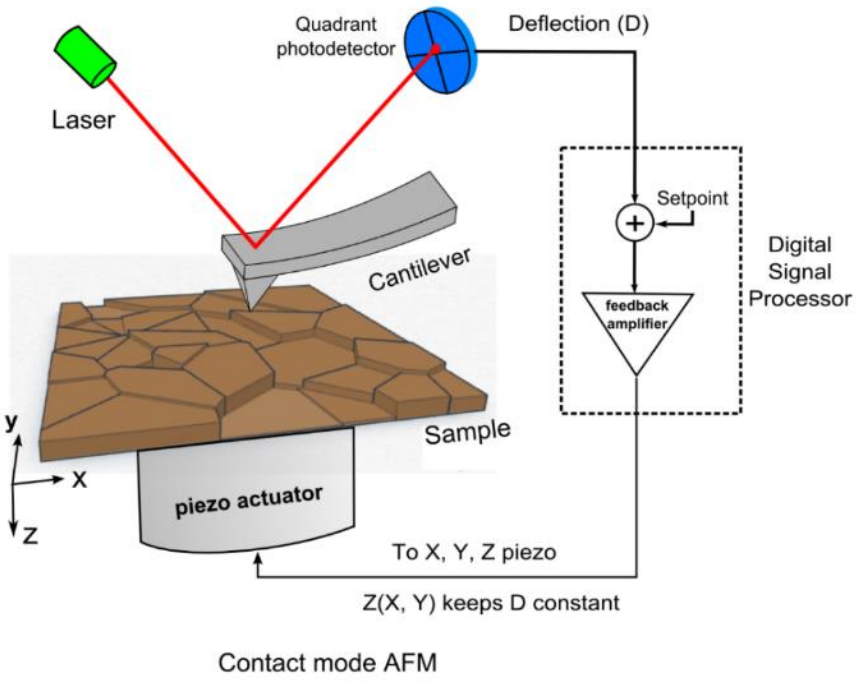

Figure 2-4 Schematic diagram of the essential components for contact mode AFM. (Adapted from Ref. 29)

Figure 2-5 shows the AC mode AFM operation. In this mode, the cantilever is vibrating all the time instead of touching the sample surface. When the tip is moving on the sample surface,

atomic force can dampen the vibrating which can be used as feedback and map out the surface profile.

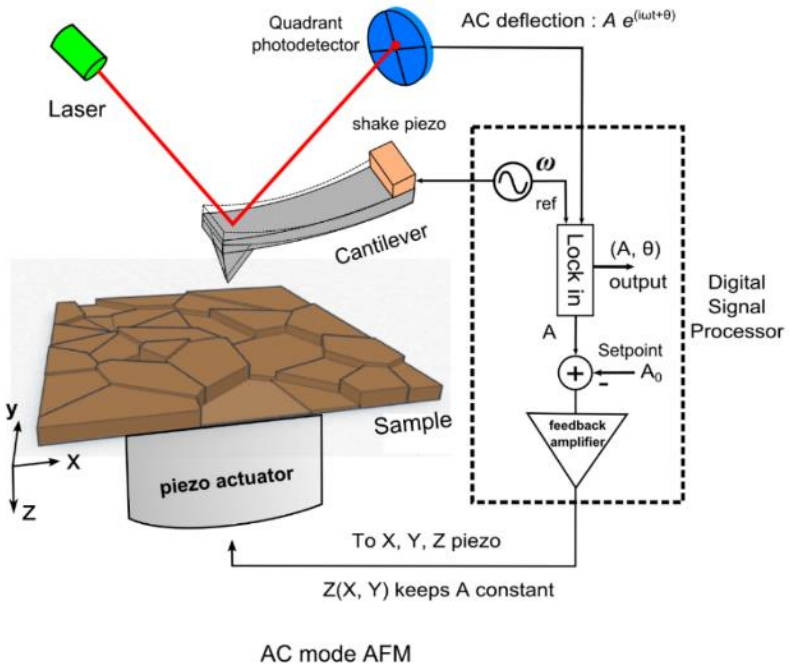

Figure 2-5 Schematic diagram of the essential components for AC mode AFM. (Adapted from Ref. 29)

2.4 C-AFM LITHOGRAPHY ON $LAALO_3/SRTIO_3$

As discussed in Section 1.3 and Section 1.4, the polar catastrophe induces metal-insulator transition at the interface between $LaAlO_3$ and $SrTiO_3$, and with a critical thickness (3 u.c.) $LaAlO_3$ on $SrTiO_3$, the interfacial conductivity can be macroscopically modulated by back-gating. Our group first demonstrated that positively biased AFM tip can locally induce a metal-insulator so that conducting nano-scale structures can be written using this c-AFM lithography. Writing with a positively biased (~5-10 V) AFM tip can leave positive charges on the $LaAlO_3$ surface[35], making the potential large enough to induce polar catastrophe, and consequently causing the insulating

interface to be conducting. In the meantime, a negatively biased AFM tip will remove the doped positive surface charges, and return the interface to the insulating state.

Figure 2-6 shows the nanowire writing on 3 u.c. $LaAlO_3/SrTiO_3$ heterostructures by the c-AFM lithography technique. For the writing process (Figure 2-6a), the AFM tip is biased with a positive voltage and scanned from one electrode to the other in contact mode. When the tip reaches the second electrode, the conductance between two electrodes has several orders of increase which indicates that a conducting channel (green line in Figure 2-6a) is formed at the $LaAlO_3/SrTiO_3$ interface. We can also cut the wire by applying a negative voltage to the AFM tip and erasing cross the conducting nanowire (Figure 2-6b). As the AFM tip cuts across the written nanowire, the conductance between two electrodes drops back to the insulating value, effectively creating a nano junction. By fitting the conductance drop, the nanowire width can be determined. By reducing the writing voltage, the width of the nanowire can be as small as 2 nm. In real device writing, the voltage used is the lowest voltage that can make the device survive, as determined by pretests.

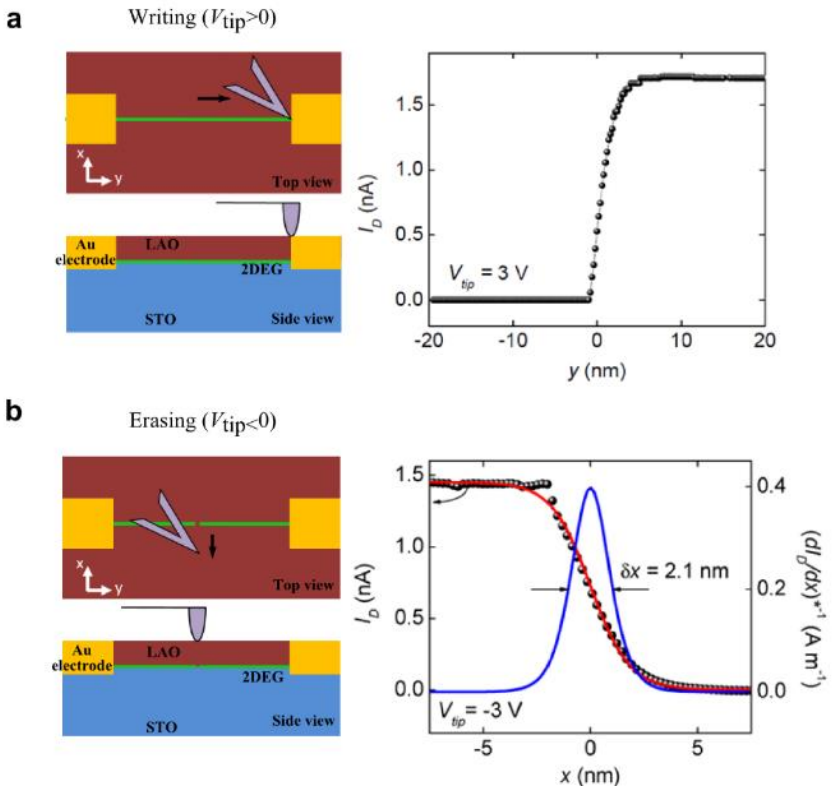

Figure 2-6 Conductive AFM lithography in 3 unit cell (u.c.) $LaAlO_3/SrTiO_3$ heterostructures. (a), c-AFM writing process with positive biased AFM probe. (b), c-AFM erasing process with negative biased AFM probe. The data is adapted from Ref. 36.

The writing procedure is attributed to a "water cycle" involves adsorbed H_2O dissociating into OH^- and H^+ on the $LaAlO_3$ surface. The first principles calculations[37] show that H_2O binds strongly to the AlO_2 outer surface and dissociates into OH^- and H^+ adsorbates. (Figure 2-7a) During the writing process, the positively-biased AFM probe removes OH^- atoms, leaving excessive H^+ ions locally charging the surface (Figure 2-7b). During the erasing process, the negatively biased AFM probe removes H^+ adsorbates, restoring the OH^--H^+ balance, and the interface reverts back to an insulating state (Figure 2-7c). We call this process as a "water cycle" because it permits multiple writing and erasing cycles without physical modification of the oxide heterostructures.

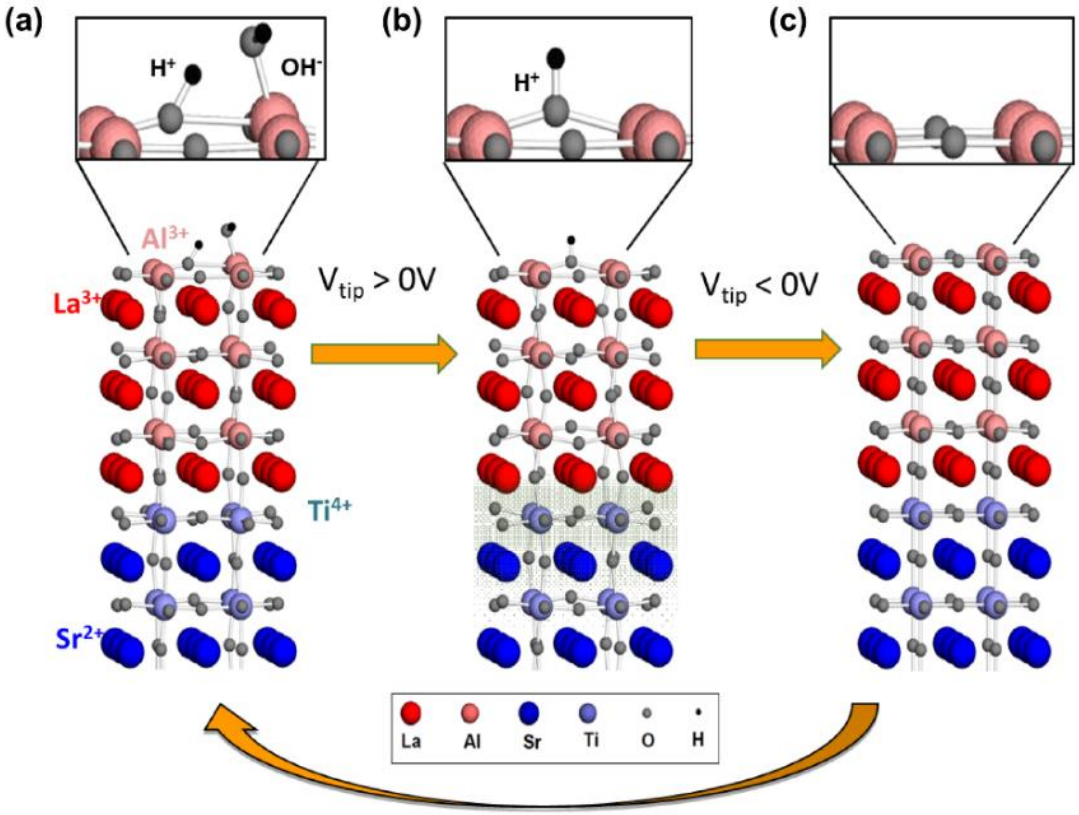

Figure 2-7 "water cycle" mechanism for c-AFM lithography on $LaAlO_3/SrTiO_3$. (a), Layer of water spontaneously adsorbed at the $LaAlO_3$ top surface. (b), Positive tip bias removes OH^-, leaving H^+ adsorbate and producing a metallic interface. (c), Negative tip bias removes residual H^+ and restores the initial insulating state (Adapted from C. S. Hellberg, APS talk)**.**

3.0 ANOMALOUS TRANSPORT IN SKETCHED NANOSTRUCTURES

Nanoscale control of the metal-insulator transition in $LaAlO_3$/ $SrTiO_3$ heterostructures can be achieved by using local voltages applied by a conductive atomic-force microscope probe. With this technique, nanowires with a line width of ~ 10 nm can be created on the $LaAlO_3/SrTiO_3$ interfaces. Four terminal transport measurements of those nanowires at room temperature show large enhancement of mobility, relevant for room temperature device applications. At low temperature, nanostructures show superconductivity with finite resistance, and nonlocal transport phenomena can be observed both at normal state, and superconducting state, suggesting an indicate edge state in the device.

This thesis has major contributions to the results described in this chapter. For enhanced high mobility in 1D nano wires in sections 1.0 3.4, I designed, tested, and analyzed most of samples. For nonlocal transport in section 3.5, I was one of the four individuals who recorded all the experimental data. I also enhanced the project by finding the tunability of the non-local signals.

3.1 INTRODUCTION

The discovery of a two-dimensional electron liquid (2DEL) at the $LaAlO_3/SrTiO_3$ interface has attracted lots of attention because of the wide range of properties discovered. These phenomena emerge from the conducting 2DEL at the interface, the metal-insulator transition (MIT) near the critical $LaAlO_3$ thickness, superconductivity, coexistence of superconductivity, magnetism under some conditions, and strong Rashba spin orbit coupling with spin splitting as large as 10 meV. The

MIT of four unit cell (4 u.c.) $LaAlO_3/SrTiO_3$ heterostructures can be controlled by a voltage-biased conductive atomic force microscope (c-AFM) tip in contact mode with the top layer of $LaAlO_3$, and the resolution can be as high as 2 nm. This technique enables the creation of a variety of nanostructures such as nanoscale transistors, rectifying junctions, optical photodetectors, and single electron transistors. The experiments described here are mainly performed on $LaAlO_3/SrTiO_3$ Hall bar nanostructures. Many new anomalous phenomena occur when constraining the device to the nanoscale, including great mobility enhancement in nanowires compared to 2D structure, non-local transport at normal state which might be related to edge states, and non-local transport at the superconducting state.

3.2 SAMPLE GOWTH

Details about sample growth are discussed in Section 1.2. Thin films (3 u.c.) of $LaAlO_3$ were deposited on a TiO_2-terminated (001) $SrTiO_3$ substrates by our collaborators by using pulsed laser deposition with *in situ* high pressure reflection high energy electron diffraction (RHEED)[38]. Growth was at a temperature of 550°C and O_2 pressure of 1×10^{-3} Torr. After growth, electrical contacts to the interface were prepared by milling 25 nm deep trenches via an Ar-ion mill and filling them with an Au/Ti bilayer (2 nm adhesion Ti layer, and 23 nm Au layer). Figure 3-1a shows an example of the fabricated electrodes on a 3 u.c. $LaAlO_3/SrTiO_3$ heterostructure. The electrical contacts define a 30 μm × 30 μm canvas for AFM writing experiments, as illustrated in Figure 3-1b.

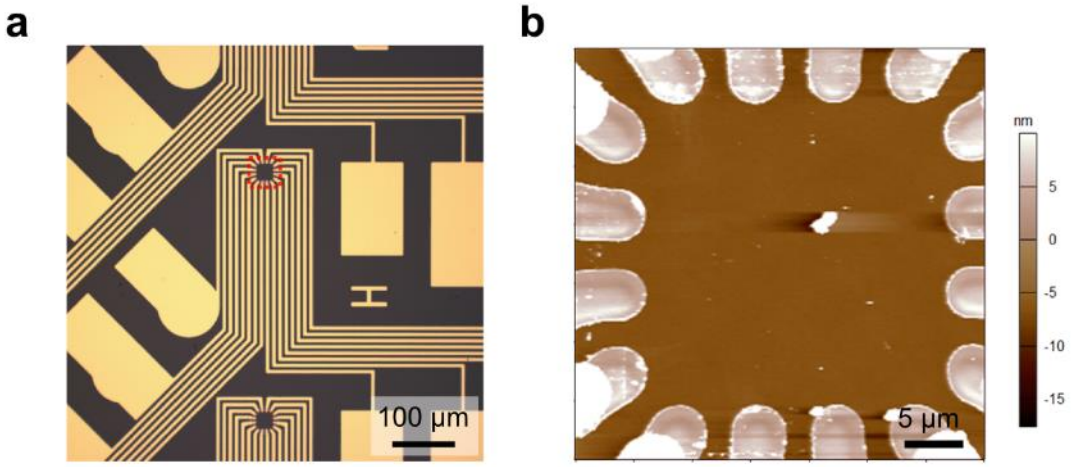

Figure 3-1 Fabricated electrodes and writing canvas. (Adapted from Ref. 29) (a), Fabricated Au electrodes that make contact to the $LaAlO_3/SrTiO_3$ interface. The red dash line encloses the region that serves as the AFM writing canvas. (b), AFM height image of the writing canvas showing sixteen electrodes contacting the interface.

3.3 EXPERIMENT SETUP

The general device writing method is described in section 2.4, and the detailed structure is described in each section below. In order to perform transport experiments at cryogenic temperatures, the sample is transferred, after the writing, in the dark into a Quantum Design-physical property measurement system (QD-PPMS) with dilution unit capable of reaching 50 mK base temperature and nine T magnetic field. Simultaneous sampling 24-bit data acquisition cards are used to source voltages and acquire amplified voltage signals coming from true differential voltage amplifiers (Femto model DLPVA). A one TΩ input impedance eliminates the current draw from the voltage sensing contacts. I-V measurements were performed at low-frequencies (1.34-

13.4 Hz) in order to minimize capacitive and inductive coupling. A back-gate, V_{bg}, is applied through the $SrTiO_3$ substrate (0.5 mm thick). The leakage to the device from the back-gate is kept below one pA by connecting a 100 Mohm resistor in series with V_{bg}.

3.4 ENHANCED HIGH MOBILITY IN 1D NANO WIRES

As previously mentioned, different phenomena have been observed at the interface of $LaAlO_3/SrTiO_3$ including tunable metal-insulation transitions, magnetism, superconductivity, and strong spin-orbit coupling. Despite these promising functions, the system still has relatively low room-temperature mobility (6 $cm^2/(V \cdot s)$), which has tempered enthusiasm for applications. The low-temperature mobility of the $LaAlO_3/SrTiO_3$ system has been enhanced by optimization of growth conditions and doping; however, no experimental results show enhancement of room-temperature mobility. Here we demonstrate lateral confinement of nanostructures at the $LaAlO_3/SrTiO_3$ interface, leading to great enhancement of room-temperature and low temperature mobility which make this system even more promising.

Nanowires are formed using c-AFM lithography (Figure 3-2a). Here, for comparison we present data from two types of devices: nanowire Hall bar structures and two-dimensional squares with different sizes. The results described come from a total of 16 distinct devices (nine Hall crosses and seven squares) which were written on five distinct thin films (see Table 3-1 for a device summary). 2D mobility for a 14 u.c. $LaAlO_3/SrTiO_3$ whose interface is conducting intrinsically is also measured in van der Pauw geometry for additional comparison.

In order to measure 2D properties of the 3 unit cell interface samples, square-shaped conducting areas with length scale of 20 – 1000 nm are written and measured by the van der Pauw

method (Figure 3-2e). Nanowire properties are determined by writing multi-terminal Hall bars. A schematic of a six-terminal configuration is showed in Figure 3-2b. The Hall bars have channel widths, w, ranging from 10 to 100 nm and lengths, L, ranging from 1.2 to 8 μm. The narrowest structures ($w \sim 10$ nm) are written with a single c-AFM tip movement, shown in Figure 3-2a. Wider structures are written by controlling the c-AFM tip back and forth movement with constant separation to form a rectangular-shaped structure with the desired width.

Four-terminal and two-terminal current–voltage (I-V) curves are acquired by sourcing a voltage, V_{ab}, between electrodes "a" and "b", and measuring both the current, I_{ab}, and the differential voltage, V_{cd}, between electrodes "c" and "d". The resistance, $R_{ab,cd} = dV_{cd}/dI_{ab}$, yields either the channel (R_{xx}) or transverse Hall (R_H) resistance as shown in Figure 3-2b. At room temperature, R_{xx} typically ranges between 10 kΩ and 1 MΩ depending on structure width and other factors. The Hall resistance $R_H = R_{AB,CF}$ is simultaneously measured by monitoring the voltage between electrodes "B" and "F". In order to acquire the 2D carrier density, $n_s = \frac{1}{e}\frac{\Delta B}{\Delta R_H}$, where e is the electron charge, magneto-resistance R_{xx} and R_H are measured by applying an out-of-plane magnetic field B. The quantity $\frac{\Delta B}{\Delta R_H}$ is calculated by performing a linear fit to $R_H(B)$. The 2D Hall mobility is calculated using the expression $\mu_H = \frac{1}{en_s R_{xx}(0)}\frac{L}{w}$.

Typical R_{xx} and R_H versus B curves are showed as in Figure 3-2c-d. Slight changes in the R_H between forward and backward sweeps are observed; device drift as a function of time is typical in $LaAlO_3/SrTiO_3$ based nanostructures, and these slight differences are accounted for by symmetrizing the forward and backward-swept data collection sets. The Hall offset resistance $R_H(0)$ observed in device H8 (Figure 3-2d) can be converted to an equivalent longitudinal shift

between the terminals on opposite sides of the channel $\delta x = (R_H(0)/R_{xx})L \approx 0.5$ nm, much smaller than the nanowire width. R_{xx} and R_H versus B for device vdP3 (w = 500 nm) are shown in Figure 3-2f, g.

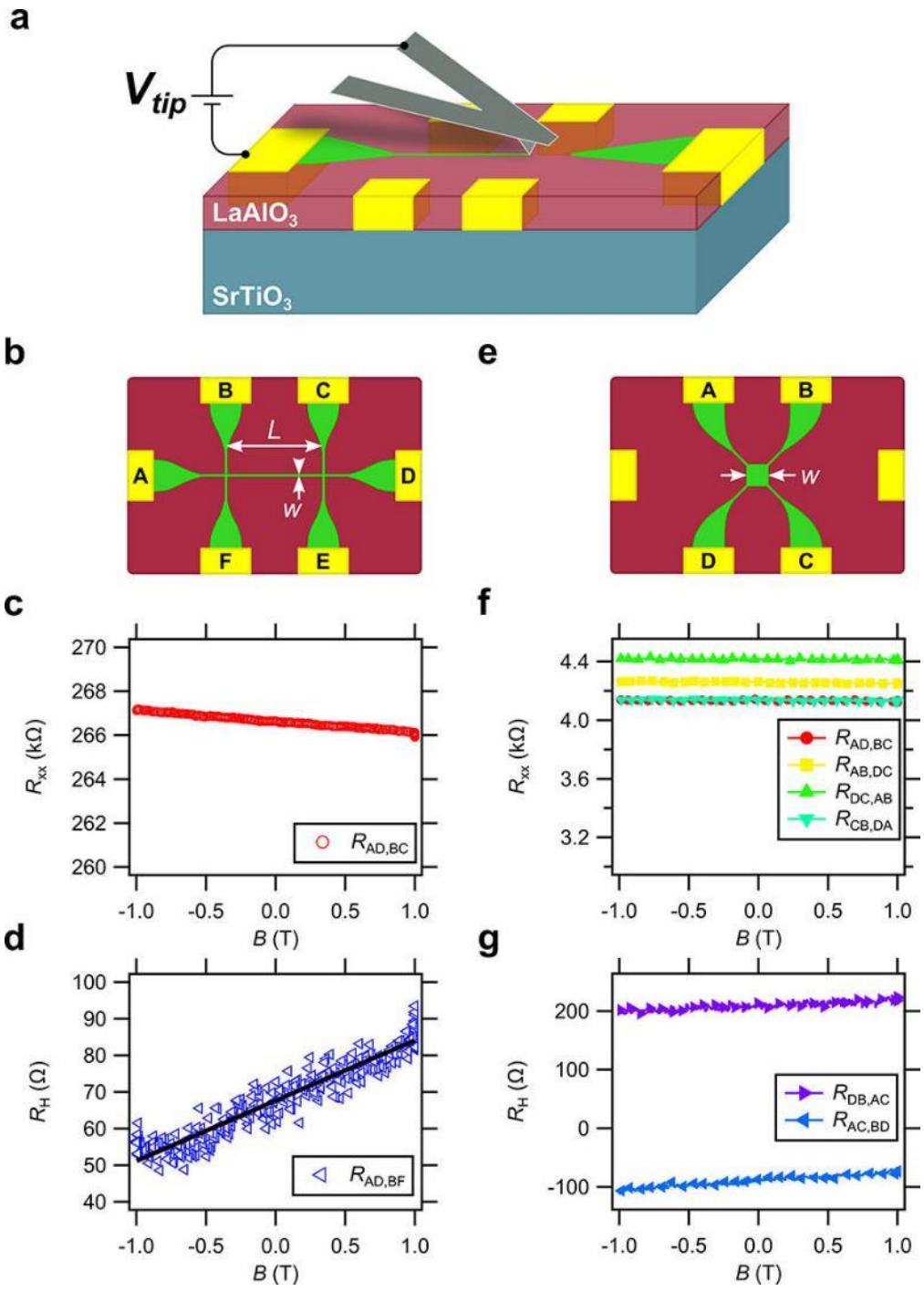

Figure 3-2 Device schematic and transport measurement. (a), c-AFM lithography is used to write a nanoscale device at the interface between $LaAlO_3$ and $SrTiO_3$. (b), Schematic arrangement of a six terminal Hall cross device. (c,d), Longitudinal and Hall resistances of a six terminal Hall cross, device H8 (w = 20 nm). (e), Electrode arrangement for van der Pauw transport measurements. (f,g), Longitudinal and Hall resistance in van der Pauw geometry of device vdP3 (w = 500 nm).

Table 3-1 High mobility device growth parameters and transport characteristics. Growth type, channel length (L), and width (w) are identified for each sample. Equivalent 2D Hall mobility (μ_H) and sheet carrier density (n_s) are shown at room temperature (300 K). LTHP: 550°C, $P_{O2} \sim 10^{-3}$ mBar. HTLP: 780°C, $P_{O2} \sim 7.5 \times 10^{-5}$ mBar.

Device name	Growth type	μ_H ($cm^2/(V \cdot S)$)	n_s (10^{12} cm^{-2})	Channel length (nm)	Channel width (nm)
2D	LTHP, 14 uc	6	9.5	5×10^6	5×10^6
vdP2	LTHP, 3 uc	6	5.6	1000	1000
vdP3	LTHP, 3 uc	6	5.1	500	500
vdP4	LTHP, 3 uc	6	4.2	250	250
vdP5	LTHP, 3 uc	7	7.4	125	125
vdP6	HTLP, 3 uc	7	6.6	80	80
vdP7	HTLP, 3 uc	7	7.4	50	50
vdP8	HTLP, 3 uc	7	9.2	20	20
H7	LTHP, 3 uc	25	1.2	2000	100
H1	LTHP, 3 uc	60	7	2000	60
H9	LTHP, 3 uc	77	6.2	2000	30
H8	LTHP, 3 uc	65	3.6	2000	20
H5	LTHP, 3 uc	86	3.7	6600	10
H6	LTHP, 3 uc	100	11	1200	10
H2	HTLP, 3 uc	130	3.3	8000	10
H3	HTLP, 3 uc	160	3.8	7000	10
H4	HTLP, 3 uc	350	8.7	6300	10

Figure 3-3a-b summarizes the mobility and carrier density for both Hall bars with widths ranging from 10 nm to 1 μm, and van der Pauw geometries. The van der Pauw devices (vdP2 – vdP8) show a room temperature mobility of approximately 6−7 $cm^2/(V \cdot s)$ regardless of width which are generally in good agreement with the 14 u.c. 2D control sample. However, among the

Hall bar devices, even the widest structure, Device H7 with a main channel width w_{H7} = 125 nm, displays a modest increase in mobility to μ_{H7} = 25 $cm^2/(V \cdot s)$. This trend continues as mobility further increases as w is reduced. Nanowires with w = 10 nm exhibit the largest mobility enhancements, which can reach as high as 350 $cm^2/(V \cdot s)$; this device has mobility that is 60 times that of bulk $SrTiO_3$ at room temperature. Mobility enhancements are observed in samples grown with both HTLP and LTHP growth conditions, with $\bar{\mu}_{HTHP}$ = 210 $cm^2/(V \cdot s)$, and $\bar{\mu}_{LTHP}$ = 90 $cm^2/(V \cdot s)$, implying that the effect is not principally related to growth conditions.

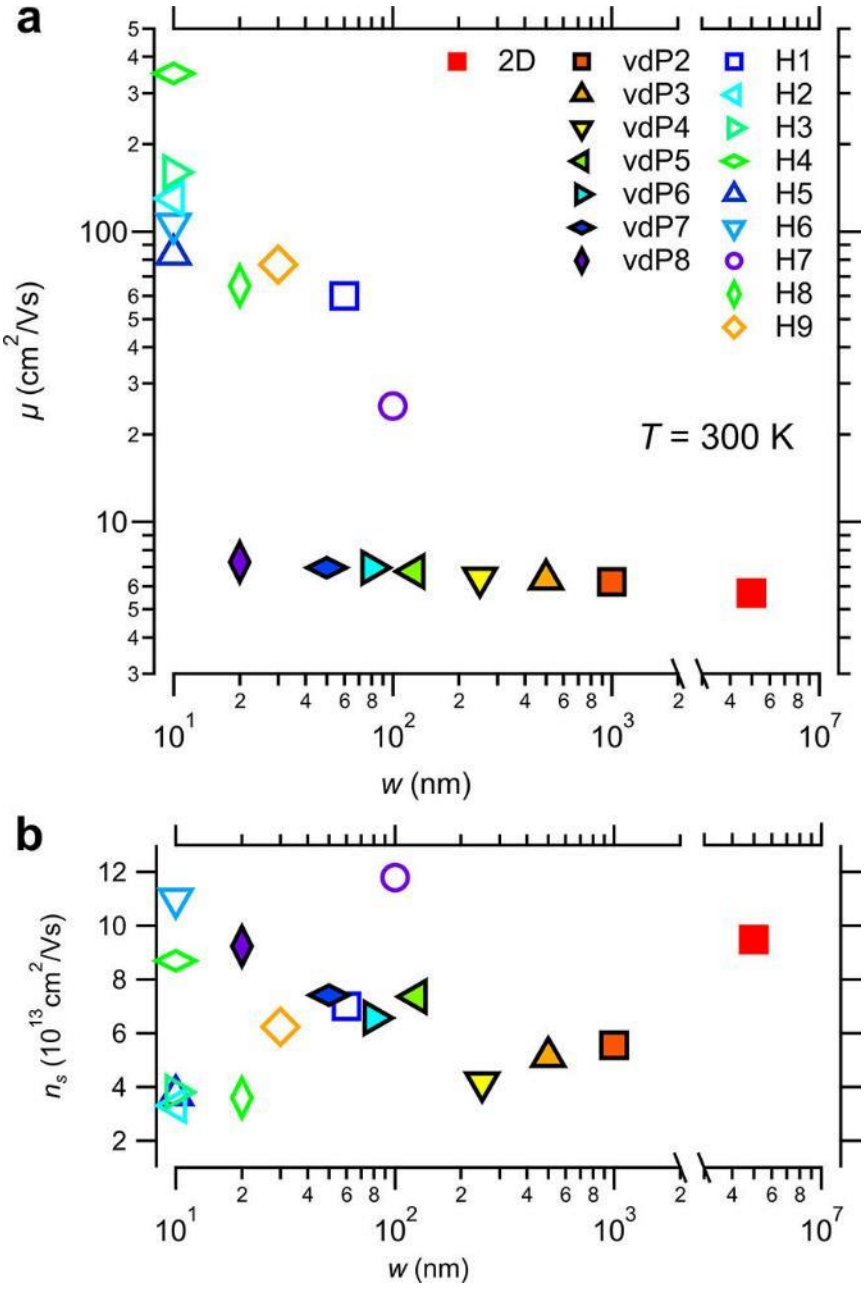

Figure 3-3 Summary of mobility and carrier density for different devices. (a), Equivalent 2D Hall mobility and (b), carrier density, are plotted as a function of wire width at room temperature. Open symbols represent measurements in the Hall geometry; closed symbols are taken in van der Pauw geometry.

Figure 3-4 shows temperature-dependent transport properties of representative devices, indicating that mobility enhancements compared to the 2D structures persist in low temperature.

While the mobility of the 2D device is scaled as T^2 over the temperature range 50−300 K, similar to bulk n-type $SrTiO_3$[39], the mobility of devices H5 and H6 clearly deviate from this power-law scaling and change much more rapidly over the same temperature range. Device H6 reaches more than 20,000 $cm^2/(V \cdot s)$ at the maximum mobility at 20 K, then decrease a little bit at lower temperatures. This non-monotonic behavior is correlated with resistance changes and a breakdown of scaling between the two-terminal ($R_{2t} = R_{AD,AD}$) and four-terminal resistances (Figure 3-4a, inset). R_{xx} and n_s for devices H5 and H6 are plotted as a function of temperature in Figure 3-4b and Figure 3-4c, respectively.

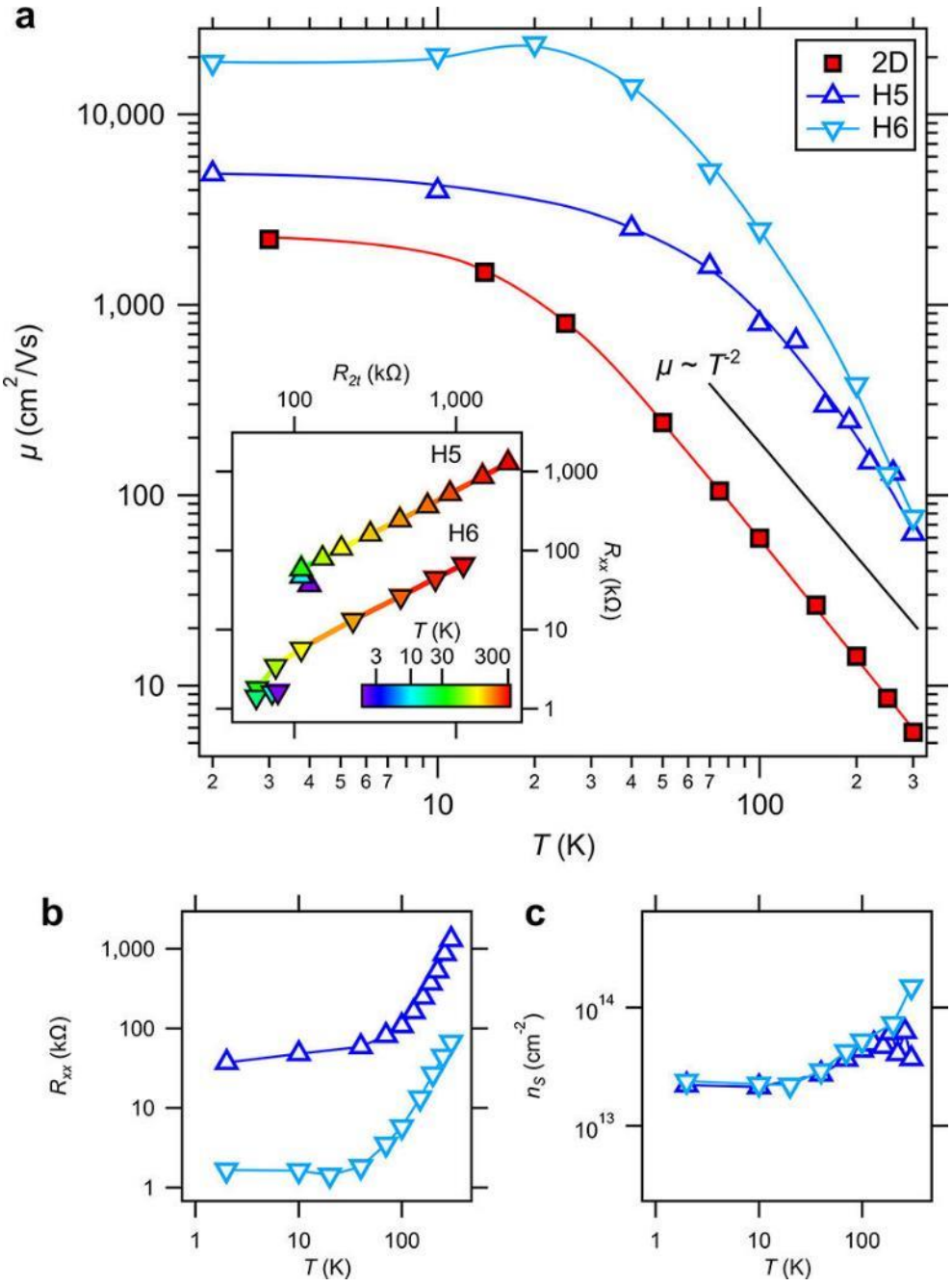

Figure 3-4 Equivalent 2D Hall mobility is measured as a function of temperature. Symbols are data points, lines are guides to the eye. (a), 1/ T^2 line is shown for comparison. Inset shows the four-terminal resistance R_{xx} plotted versus the two-terminal resistance R_{2t}, parametrized by temperature for devices H5 and H6. Also shown is the four-terminal resistance R_{xx} (b), and sheet carrier density $n_{S,}$ (c), as a function of temperature for devices H5 and H6.

The observed enhancement of carrier mobility in nanowire devices is quite different from what is typically observed in semiconductors. The room-temperature mobility of bulk silicon (1400 $cm^2/(V \cdot s)$) is reduced when constrained into a nanowire geometry (e.g., 200−300 $cm^2/(V \cdot s)$[40]); surface passivation can help restore, but does not enhance, the mobility[41]. Greater carrier mobility enhancement with decreasing nanowire width have not been reported for silicon or III−V semiconductor nanowires.

There are several factors that may help to explain this observed mobility enhancement. First, one may consider the c-AFM lithography technique. As discussed in Section 2, conductivity at the $LaAlO_3$/ $SrTiO_3$ interface is controlled by placement of positive charges on the top $LaAlO_3$ surface. This type of surface modulation doping can reduce scattering from charged impurities, as with III−V semiconductor heterostructures. However, square devices which are also created by the c-AFM technique do not exhibit an enhancement of mobility at room temperature, ruling out this as the principal mechanism. Another factor that must be considered relates to the consequences of an inhomogeneous carrier density, which can sometimes lead to an apparent mobility enhancement[42]. However, measured carrier densities for the w = 10 nm devices are generally comparable to the measurements of 2D devices. In addition, nanoscale inhomogeneities on the scale of these devices are predicted to result in an overall lower mobility.

The fact that some of the narrowest nanowires (w = 10 nm) show different carriers suggests that there is a hidden variable more closely related to the enhancement of the mobility. The mobility enhancement of devices created on HTLP-grown samples is somewhat higher as compared to LTHP-grown samples. However, variations among the HTLP devices are themselves large, implying that the overall room-temperature mobility enhancements are not growth-related. In the temperature range 100−300 K, the T^2 dependence appears to be consistent with

Landau−Pomeranchuk scattering[43]. A phonon-mediated electron−electron interaction is also observed in bulk *n*-type $SrTiO_3$[39]. A predicted breakdown of T^2 scaling in one dimension[44] could be a possible explanation of the results presented here.

As described previously, the room-temperature 1D and 2D device mobilities begin to diverge around 100 nm. We also note that, when comparing 1D and 2D devices, the temperature dependence of mobility also shows different behavior: 2D devices follow a T^2 dependence, while in 1D devices, the mobility changes more rapidly. Typical variations in the nanowire width for a given sample, a ∼20% set of writing conditions, and the method used to determine the width of the nanowires, could be underestimated by a factor of two, however the 1D mobility is 25 times that of the mobility of 2D structures, so it is apparent that the 1D and 2D devices display very different physics. The observation of a room-temperature mobility enhancement only in 1D devices with high L/w aspect ratios suggests that there is a potential long-range coherence that only becomes apparent when devices are scaled to quasi-one dimension. The enhanced room-temperature mobility at the $LaAlO_3/SrTiO_3$ interface holds great promise for introducing this oxide material system to practical applications at room temperature, as well as suggesting novel physics. Further experiments and theoretical treatments are necessary to more precisely reveal the physical mechanism(s) to further optimize the mobility enhancement for device applications.

3.5 NONLOCAL TRANSPORT

3.5.1 Nonlocal transport at normal state

Table 3-2 summarizes device names, and sample growth parameters. Nanoscale devices are written using the c-AFM technique as described in Chapter 2. Five-terminal Hall bar device with the main channel length varying from 2 μm to 10 μm are written with 10-15 V tip voltage at a speed of 200 nm/s. The resulting nanoscale devices are composed of nanowire segments that have widths around 10 nm, as determined by erasing the nano wire on the same canvas of the sample with the same AFM tip. Trapezoidal virtual electrodes connect the gold interface electrodes at one end, and the nano scale devices at the other end, as shown in Figure 3-5a-b. Upon completion of device writing, the sample is transferred to the vacuum environment of a dilution refrigerator for low temperature measurement within five minutes.

Table 3-2 Nonlocal device growth parameters and transport characteristics.

Device name	Growth temperature (ºC)	Oxygen pressure (mBar)	Anneling conditions	Channel length (μm)	Channel width (nm)	Nonlocal resistance (Ω)
C	780	7.5×10^{-5}	600 ºC	10	10	2500
C2	550	1×10^{-3}	No	6.5	10	1500
C3	550	1×10^{-3}	No	12	10	20
H	550	1×10^{-3}	No	2	10	0
H2	780	7.5×10^{-5}	600 ºC	10	10	0

Table 3-2 (continued).

H3	550	1×10^{-3}	No	6.5	10	0
H4	550	1×10^{-3}	No	6.5	10	0
H5	550	1×10^{-3}	No	10	10	0
H6	550	1×10^{-3}	No	2	250	0
H7	550	1×10^{-3}	No	2	50	0

Transport experiments are carried out at two locations, the University of Pittsburgh (Pitt, devices C and H-H7), and the National High Magnetic Field Laboratory (NHMFL, devices C2 and C3), using independent measurement set-ups. At both locations, true differential voltage amplifiers (Femto model DLPVA) with a 1-TΩ input impedance are used so that virtually no current flow from the voltage-sensing leads. At Pitt, simultaneous-sampling 24-bit data acquisition cards are used to source voltages, and acquire amplified voltage signals. Lock-in amplification is achieved by demodulating the signal with computer-based digital signal processing, allowing simultaneous measurement of up to four channels. For electrical current measurements, a low input impedance current amplifier is used (Femto DDPCA-300). At NHMFL, conventional lock-in amplifiers are employed to perform transport measurements. Low-frequency (~1.3 Hz) lock-in detection is used at both locations to minimize capacitive and inductive coupling. Devices are cooled in refrigerators with base temperatures of 50 mK (Pitt), 20 mK (NHMFL), or 250 mK (NHMFL).

Transport measurement are carried out on five-terminal or six-terminal Hall bar structures with nanowire segments that are about 10 nm wide. All results discussed here have been reproduced qualitatively in multiple devices from different $LaAlO_3/SrTiO_3$ samples with different growth conditions and measurement setups. Although the samples are fabricated in a similar

fashion, and the devices are written in similar conditions and parameters, two distinct classes of physical properties emerge among all devices. Among the ten devices discussed here, three exhibit "Type-C" behavior, while other seven exhibit "Type-H" behavior. The devices themselves are labeled according to the classification of the properties (e.g. device C3 or device H4). Representative device C and device H for each type are shown in Figure 3-5 with device schematics and transport properties. A detailed summary of device properties is shown in Table 3-2.

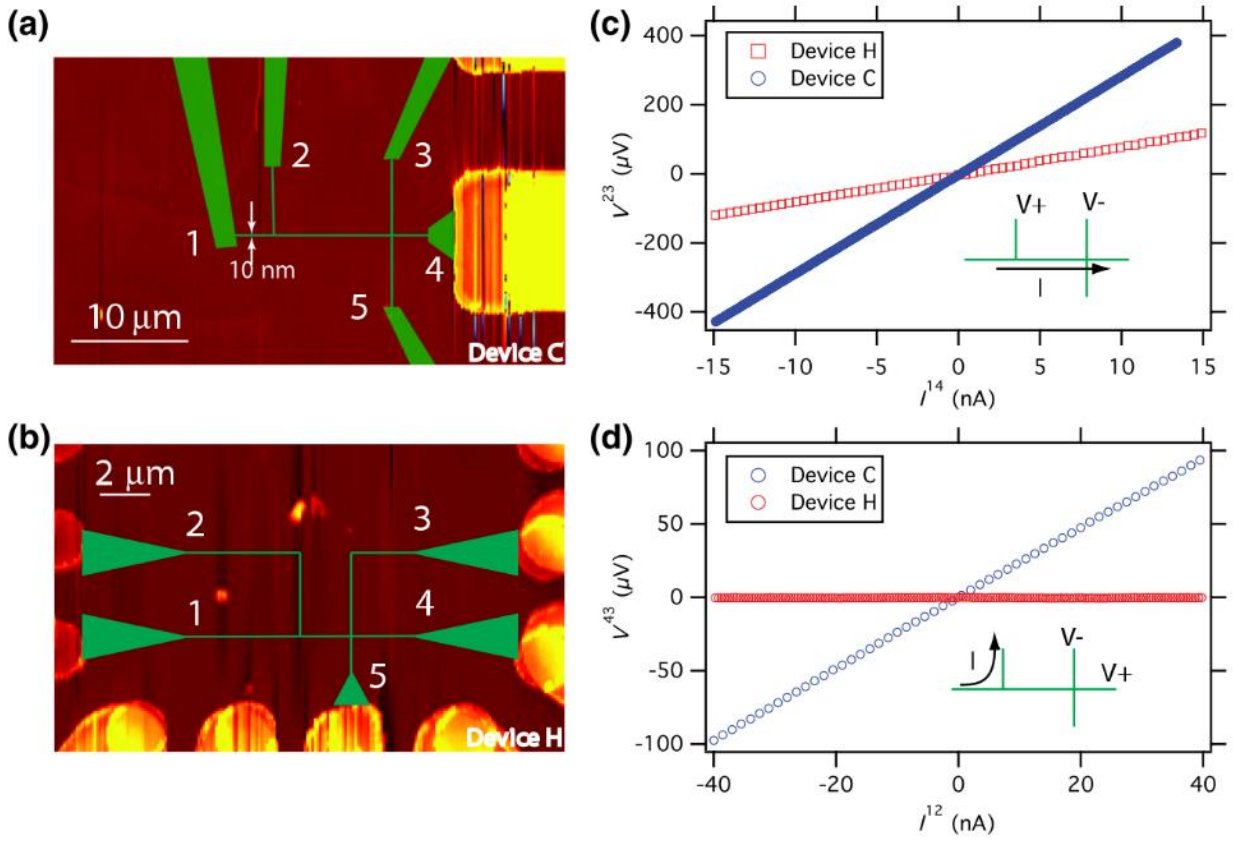

Figure 3-5 Device schematic and electrical characterization of $LaAlO_3/SrTiO_3$ nanostructures. (a), Five-terminal structure (device C, overlaid on an AFM canvas image) composed of W = 10-nm-wide conducting nanowires (green), including an L = 10-µm-long main channel surrounded by insulating (red) background. (b), Five-terminal nanowire (device H) formed in a similar fashion (W = 10 nm, L = 2 µm). (c), Longitudinal I-V curves for devices C and H at T

= 400 mK. The inset shows the direction of the current flow and voltages measured. (d), Nonlocal I-V curves for devices C and H at T = 400 mK. The inset shows the direction of the current flow and voltages measured.

Four-terminal IV curves are acquired by sourcing current I_{ab} from lead "a" to lead "b" and simultaneously measuring the voltage, V_{cd}, between lead "c" and lead "d". The differential resistance $R_{ab,cd} = dV_{cd}/dI_{ab}$ is obtained by numerical differentiation. Figure 3-5c shows linear IV curves for both device C and device H, from which we find $R^{C}_{14,23} = 28.4\ k\Omega \approx 1.1\ h/e^2$ and $R^{H}_{14,23} = 6.9\ k\Omega \approx 1.3\ h/e^2$, respectively. The channel resistance for both devices is approximately temperature independent up to and around 50 K before they shoot up to several hundred kilo-ohms at room temperature.

Figure 3-5d shows the nonlocal transport properties of device C i.e. sourcing current I_{12} and measuring the voltage between the lead "4" and lead "3", the V_{43}, which is 10 μm away from the current channel. The IV curve is linear with nonlocal resistance $R^{C}_{12,43}$ = 2.5 kΩ and the thermoelectric effects can be ruled out based on the linear IV curve within low sourcing current ~ 15 nA. The nonlocal resistance for device H is vanishing within measurement limits.

Figure 3-6a shows the magnetic field dependence of the nonlocal resistance $R^{C}_{14,23}$ for device C. The nonlocal magneto-resistance can be empirically described as $R^{C}_{14,23} \propto \sqrt{B^2_{NL} + B^2}$, where B_{NL} = 15 T in this case. The forward and reverse sweep exhibit some hysteresis due to device drift, which is quite normal for $LaAlO_3/SrTiO_3$ based nano structures, as previously described. Additionally, a resistance shoulder near +/- 3 T is observed after sweeping through the zero field, similar to the effect reported by Brinkman *et al.*[23]. The local two terminal magneto-resistances (Figure 3-6b) show similar overall positive curvatures and hysteresis.

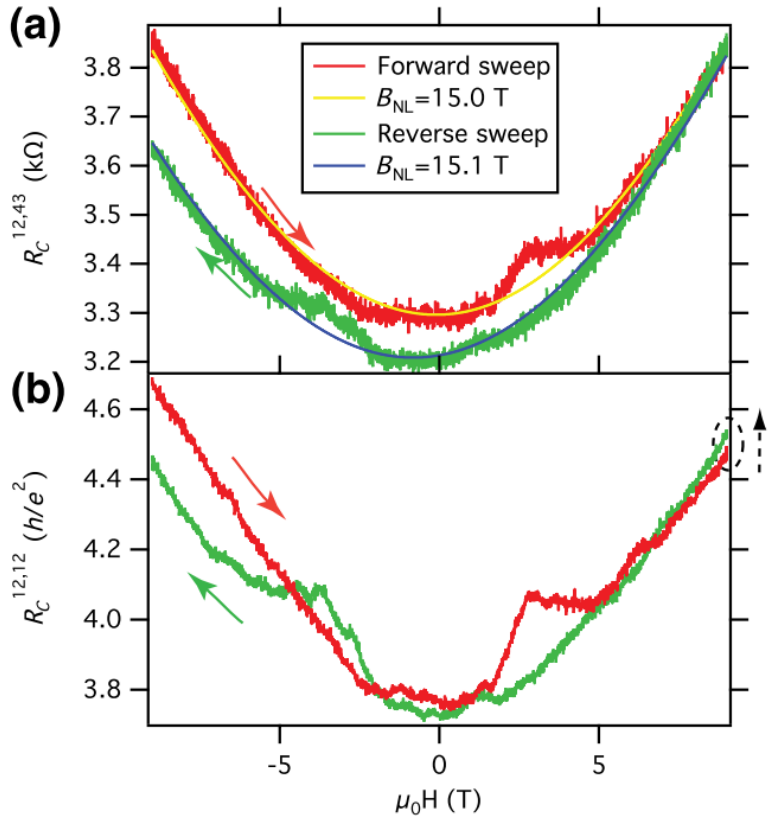

Figure 3-6 Out of plane field dependence. (a), nonlocal resistance $R^C_{12,43}$, and (b), local two-terminal resistance $R^C_{12,12}$ at T = 4 K. Red and green curves represent forward and reverse sweeps (at 3 mT/s). Yellow and blue solid lines in (a) are empirical fits with form $R^C_{14,23} \propto \sqrt{B^2_{NL} + B^2}$, giving two similar built-in fields B_{NL} of 15.0 T and 15.1 T.

Below the superconductivity critical temperature $T_c \approx 200$ mK, superconductivity plays a very important role by interacting with nonlocal resistance. Figure 3-7a shows the four terminal IV curve for device C at T = 65 mK, well below T_c. The region of low resistance state for $|I_{14}| < I^c_{14}$ = 3 nA results from superconductivity in the nanowires as described in detail elsewhere[45]. Application of a magnetic field larger than $H_c \approx 1500$ Oe destroys the superconductivity, thereby restoring the linear IV curves. Figure 3-7b shows that the nonlocal IV curves also respond to a magnetic field and that the nonlocal resistance collapses within the sourcing current range of

$|I_{12}| < 25$ nA. When the sourcing current is exceeded, or the applied magnetic field becomes sufficiently large, superconductivity is suppressed and the nonlocal resistance is restored. The nonlocal critical current is approximately one order of magnitude larger than the critical current of the main channel, and the nonlocal critical current is not directly related to the superconductivity critical current in the main channel since there is no current flow within the main channel.

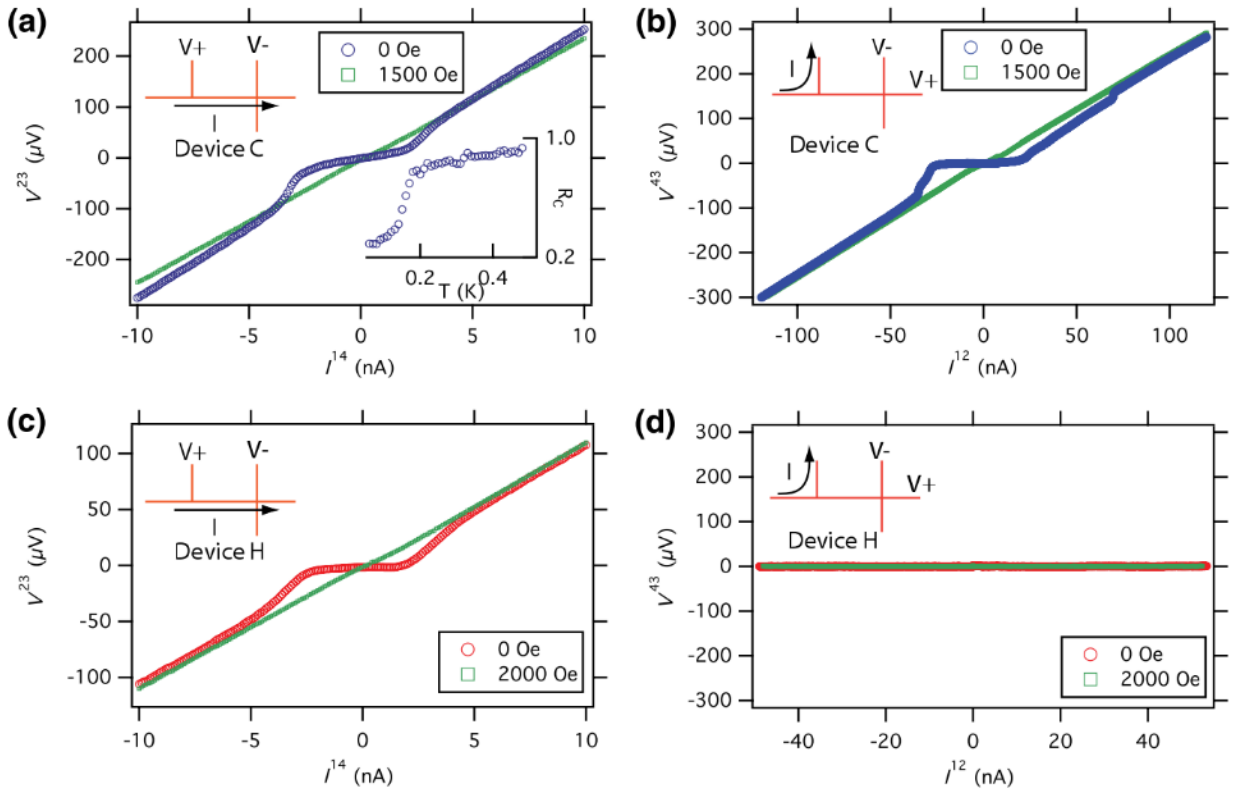

Figure 3-7 Interaction between Cooper pairs and nonlocal transport. (a), IV curves for device C at T = 65 mK, which is below the superconducting critical temperature. The lower-resistance region of the H = 0 curve is related to the formation of Cooper pairs. Normal-state is restored by applying an external magnetic field (green curve). The inset shows the temperature dependence of channel resistance, indicating that the critical temperature is around 200 mK. The y-axis unit is h/e^2. (b), Nonlocal resistance $R_{12,43}$ of device C of H = 0 T. The Cooper pairs block spin transport without current flow, which is required for manifestation of nonlocal resistance. Applying an external magnetic field restores the linear nonlocal response (green curve). (c), Channel IV curves for device H at T = 50 mK in the

superconducting regime (H = 0 oe), and normal state (H = 2000 Oe). (d), Nonlocal resistance $R_{12,43}$ of device H is vanishing both above and below T_c.

The local and nonlocal transport results described here put a strong constraint on any theoretical description. First, the three unit cell $LaAlO_3/SrTiO_3$ interface is naturally insulating: sheet resistances are of order GΩ at room temperature and will become immeasurably large at low temperature. Secondly, thermoelectric effects cannot account for the quite large nonlocal resistance, since the IV curves would have a nonlinear response instead of a linear response (Figure 3-5d). Finally, the most important fact is that there is no current flow through the main channel, which can imply the existence of another variable that relates the voltages and currents, e.g. the spin degree of freedom. The observation of a nonlocal transport spanning the device dimensions, two orders of magnitude larger than the spin coherent length of 2D $LaAlO_3/SrTiO_3$ (10 μm compare to 10-100 nm), is also striking.

There are several nonlocal transport effects reported in semiconductors and superconductors among which we can search for the explanation of the results observed. Superconductivity-related nonlocal effects such as charge imbalance or the Andreev reflection[46] cannot explain the existence of nonlocal signals above the superconducting critical temperature. Large nonlocal transport is also observed in topological insulator phases, e.g. HgTe/CdTe quantum wells[47-49]. However this requires a bulk energy gap, and the electron bands in $LaAlO_3/SrTiO_3$ are all electron-like. The nonlocal resistances observed in our experiments are relatively much larger than the nonlocal resistance observed in spin Hall effect experiments[50]. Furthermore, in order to observe spin Hall effect, the sourced electrons need to be spin polarized[50,51] or have a high sensitivity detector[52]. Nonlocal transport effects are also observed in graphene near the Dirac point[53]; however, a strong magnetic field is necessary.

While the origin of the nonlocal transport is still an open question, these experimental results suggest some form of a highly coherent charge and/or spin transport. A few of these possibilities will be discussed. If the nanowire is regarded as a 2D system, a bulk gap will introduce topological insulator states leading to nonlocal transport. Experiments in 2D $LaAlO_3/SrTiO_3$ devices observe magneto-conductance oscillations as a function of an in-plane magnetic field, which demonstrates the opening and closing of a spin-orbit gap. A bulk gap can be opened by either a lateral quantum confinement or a disorder, which could also be the case here. Another possible explanation for the nonlocal transport could be the presence of a novel helical band structure in the 1D $LaAlO_3/SrTiO_3$ nanowires as proposed by Fidkowski *et al.*[54]. In those helical wires, spin and momentum are locked, which is attributed to spontaneous ferromagnetism and strong spin-orbit coupling that have also been discovered in the $LaAlO_3/SrTiO_3$ system. Such a helical wire could support nonlocal transport due to the coupling between spin-momentum locked transmission modes, and magnetism in different leads.

3.5.2 Tunability of nonlocal transport

Here we mainly focus on the devices that show nonlocal transport signals; even among these devices there are two kinds of nonlocal signals. The first kind of nonlocal voltage signal is the linear dependence of the source current as shown in Figure 3-8. Four-terminal IV curves are acquired by sourcing current I_{12} from lead "1" to "2", and simultaneously measuring the voltage, V_{34}, between leads "3" and "4" which is separated from the main current channel by 2.5 μm. Figure 3-8a shows that the main channel IV curves change as the back-gate changes, and the resistance, extracted from fitting IV curves, varies from 10 Kohm to 42 Kohm as the back-gate changes from 5.0 V to 1.6 V (Figure 3-8c). And Figure 3-8b and 3-8d show linear nonlocal current-voltage (I-

V) and the four-terminal resistance vary from 0 Ω to 235 Ω when the back-gate is decreased from 5.0 V to 1.6 V at T = 50 mK. Two-terminal IV measurements for leads "3" and "4" indicate that they become insulating when the back-gate is below 1.6 V, rendering it unable to measure the four-terminal IV curves with the 1.6 V back-gate. Each IV curve in Figure 3-8b has its offset at zero current subtracted, which is believed to be introduced by the instrument's offset. The nonlocal resistance remains around 0 Ω above the 3.5 V back-gate and increases to 235 Ω as the back-gate decreases to 1.6 V.

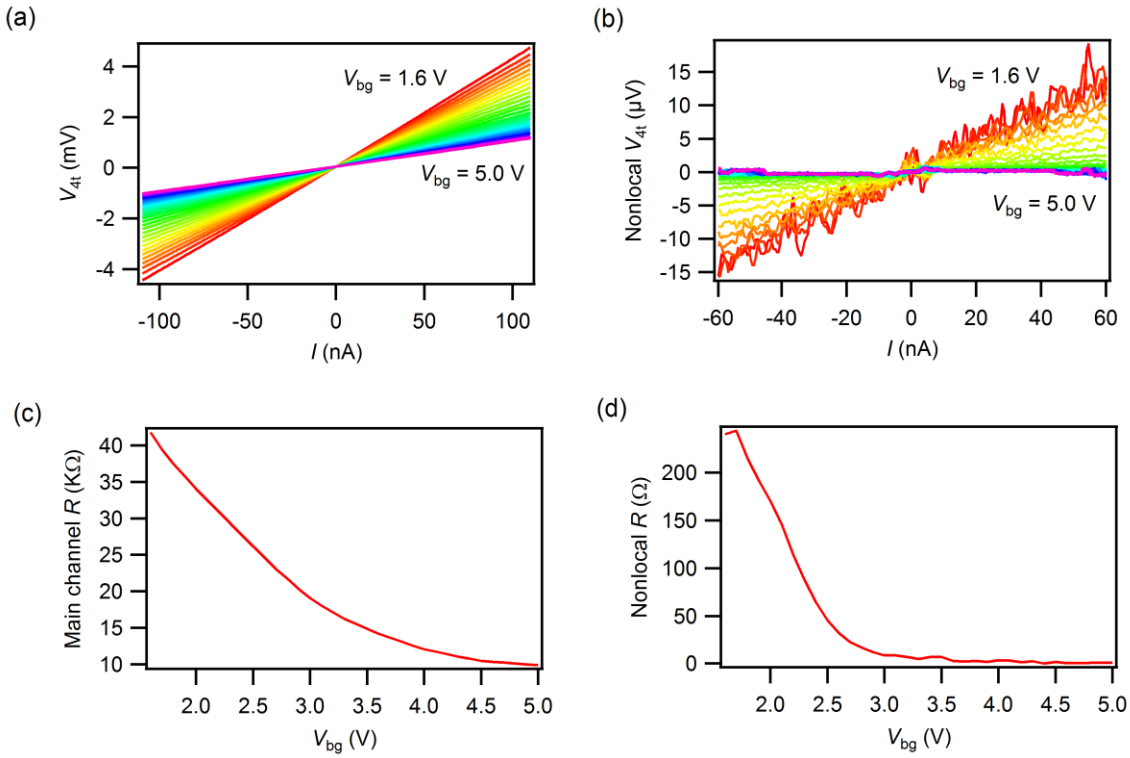

Figure 3-8 Nonlocal resistance change as the back-gate change. (a), Main channel local 4-terminal IV curves at different back-gates. (b), Nonlocal four-terminal IV curves at different back-gates. (c), Main channel 4-terminal resistance via back-gate dependence. (d), Nonlocal four-terminal resistance of back-gate dependence. Measurement conducted at T = 50 mK.

The nonlocal signals can also be tuned using a side-gate, as shown in experiments performed on another sample (Figure 3-9). The nanostructures are the same as the back-gate experiment, except there is a side-gate pointing to the channel. The side-gate is created by the same parameters as the nanostructure writing. The side-gate tuning voltage is one order smaller than the back-gate tuning voltage, while the range of nonlocal resistance change is similar to the back-gate dependence experiments. The nonlocal resistance remains around 0 Ω in the side-gate range of -25 mV to 150 mV, and increases to ~230 Ω as the side-gate is decreased to -150 mV. It is also of note that the main channel four-terminal IV curves show superconductivity except at the -150 mV and the -125 mV side-gate condition, which means that the negative side-gate suppresses the superconductivity of the sample.

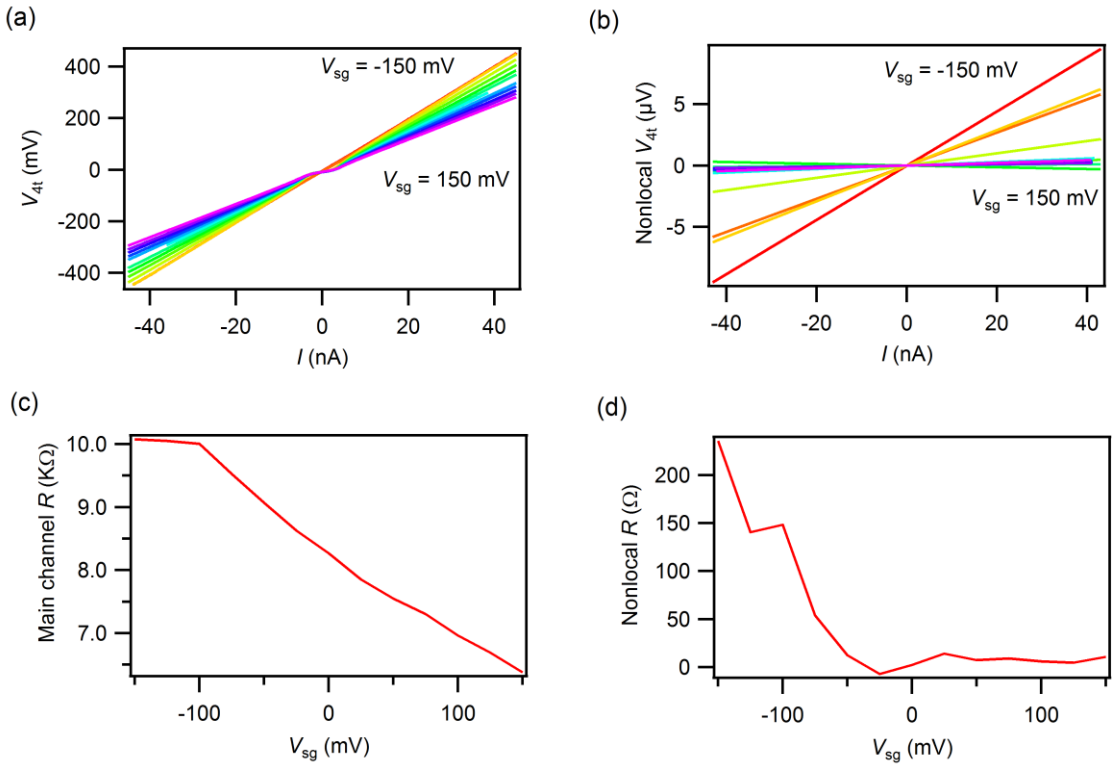

Figure 3-9 Nonlocal resistance change as the side-gate change. (a), Main channel local four-terminal IV curves at different side-gates. (b), Nonlocal four-terminal IV curves at different side-gates. (c), Main channel local four-terminal resistances extracted from linear fitting of the IV curves as a dependence of the side-gate. (d), Nonlocal four-terminal

resistance extracted from the linear fitting of the IV curves as a dependence of the side-gate. The measurement is done at T = 50 mK.

The temperature dependence of the IV curves of this sample are also measured as show in Figure 3-10a. The nonlocal resistance extracted from the IV curves is shown in Figure 3-10b, and increases from 120 Ω to 200 Ω when the temperature decreases from 500 mK to 50 mK. The main channel resistance stays at 10.15 KΩ in this temperature measurement range.

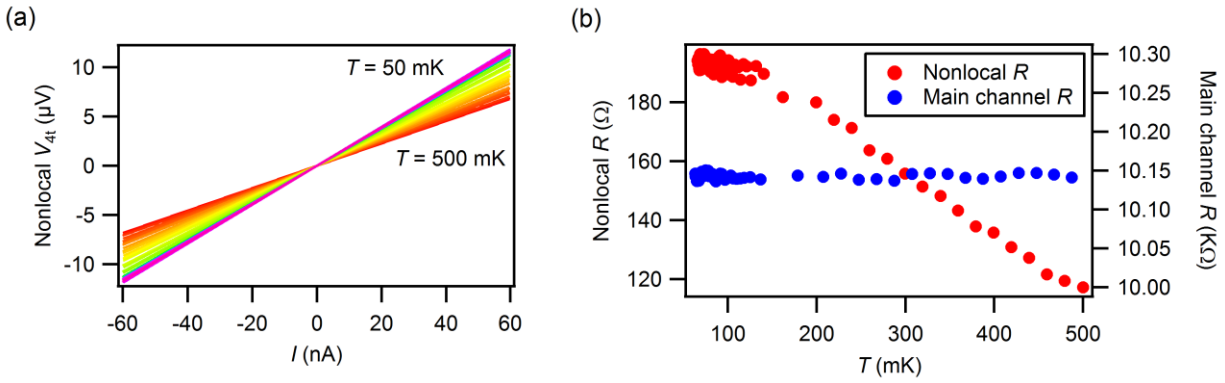

Figure 3-10 Nonlocal resistance change as the temperature change. (a) Nonlocal four-terminal IV curves at different temperatures. (b) Nonlocal four-terminal resistances from linear fitting of the IV as a dependence of the temperature. Measurements are conducted at -0.15 V side-gate.

Another kind of nonlocal signals show peaks in IV measurement. Figure 3-11a shows the IV curves at different frequencies. Besides the peaks in the central area, the curves also show hysteresis since the forward and backward measurement are not overlapped, and the hysteresis becomes larger when the frequency increases. In Figure 3-11b, the upper branch of the 25 mHz frequency IV curves of the field dependence is in plane and pointing at the main channel direction. The width and height of the peaks become smaller as the magnetic field increases, and eventually the peaks at zero current disappear above the 6 T field. Other features also appear and become more obvious upon reaching a 2 T field. The features for positive and negative field are symmetric.

This kind of nonlocal signal can also be tuned by a back-gate as shown in Figure 3-11c; this figure also shows only the upper branch of 25 mHz IV curves. It is obvious that the peaks shift from the left side to the right side as the back-gate increase from -0.78 V to -0.7 V. To show the peaks more clearly, each curve is manually introduced by a 2 μV offset.

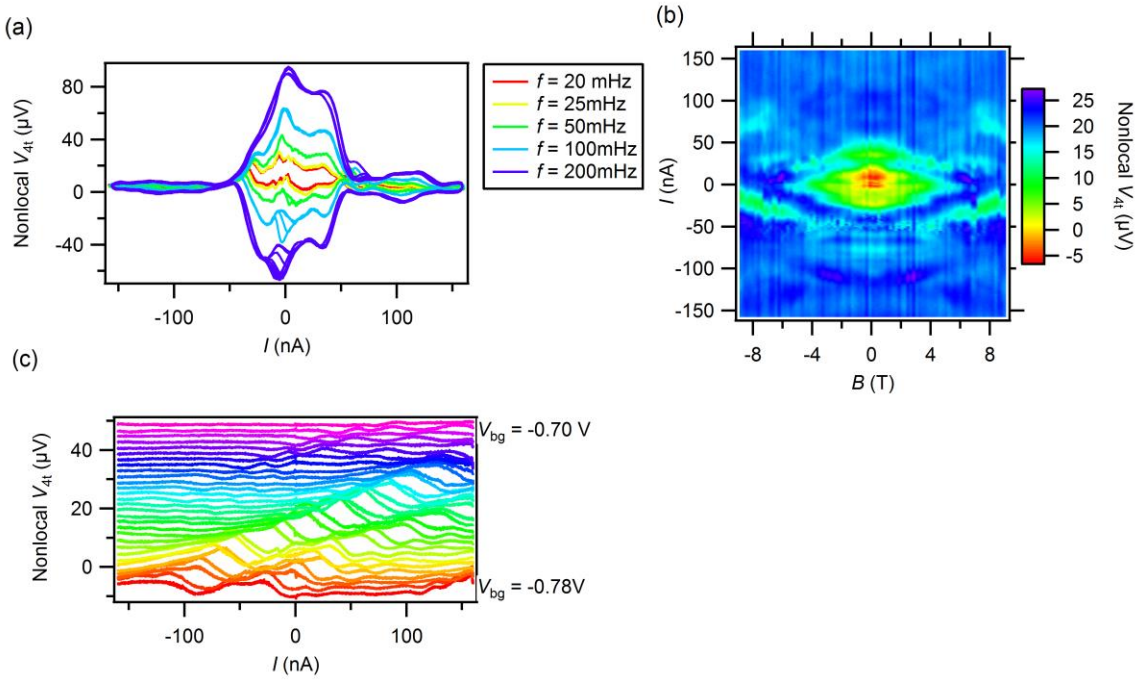

Figure 3-11 Peak shape nonlocal signal. (a), Nonlocal signal IV curves at different measurement frequencies. (b), Upper branch 25 mHz IV curves at a -9 T to 9 T field. (c), Upper branch 25 mHz IV curves at different back-gate biases.

The back-gate tuning ability can also be seen in the field sweep data (Figure 3-12). The back-gate in Figure 3-12 is at -0.75 V, -0.65 V, and -0.55 V from left to right, respectively. The data clearly show that the peaks shift from the negative current branch to the positive current branch as the back-gate increases, with the peak shape and height slightly changed.

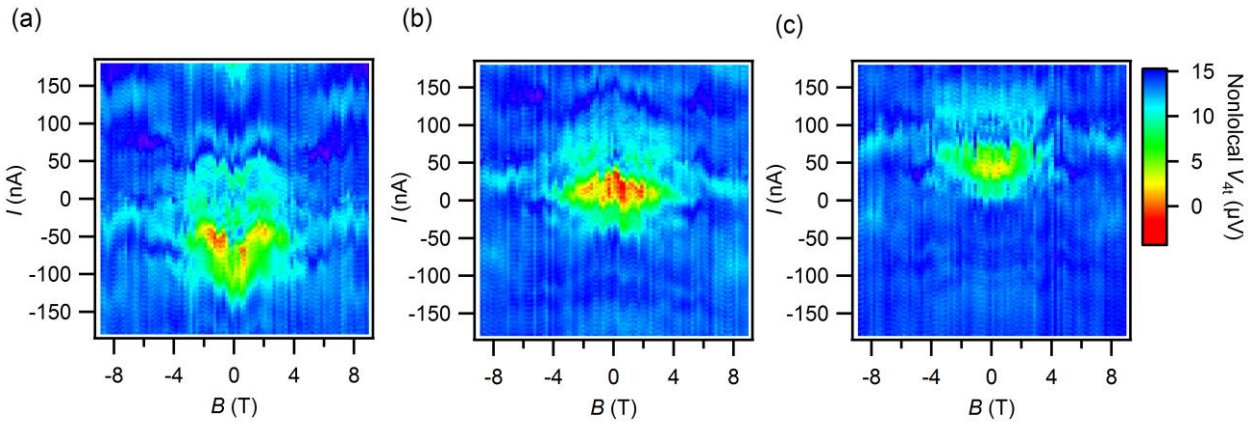

Figure 3-12 Field sweep IV curves at different back-gates. Backgate are at -0.75 V, -0.65 V, -0.55 V from (a) to (c), respectively.

3.5.3 Nonlocal transport at superconducting state

Nonequilibrium processes in superconductors are critical to the development of superconducting nanoelectricity. The application of such devices is limited by the incomplete understanding of the physics of superconducting and quasiparticle (QP) excitations[55,56]. Nonlocal transport in superconducting nanostructures, in which a current source path through two leads is some distance (*d*) away from the voltage detection leads (Figure 3-13a), is often interpreted as a result of charge imbalance (CI) created by injecting quasiparticles into the superconductor through its interface with a normal metal. During the injection, when quasiparticles are created in the superconductor near the interface with the normal metal, the electron and hole branches of the excitation spectrum are unequally populated[57]. This charge density difference, Q or CI, was discovered experimentally by Clarke[58], and contributes to both local and nonlocal transport in superconductors.

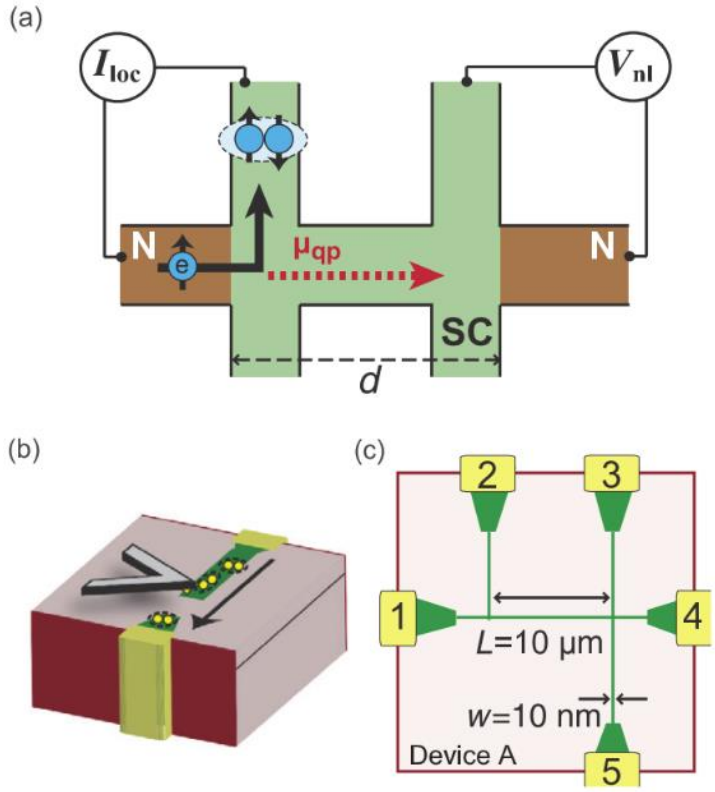

Figure 3-13 General device schematics. (a), Schematic of a nonlocal transport measurement of charge imbalance. Typically, normal leads would be attached to the superconductor. Quasiparticles are injected at the N/S interface (I_{loc}), and the resulting chemical potential detected with voltage leads nonlocally (V_{nl}) on the other side of the channel, a distance (d) away. (b), In $LaAlO_3/SrTiO_3$, c-AFM lithography is used to sketch nanostructures at room temperature that become superconducting below $T_c \sim 200$ mK. (c), Schematic for a five-terminal nanostructure, device A. In general, the $LaAlO_3/SrTiO_3$ devices are multi-terminal nanostructures presumed to be superconducting in all of the leads.

The origin of nonlocal transport in superconducting nanowires is not limited to charge imbalance; another important case involves crossed Andreev reflection (CAR), which is used to detect and study electron entanglement in superconductors. The superconducting coherence lengths ($\xi \sim 100$ nm) are smaller by several orders of magnitude compared to the charge imbalance length scale ($\Lambda_Q \sim$ 1-10 μm), so the nonlocal signals from this charge imbalance will usually

dominate in larger scale devices. CI phenomena have been studied in metallic superconductors and interfaces with ferromagnetic leads; spin-dependent phenomena can also be studied by CI.

Multiply connected and reconfigurable nanostructures can be created on the $LaAlO_3/SrTiO_3$ interface, and these nanostructures show nonlocal signals in four-terminal resistance studies that may be interpreted as signatures of CI. Additionally, the superconductivity in $LaAlO_3/SrTiO_3$ coexists with ferromagnetism, and strong spin-orbit coupling. Moreover, both superconductivity and spin-orbit coupling can be tuned by electric fields and easily applied by connecting a back-gate to the samples.

The literature reflects much work geared towards understanding CI effects in nanowires near T_c and addressing the divergence from the existing theory when $T \approx T_c$. In order to better understand the physics in $LaAlO_3/SrTiO_3$ nanostructure platform, we analyze(d) nonlocal transport effects in $LaAlO_3/SrTiO_3$ nanostructures. With superconductivity in local measurement, nonlocal effects can be observed as a result of pair-breaking near the superconducting critical values. The nonlocal resistance associated with charge imbalance is expected to increase as the temperature gets closer to the superconducting critical temperature, as well as similar dependence behaviors of the magnetic field and the bias current. The coexistence of ferromagnetism and spin-orbit coupling affecting the nonlocal transport properties is also discussed here.

The device schematics are shown in Figure 3-14a-b. To carry out transport measurements, the current is sourced between lead "1" and lead "2" by applying a voltage, V_s, to lead "1" and holding lead "2" on the virtual ground. The voltage difference ($V_{34} = V_3 - V_4$) is measured simultaneously. The differential resistance ($R_{12,34} = dV_{34}/dI_{12}$) is calculated numerically. To distinguish resistance for superconducting states and normal states, we use the notations

$R^C_{12,34} = R_{12,34}(I < I_{c)}$ and $R^N_{12,34} = R_{12,34}(I > I_{c)}$, respectively, where I_c is the critical current for superconductivity.

Figure 3-14a shows IV curves for both the four-terminal local and nonlocal configurations of device A, a five-terminal Hall bar nanostructure (Figure 3-13c), at temperature T = 50 mK. The local four-terminal $R^C_{14,25} = 0.07\ h/e^2$ is finite when the current is below the critical current I_c = 7 nA. A similar finite resistance in the superconducting state has been reported previously[59]. The nonlocal IV curve is also plotted in Figure 3-14a. The nonlocal voltage V_{25} is proportional to the bias current I_{34} and peaks at the local four-terminal critical current I_c. The nonlocal voltage is suppressed as the current exceeds I_c. The nonlocal differential resistance is $R_{34,25}$ = -200 Ω at a zero current bias (Figure 3-14b). As the current increases, the nonlocal resistance changes sign before peaking at $R_{34,25}$ = 300 Ω, when the current is near the local critical current I_c. Here, the effective separation between current path and voltage leads in the nonlocal configuration is of order d ~ 10 nm, which is one order of magnitude smaller than the superconducting coherence length ξ ~ 100 nm.

Figure 3-14b shows three differential nonlocal resistance curves for different configurations, including the one in Figure 3-14a. One configuration has larger peak magnitude of the nonlocal resistance ($R_{15,34}$ = 600 Ω) while another configuration has nearly vanishing nonlocal resistance ($R_{45,13} \approx$ 50 Ω). This nonlocal resistance dependence on the configurations suggests a dependence on the microscopic details of the current path and/or the leads that are used to detect the nonlocal voltage. We notice that the sign of the nonlocal resistance contains some ambiguity. This ambiguity should not come from the leads as no intentional differences are introduced during the sample processing and all of the leads are therefore presumed to be superconducting.

Regardless of its actual value, the sign of the nonlocal resistance always switches around the local critical current I_c.

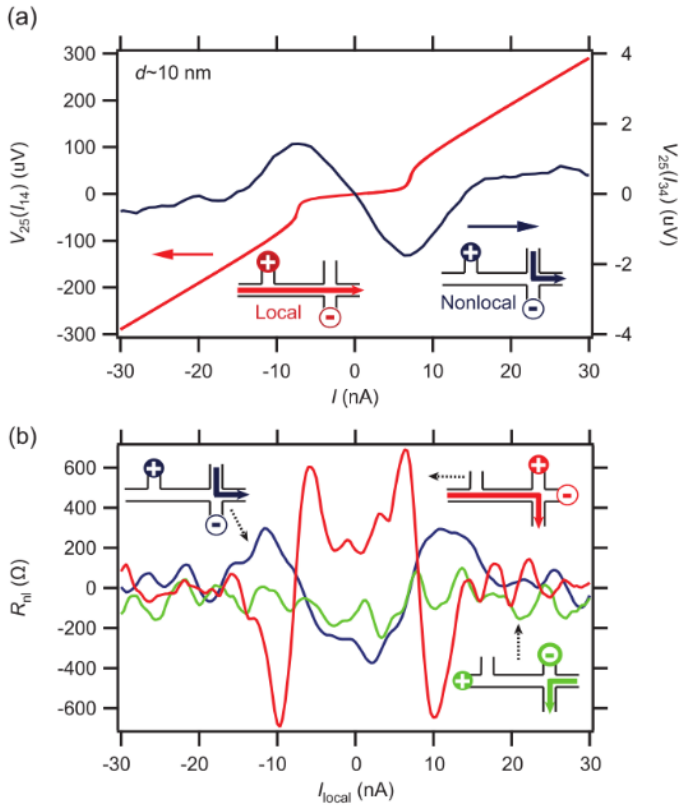

Figure 3-14 Transport measurement. (a), Local four-terminal IV curve (left axis, red) and nonlocal IV curve (right axis, blue) obtained for device A with the lead configurations shown in the graphic insets. The nonlocal voltage peaks at $I \approx I_c$ before gradually diminishing for higher currents. (b), Differential resistance dV/dI for device A shown for three configurations of the voltage and current leads, including the configuration in (a). The nonlocal resistance changes sign near the critical current, and the magnitudes of the nonlocal resistance differ for different configurations of the leads. Numerical subscripts correspond to lead numbers for device A as shown in Figure 3-13.

Figure 3-15 shows local IV and nonlocal dV/dI curves for two similar Hall bar devices. In these two devices, nonlocal resistances are observed for larger values of d = 1.5-6 μm, which exceeds the $LaAlO_3/SrTiO_3$ 2D coherence length of $\xi \sim 100$ nm. For device B, shown in Figure 3-15a, the nonlocal resistance is positive at the zero bias, and decreases below zero then increases

to above zero again, as the current increases toward I_c. Figure 3-15b shows that the nonlocal resistance for device C is negative at a zero bias, and increases to greater than zero as the current is increased, but only changes sign once before reaching I_c. Through a long channel of d = 6 μm, we can still observe nonlocal transport phenomena, which may indicate that this is related to a charge imbalance phenomenon since d is two orders larger than ξ, but is comparable to charge imbalance lengths Λ_Q in metallic superconductors.

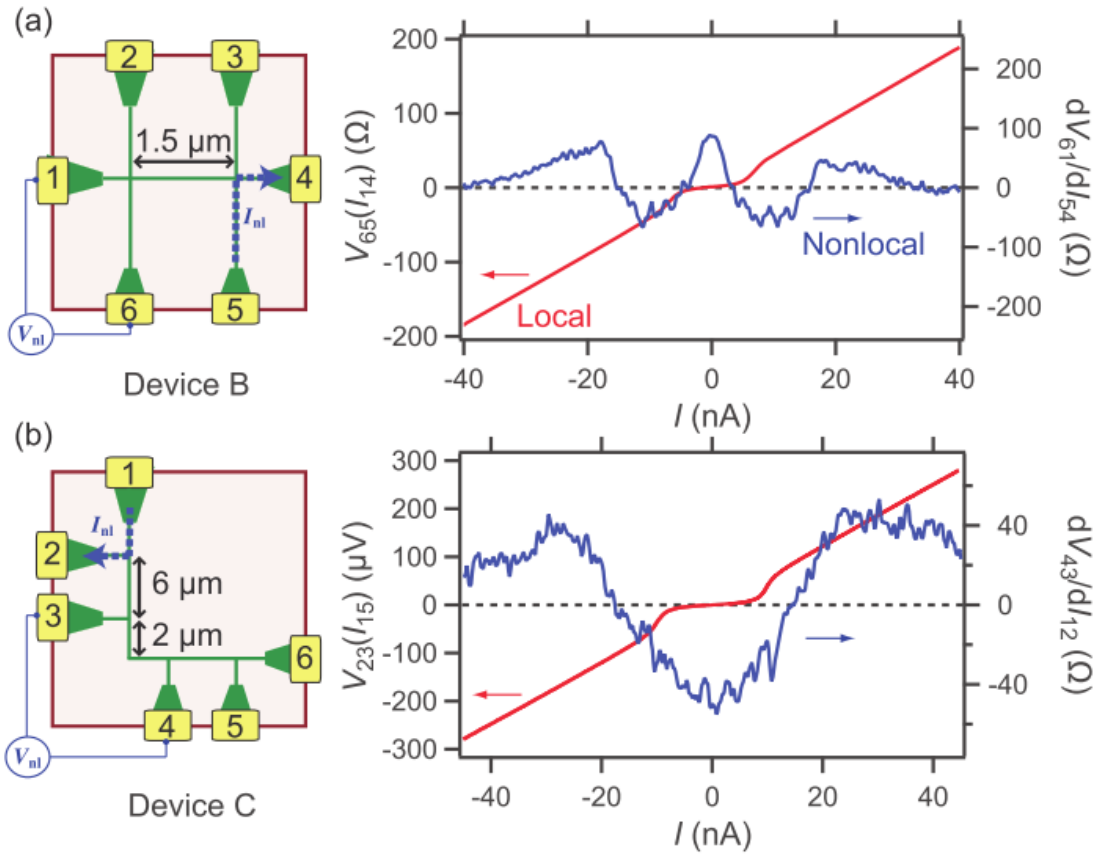

Figure 3-15 Local four-terminal IV curves and nonlocal dV /dI curves. (a), Device B, and (b), device C, with measurement configurations placing the voltage leads microns away from the current path (d >> ξ). The nonlocal resistance again changes sign near $I \approx I_c$. The sign of the nonlocal resistance switches more times in (a) than in (b), although there are no intentional differences in the device fabrication, other than the geometry shown in the schematics.

There is a correlation between the nonlocal signal and superconductivity, as shown in Figure 3-16, in which the B dependence of the nonlocal resistance is compared with the local resistance for device C. The magnitudes and signs of the nonlocal signal are correlated to suppression or enhancement of the local transport superconductivity. The nonlocal resistance (Figure 3-16a) changes sign near the critical local transport current I_c (Figure 3-16b). The current value for which the nonlocal resistance changes sign decreases as the field increases which also contributes to the decrease of local I_c. This is shown as Figure 3-16c, and for all magnetic field H, the nonlocal resistance switches sign around $I_c = I_c(H)$. When comparing the nonlocal and local resistance plots as in Figure 3-16c, the nonlocal resistance reaches a maximum at a finite magnetic field value of $\mu_0 H \approx 500$ mT. This maximum of nonlocal resistance corresponds to the field at which the local superconductivity resistance peaks at $I = I_c$ and begins to decrease significantly in magnitude. The I_c itself also decreases significantly as field increases since the superconductivity is extinguished and quasiparticles excitations are dominating. However, for $\mu_0 H < 500$ mT, the nonlocal resistance is lower than the maximum value, which is expected since fewer quasiparticles remain at $H = 0$, but the nonlocal resistance remains finite at $H = 0$. The fact that the local superconductivity resistance remains finite at $H = 0$ also suggests that quasiparticles excitations occur under this condition.

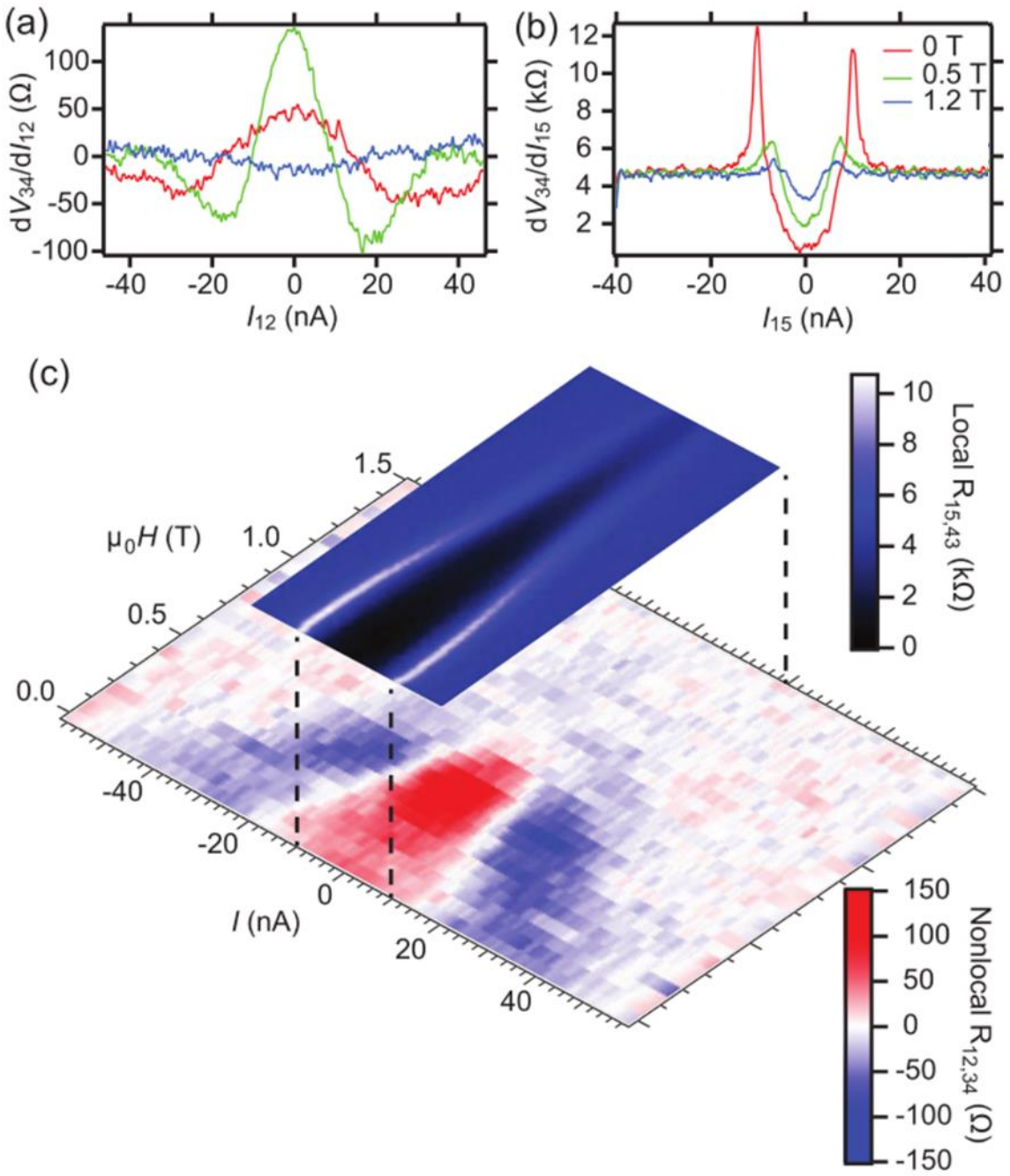

Figure 3-16 In-plane magnetic-field dependence. Dependence of the (a) nonlocal and (b) local four-terminal resistances. Shown in (a) and (b) are curves at three different magnetic fields. (c), Complete magnetic-field dependence over the range $\mu_0 H$ = 0-1.5 T. The nonlocal resistance is clearly associated with superconductivity, peaking as the superconductivity is suppressed, where the pair breaking is enhanced ($\mu_0 H \approx$ 0.5 -1.0 T). The nonlocal resistance also changes sign at $I \approx I_c$ for all fields

Similar to tuning superconductivity by magnetic field, superconductivity can also be tuned by changing the back-gate leading to modulation of the nonlocal resistance strength. Figure 3-17 shows the dependence of nonlocal resistance and local resistance on the back-gate voltage (V_{bg}) for device B. The current at which the nonlocal resistance changes sign also tracks well with I_c, as before. As V_{bg} is increased, the nonlocal resistance peaks at $V_{bg} = 0.5$ V. As V_{bg} is increased further, the nonlocal resistance is suppressed as the superconductivity is suppressed. For $V_{bg} < 0$, superconductivity is strongest, but the nonlocal resistance peaks broaden and appear to obscure the features observed at lower biases for a larger gate voltage.

All of the nonlocal resistances described here are related to the existence of superconductivity. Peaking of nonlocal resistance near the critical current is suggestive of charge imbalance. However, the interpretation of how charge imbalance is created here is not straightforward, since the whole device is presumed to be superconducting. Typically CI may be created at a superconducting/normal interface or tunnel junction. In our device, not only the quasi-1D Hall bar structures, but also the large 2D virtual electrodes, are created on the superconducting 2DEL interface. The fact that the sign of nonlocal resistance depends on the configuration of measurement indicates a dependence on the microscopic details within the device.

Several possibilities arise for the introduction of charged perturbations that are necessary for the creation of charge imbalance. First, the charge injection may occur at the normal Au contacts that were deposited to contact the $LaAlO_3/SrTiO_3$ interface. Some Au contacts are less than 10 μm from the nanostructure which is comparable to the charge imbalance length Λ_Q. The second possibility is the existence of hot spots which, in a normal state, act as sources of quasiparticle injection into the superconducting region. Hot spots were proposed as one mechanism to explain the finite superconducting resistance, which relates to these data. Outside

of the normal state hot spots, the relevant length scale is the quasiparticle diffusion length, equal to Λ_Q. In this scenario, the width of the hot spots necessarily exceeds the coherence length of the superconductor. Finally, the coexistence of superconductivity, ferromagnetism, and strong spin-orbit coupling must be considered. In particular, the magnetism and superconductivity may be inhomogeneous and cause quasiparticle excitations at intrinsic ferromagnetic/superconducting interfaces.

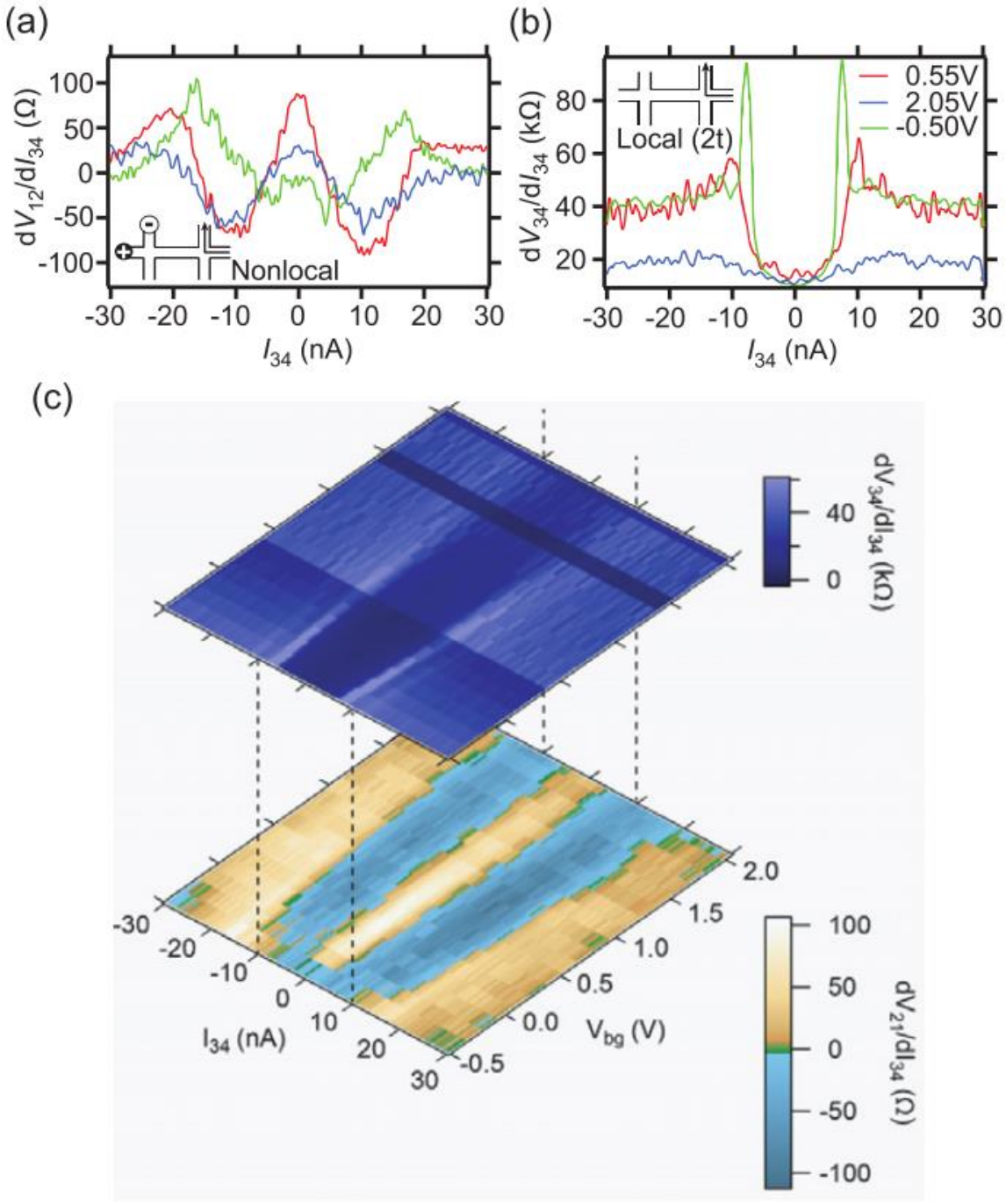

Figure 3-17 Back gate voltage V_{bg} dependence. Dependence of the (a) nonlocal and (b) local two-terminal resistances. Shown in (a) and (b) are curves at three different back gate voltages (V_{bg} = −0.50 V, 0.55 V, 2.05 V). (c), Complete back gate dependence over the range V_{bg} = −0.50 to V_{bg} = +2.0 V. The nonlocal resistance is again clearly associated with superconductivity and changes sign at $I \approx I+$ for all V_{bg}.

Although the primary signatures reported here indicate a significant contribution from quasiparticle CI, some characteristics are still puzzling. For example, the nonlocal resistance often changes sign, several times in some devices. Charge imbalances created through the same lead configuration should retain the same sign, but other phenomena in superconductors are manifest in nonlocal resistances with opposing signs. For example, work has been done over the past several years to study nonlocal transport phenomena of crossed Andreev reflection (CAR) and elastic co-tunneling (EC), both of which occur at much lower biases, and have limited nonlocal distances within the superconducting coherence length[46,60,61]. In most cases, these two phenomena compete with each other, and are observable in nonlocal resistance measurements since they have opposite signs. In particular, the switching of the nonlocal resistance sign with increasing voltage or current bias was attributed to the crossover among CI, CAR, and EC[46]. Considering the inhomogeneous superconducting and ferromagnetic states at the $LaAlO_3/SrTiO_3$ interface may provide an explanation for the creation of these or other spin-dependent effects, if present. The majority of the data reported here, however, are obtained at micron length scales, two orders of magnitude larger than the superconducting coherence length in $LaAlO_3/SrTiO_3$, and they are consistent with typical Λ_Q for charge imbalance.

3.6 CONCLUSION

$LaAlO_3/SrTiO_3$ 2DEL interfaces show a variety of properties such as metal-insulator transition, superconductivity, ferromagnetism, and spin-orbit coupling. Furthermore, with the help of c-AFM, one can create 1D nano structures at the interface which show remarkable anomalous phenomena. The room temperature mobility enhancement of 1D nanowires at the $LaAlO_3/SrTiO_3$

interface make this a promising system for practical applications. The nonlocal transport results indicate there might be spin transport involvement which make this system a great potential for next-generation spin devices. Besides these, the discovery of nonlocal transport in the superconducting state makes this system more complex, but also more attractive for research.

4.0 CONFINED NANO STRUCTURE IN 1D NANO WIRES

Previous chapters demonstrate the potential of $LaAlO_3/SrTiO_3$ 2DEL interfaces, on which we can create nanowire structures. Those quasi-1D structures present several novel phenomena, e.g. the mobility enhancement in 1D nanowires, and the nonlocal transport for both normal states and superconducting states. In this chapter, we create confined nanostructures embedded in 1D nano wires on the $LaAlO_3/SrTiO_3$ interface; these structures not only help us better understand the physics behind the results, but also propose a new material platform for investigating quantum transport in 1D systems.

For quantum dot confined nano structure section, I am one of three who collected experimental data, and I also participated in the discussion of the theory and its explanations. For quantum point contact confined nano structure section, I was the primary person to collect and analyze the data. The new experimental results are based on the novel lithography techniques and LabVIEW programs I designed.

4.1 INTRODUCTION

$SrTiO_3$ is the best known superconducting semiconductor as it exhibits an extremely low carrier density[62] threshold (as low as 10^{17} cm^{-3}) for superconductivity. This, in addition to the similar phase diagram with high-temperature superconductors, suggest that there is an unconventional pairing mechanism in $SrTiO_3$. In 1969 it was predicted that low-density superconductors should have unconventional real-space electron paring without

superconductivity[63]. Above a critical temperature or a critical field, electrons can form tightly bound pairs, and below a critical temperature and a critical field, Bose-Einstein condensation (BEC) occurs and superconductivity emerges. However, direct experiments suggest that this has not been reported previously as superconductivity properties of $SrTiO_3$ have been studied by transport measurement[64], tunneling spectroscopy[65], and the Nernst effect[62].

4.2 SAMPLE GROWTH

3.4 u.c. $LaAlO_3/SrTiO_3$ samples are grown using the PLD method by our collaborator Prof. Chang-Beom Eom's group. Details about sample growth are discussed in Section 1.2.

4.3 QUANTUM DOT CONFINED NANO STRUCTURE

4.3.1 Device geometry and general transport characteristics

Figure 4-1a shows the schematic of the device, in which the red background represents an insulating canvas while the green lines represent nanowires written by the c-AFM technique. The typical nanowire (between leads "1" and "5") width of $w \approx 5$ nm is determined by the erasing method on the same canvas with same AFM tip. Three voltage sensing leads (leads "2" to "4") separate a 5 um main channel into two equal length segments. The upper segment between leads "2" and "3" is the control segment. This is a "open" wire, that is, a wire without a barrier, while the lower segment between leads "3" and "4" contains an $L_{QD} = 1$ μm quantum dot (QD) bounded

by two barriers which is created by a small voltage (<1 V) erasing cross the nanowire. A side-gate is also written parallel, and 800 nm away from the main channel, it is used to tune the chemical potential of both the "open" wire and the QD, and modulate the coupling between QD and external leads.

Figure 4-1b and Figure 4-1c show the low temperature (50 mK) differential conductance dI/dV versus the side-gate V_{sg}, and a four-terminal voltage, V_{23} and V_{34} for the "open" wire and the QD structure, respectively. The "open" wire segment shows superconductivity through the whole side-gate range while the QD segment shows a sequence of diamond-shaped patterns which are basically insulating regions with conductance as low as 10^{-2} e^2/h, where e is the electronic charge and h is the Planck's constant. In the higher sidegate range (> -10 mV), the diamonds disappear and the supercurrent recovers, and there are also some resonant patterns discussed later.

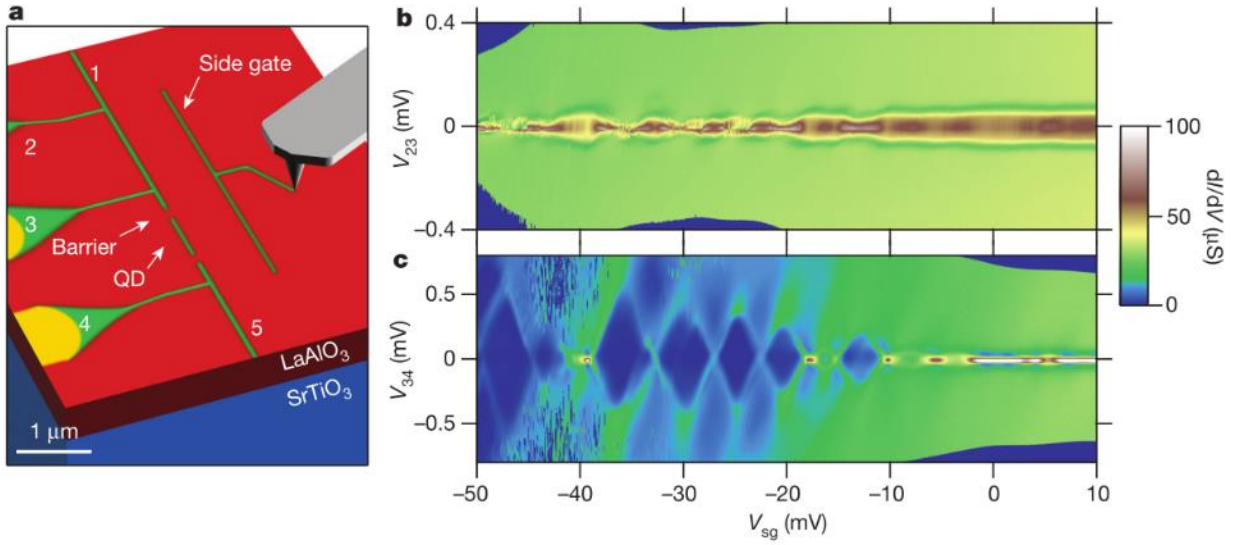

Figure 4-1 Device geometry and transport characteristics. **(**a), Device schematic. The nanowire width is w = 5 nm, the nanowire QD length is 1 µm, and barriers are 0.75 µm away from the sense leads "3" and "4". The length of the open wire is 2.5 µm, equal to the nanowire QD length plus total distances from barrier to sense leads. (b), Device

dI/dV characteristics as a function of four-terminal voltage V_{23} and side gate voltage V_{sg} in the open wire. (c), dI/dV characteristics of the QD measured simultaneously with data shown in (b).

The diamonds patterns here can be described as a Coulomb blockade effect as shown in Figure 4-2. Here, QD is a structure connected to two electrodes known as the source and the drain, and a gate that is capacitively coupled to the QD. The QD itself has discrete energy level ΔE due to spatial confinement, and these energy levels can be tuned by the gate. In a blocking state as shown in Figure 4-2a, the Fermi energy of the source electrode lies between the energy levels of the QD, so no accessible energy levels are within tunneling range of the electron, leading to an insulating state of the system. By tuning the QD by the gate, eventually the energy level of the QD will align to the Femi level of the source electrode causing the electron to tunnel from the source electrode to the QD, then tunnel to the drain electrode (Figure 4-2b). This process leads to a transmission state where the current can go through the system. By combine-tuning the gate and various source-drain biases, the conductance will show a diamond-like pattern in a 2D plot which are Coulomb diamonds. There are three criteria which have to be met in order to achieve the Coulomb blockade:

1. The source-drain bias must be lower than ΔE
2. The thermal energy $k_B T$ must below $\Delta E/2$
3. The tunneling resistance should be greater than h/e^2

Generally, ΔE is the energy required to change the QD state from N to N+1 electrons and $\Delta E(N)$ is the sum of charging energy E_C (capacitance energy) and the orbital energy δE of the system: $\Delta E(N) = E_c(N) + \delta E(N)$. ΔE is usually dominated by E_c in a normal QD system for semiconductors, carbon nanotubes, and superconductors[66], resulting in evenly spaced diamonds

pattern. However, in our device, ΔE changes from 640 μeV at V_{sg} = -47 mV to 210 μeV at V_{sg} = -13 mV (Figure 4-1). This non-uniform ΔE shows that the orbital energy δE dominates ΔE.

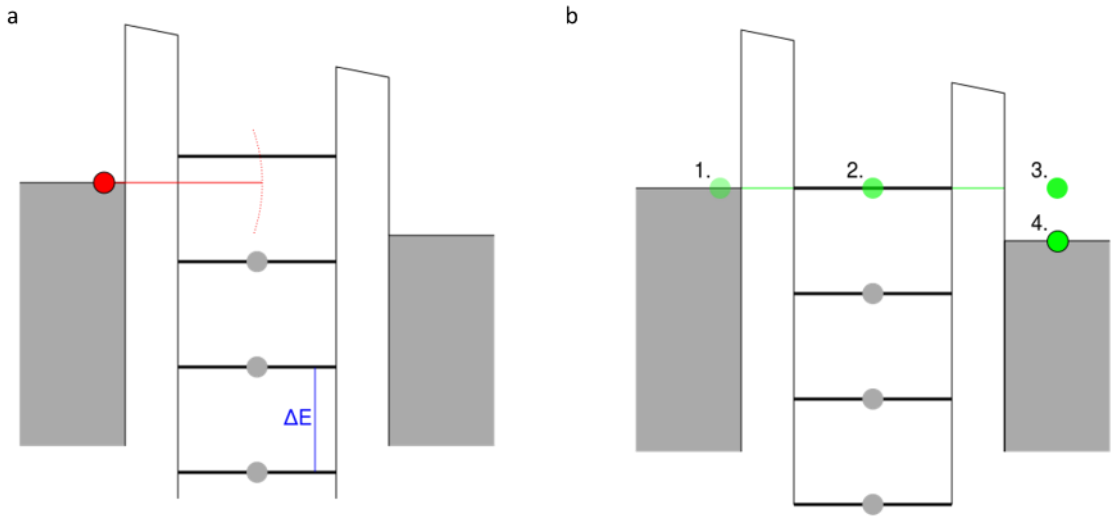

Figure 4-2 Simple diagram for Coulomb blockade. **(**a), Blocking state. (b), Transmission state when the Fermi energy of the left electrode is equal to the energy state in the QD.

4.3.2 Electron pairing without superconductivity

Figure 4-3a-e shows the evolution of the conductance diamonds as a function of an out-of-plane magnetic field *B*. The bottom insert figures are a zero bias line cut of the 2D plot. At B = 0 T, three diamonds (two zero bias peaks – ZBPs) are visible in the range, at a field below 2 T, the diamonds pattern remains relatively unchanged except for some ZBPs change in width. At B = 3 T, new diamonds emerge and become larger as the magnetic field is increased further to B = 4 T. Also the ZBPs cut clearly shows the peak number change from two to four as field increase from 2 T to 4 T. A high resolution scan of the conductance versus the gate voltage at zero bias is shown

as Figure 4-3f enables the ZBPs to be extracted and fitted versus the magnetic field. A ZBP around V_{sg} = -27 mV splits above a critical field B_p around 1.8 T which breaks the electron pairing. However, the striking finding is that this pairing critical field is one order of magnitude larger than the superconductivity critical field ~0.2 T. This can be proven by the superconducting resonance of V_{sg} = -19 mV ZBPs which also has the critical paring field with a successively smaller value. For $|B| > B_p$, the energy difference between the split peaks E_z increases linearly (Zeeman-like) with magnetic field $E_Z = g\mu_B(B - B_p)$. The Lande g factor can be calculated to form the slope by taking into account the experimentally determined coupling factor α at ~0.1 eVV^{-1}. Interestingly, at a higher field, the split ZBPs occasionally intersect and combine together (re-entrant pairing) before separating again (for example, at V_{sg} = -25 mV). The energy associated with B_p, $E_p = g\mu_B B_p$, for the four devices in Figure 4-3h is non-monotonical with increasing V_{sg} for each device.

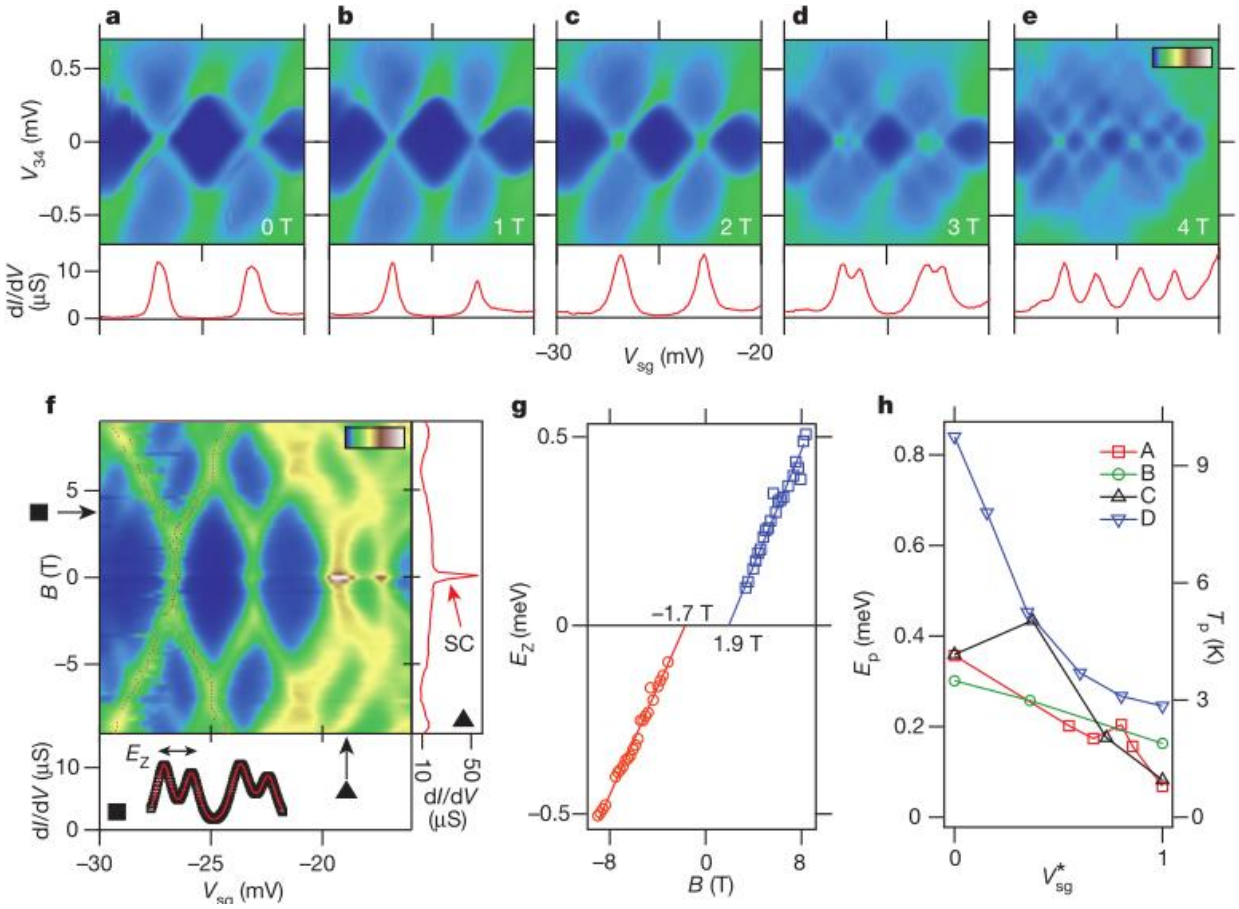

Figure 4-3 Out of plane magnetic field dependence. **(**a–e), Top panels, d*I*/d*V* dependence on V_{34} and V_{sg} at B = 0 to 4 T. New diamonds emerge at B = 3 T in (d). Color scale (top right): 0–80 μS. Bottom panels, zero-bias line profiles in (a–e). (f), Top panel, magnetic field dependence of ZBPs. All the ZBPs split above some critical pairing fields, B_p. Color scale: 0–40 μS. Bottom panel, line profile (black markers) of ZBP at B = 3.8 T, in the top panel, indicated by the horizontal black arrow. The red line is the fit to extract peak locations. Right pane, line profile at V_{sg} = -19 mV indicated by the vertical black arrow. The sharp peak at B = 0 is due to superconductivity (SC). (g), Energy difference E_Z of two Zeeman splitting branches of the ZBP at V_{sg} = -27 mV. The B_p and g factor can be extracted from the intercepts and slopes in the linear fits. (h), E_p dependence on rescaled V^*_{sg} for all available ZBP splitting in four devices, where $V^*_{sg} = (V_{sg} - V^{\min}_{sg}) / (V^{\max}_{sg} - V^{\min}_{sg})$, and $V^{\max}_{sg}, V^{\min}_{sg}$ are maximum and minimum ZBP locations of each device. E_p roughly decrease with increasing V_{sg}.

Figure 4-4 shows the temperature dependence transport measurements results. These results show B_p to be nearly independent of the temperature, up to T = 900 mK, which is the highest

temperature we measured. Of our four devices, only device B, which shows the lowest B_p, exhibits a threefold suppression at T = 900 mK. Figure 4-4a shows a representative conductance 2D plot versus V_{sg} with B at T = 100 mK. The conductance at B = 6 T shows two well-resolved split peaks at T = 100 mK. As the temperature is increased while the magnetic field is held at 6 T, the ΔV_{sg}, the sidegate difference between two peaks, increases (Figure 4-4c). Assuming the g-factor is constant over this temperature range, this result implies that $dB_p/dT < 0$, which is also consistent with the fitting results in Figure 4-4d.

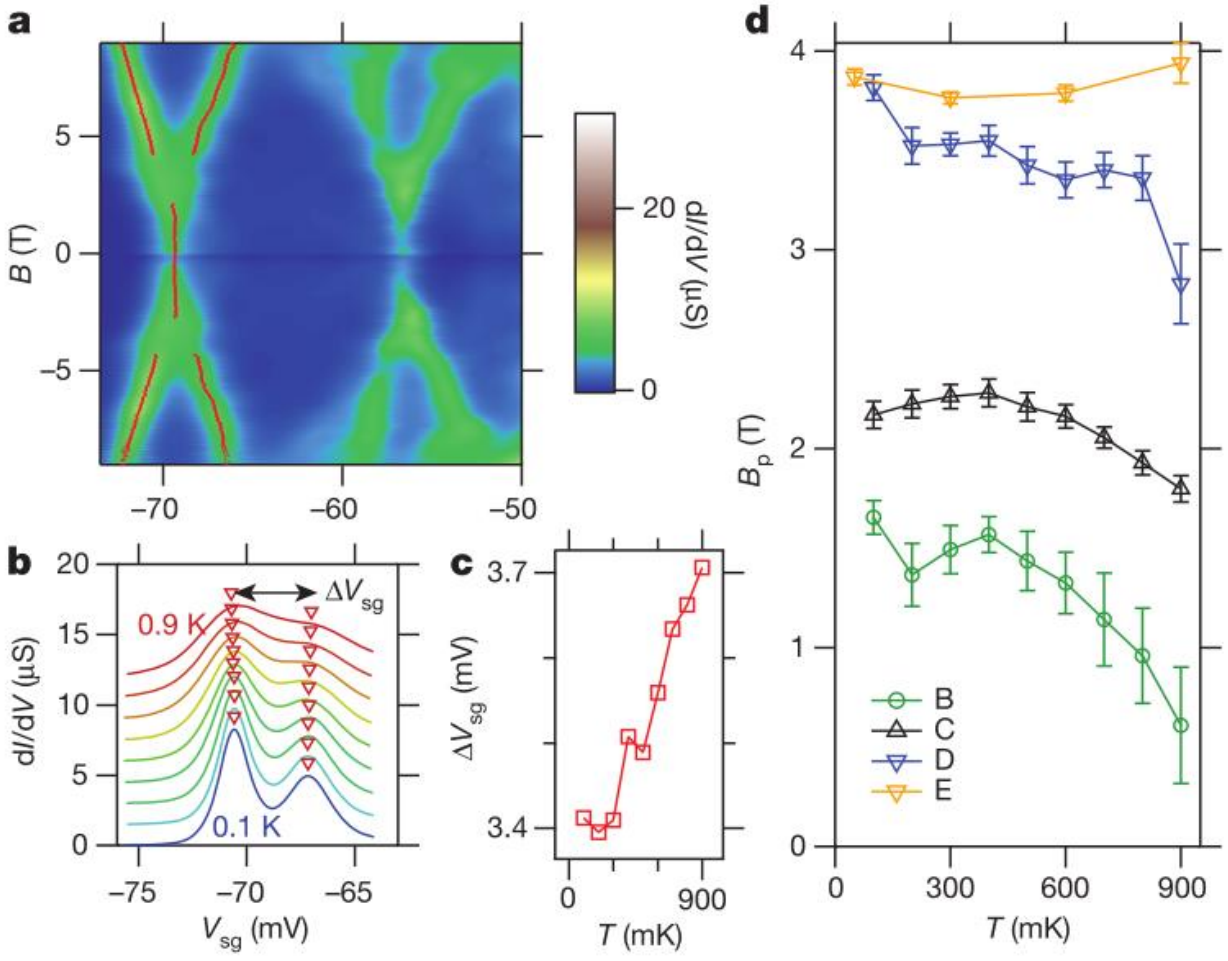

Figure 4-4 Temperature dependence of B_p. (a), Out-of-plane field dependence of ZBPs at T =100 mK. The trace of red dots reveals the actual peak locations extracted by fitting. (b), Line profiles at B = 6 T, of different temperatures from 100 mK (blue) to 900 mK (red) with 100 mK spacing. Red triangles mark actual peak positions and ΔV_{sg} is the

difference between two splitting peak positions. Curves are offset for clarity. (c), ΔV_{sg} in (b) as a function of temperature. A larger ΔV_{sg} at higher temperatures indicates lower B_p. (d), Temperature dependence of B_p for the most isolated ZBP splittings in four devices. B_p in device B, which is the lowest among the four devices, decreases non-monotonically with increasing temperature. Error bars and S.E.M. are from the linear fitting errors of the positive and negative critical pairing fields.

The quantum transport results here for $LaAlO_3/SrTiO_3$ nanowire QDs contrast sharply with conventional Coulomb blockade results in other semiconductor nanostructures[66]. Experiments in Al based superconducting SETs show similar pair tunneling, but only in a superconducting state, and with pair tunneling condition $E_c < 2\Delta$, which means that the paring energy dominates the Coulomb charging energy. However, in $LaAlO_3/SrTiO_3$ samples, the high permittivity of $SrTiO_3$ highly reduces the charge energy for $LaAlO_3/SrTiO_3$ nanowire SETs allowing them to operate in the pair tunneling region. The observed ZBP splitting indicates that the pairing state persists in the magnetic field much larger than superconductivity critical field.

The existence of electron pairing outside of the superconductivity regime does not imply that the electron pairing contributes to the superconductivity itself automatically; however, it would be a remarkable coincidence for these two phenomena to be superimposed without any interrelationship. In fact, the vertical line cut in Figure 4-3f shows a sharp superconductivity enhancement of the ZBP at V_{sg} = -19 mV, which demonstrate that the electron pairing and superconductivity are linked. This enhancement of conductance in the superconducting regime occurs with $B < 2$ T, which is the pairing break field, and demonstrates that the electron pairing is coupled to the superconducting leads.

Several other explanations for the ZBP splitting have been considered. For example, the Kondo ridge in Coulomb diamonds can split above critical field; however, these splits usually occur at a non-zero bias. Furthermore, other Kondo signatures are not observed here. Charge traps

that exists with tunneling barriers can release additional electrons to the device, which can lead to occasional resonance-double features, but the electron pairing features we observed are reproduced in over 50 devices, and do not fit the statistic profile of charge traps. In some ultra-small superconducting grains, quantum fluctuation may promote the even-odd parity energy, which can lead to similar ZBP splitting. However, this effect can only happen at $T < T_c$.

The existence of pre-formed electron pairs in $LaAlO_3/SrTiO_3$ system, forming a superconducting condensate at lower temperatures and lower magnetic fields, follows the paradigm of BEC superconductivity, in which the pairing is local and precedes the formation of the superconductivity. The only well-established physical embodiments of BEC super-fluidity have been in ultra-cold atomic gases, in which the BEC and BCS crossover can be tuned by a Feshbach resonance. For our system, the ability to confine electrons at nanoscale, combined with an inherent affinity for strong pairing, suggests it is an ideal system to explore strongly correlated electronic phases in a solid state material system.

4.3.3 Fabry-perot interference

In 1D geometries, the Fabry-Perot interference has been widely cited as a reliable proof of system-wide quantum coherence. In an analog to optical cavities, carriers are partially reflected at two ends of a nanowire cavity, and the quantum coherence is preserved when the mean free path is longer than the cavity. Interference oscillations due to coherence are observed as the chemical potential is varied, usually by a nearby gate electrode, due to the changing Fermi wavelength. Only exceptionally clean systems have shown this kind of interference e.g., suspended single-wall carbon nanotubes[67], high-mobility graphene structures, and stacking-fault-free III-V nanowires

grown by vapor-liquid-solid techniques[68]. Lithographically defined III-V nanowires are generally prone to localization from interface scattering.

Here, same kind of nanowire cavities, shown in Figure 4-5a, are created at the $LaAlO_3/SrTiO_3$ interface using c-AFM lithography[36] as in previous chapters; however, the side-gate ranges we are focusing on are higher making the overall conductance of the device above zero. There are three distinct transport regimes as a function of the applied magnetic field. Below a critical field $|B| < B_c \sim 0.2$ T, the nanowires are generally superconducting. In the regime $B_c < B < B_p$, where $|B_p| \sim 2$-5 T, the electrons are paired but are no longer superconducting[69]. Finally, in the regime $B > B_p$, the system is driven into the "normal" state, i.e. electrons are unpaired. We first focus on the unpaired regime, $B > B_p$. As a function of V_{sg}, the typical differential conductance dI/dV measurements of the cavity exhibit quasiperiodic oscillations which extend to the non-equilibrium regime, where the four-terminal bias voltage V_{4T} is non-zero. A "checkerboard" pattern characteristic of Fabry-Perot interference[67,68] appears in dI/dV as a function of V_{sg} and V_{4T} for device A. At a finite bias, the range of momentum states participate in transport, causing the conductance resonances to become dampened. A comparison of dI/dV at zero and finite biases (Figure 4-5c) show that the oscillations are out-of-phase, as expected for a Fabry-Perot interference[70].

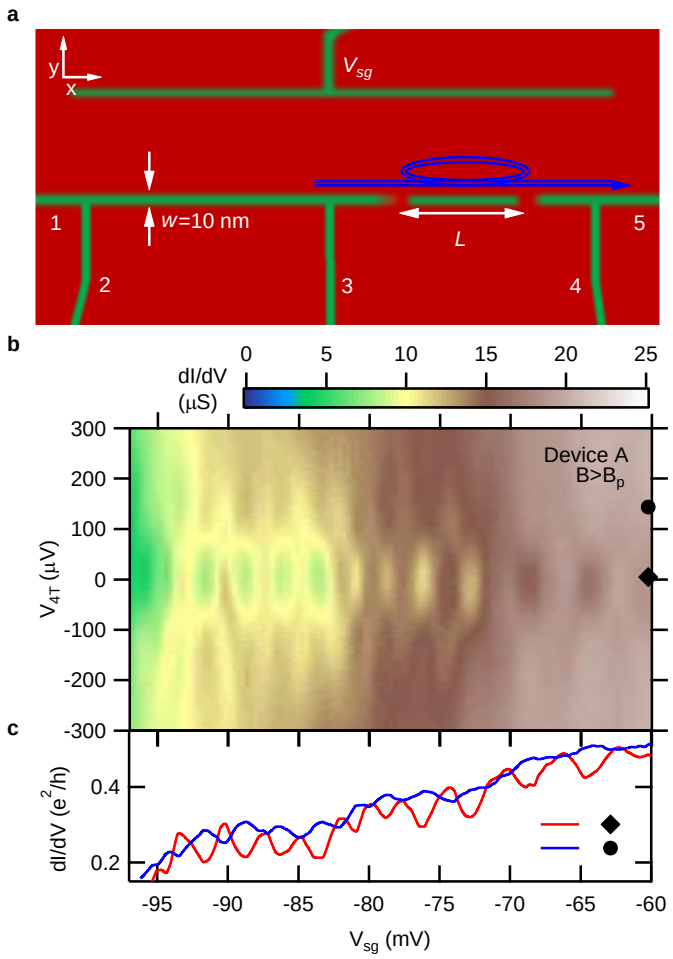

Figure 4-5 Device schematic and Fabry-Perot oscillations. (a), Schematic of cavity device defined by two barriers separated by length *L*. Interference, due to coherent scattering in the cavity, results in conductance oscillations which are periodic in Fermi momentum. (b), Differential conductance (*dI*/*dV*) of device A (*L*=0.25 μm, *B*=3 T) for the cavity (between voltage leads 3 and 4 in (a)) in the normal, unpaired electron state. (c), *dI*/*dV* linecuts at zero-bias (diamond marker) and finite bias (circle marker) are in anti-phase, though the amplitude of the oscillations at finite bias are suppressed.

The regime $B_c < B < B_p \sim 2$ T has been previously identified as a strongly correlated state in which electrons exist as spin-singlet pairs without forming a superconducting condensate[69]. Fascinatingly, signatures of interference persist into this paired regime. Device B (L = 4 μm)

exhibits conductance oscillations in both the normal, unpaired state ($B > B_p$, Figure 4-6a) as well as in the recently discovered paired state ($B_c < B < B_p$, Figure 4-6b). Conductance oscillations occasionally display abrupt changes in frequency, expected when new energy subbands become accessible. In such a multimodal description, the observed periodicity can depend not only on the length of the device, but also on the mass of the subband, and the location of the Fermi energy within a subband, obscuring a direct relationship between device length and the interference V_{sg} period.

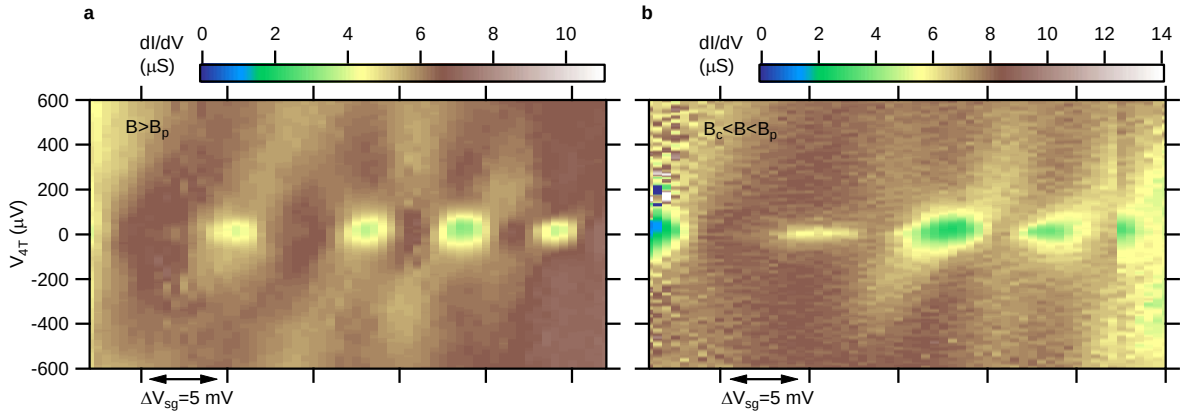

Figure 4-6 Fabry-Perot interference signatures in the normal and paired electron states. **(**a-b), dI/dV vs V_{4T} and V_{sg} of device B (L=4 μm) in both the normal, unpaired electron state ((a), B = 7 T) and the paired electron state ((b), B = 1 T).

The transition between unpaired, paired, and superconducting regimes can be observed in the magnetic field dependence of the trans-conductance (Figure 4-7a). Zero-bias conductance from device C is differentiated with respect to the side-gate; the resulting trans-conductance, dG/dV_{sg}, reveals large oscillations in the superconducting state, which is characterized by a conductance peak below $B < B_c$ (Figure 4-7b). Other than reducing the magnitude of the oscillations, the applied magnetic field has a negligible effect below $B = B_p$; the trans-conductance oscillations of the paired

state are in phase with the superconducting oscillations (Figure 4-7c). Above $B > B_p$, the electron pairs break, and the magnetic field causes significant shifting of the interference pattern.

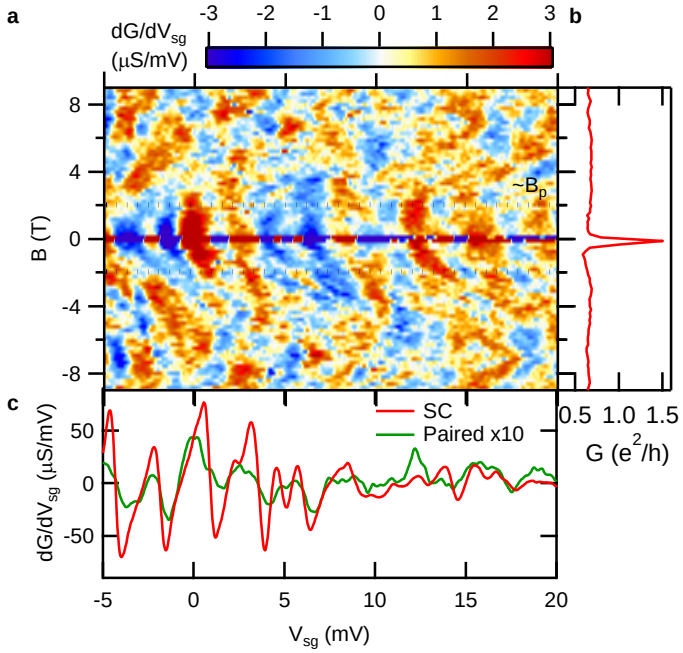

Figure 4-7 Magnetic field dependence of conductance oscillations. (a), Transconductance dG/dV_{sg} from a lock-in amplifier measurement of G at a small (100 μV) bias versus B and V_{sg} for device C (L = 1 μm). Alternating red and blue regions correspond to conductance oscillations. (b), A linecut of G versus B at V_{sg} = 0 mV shows a sharp peak attributed to superconductivity at $B < B_c \sim 0.2$ T. (c), Linecuts of dG/dV_{sg} in the superconducting state (red) and in the paired, non-superconducting state (green). The oscillations in the paired state are an order of magnitude smaller than, but largely the same pattern as, the superconducting oscillations, as seen in (a). As the magnetic field increases above $B_p \sim 2$ T, the electron pairs break and single electron states shift with the field, changing the observed Fabry-Perot patterns.

The existence of Fabry-Perot interference, indicating ballistic transport in quasi-1D $LaAlO_3/SrTiO_3$ nanowires in both the single- and paired-electron states, stands in stark contrast to behavior in higher spatial dimensions. Understanding the distinctive transport in quasi-1D

structures is possibly relevant for transport measurements in 2D $LaAlO_3/SrTiO_3$, where local probes have revealed the existence of narrow channel flow along ferro-elastic domain boundaries[71,72]. A one-dimensional transport, realized here through highly-reconfigurable c-AFM lithography, offers rich physics with many theoretical predictions[73], including charge/spin separation[70] and electron fractionalization[70]. The observation of micrometer-scale quantum interference in the superconducting, paired, and unpaired electron regimes opens new opportunities to explore 1D quantum transport in a strongly correlated electron system.

4.4 QUANTUM POINT CONTACT CONFINED NANO STRUCTURE

One-dimensional (1D) conducting paths play a central role in quantum transport. A key signature of 1D transport is the quantization of conduction at integer multiples of e^2/h, where e is the electron charge and h is the Planck constant. Here we report the development of quasi-1D quantum channels formed at the strongly correlated $LaAlO_3/SrTiO_3$ interface. Using a gate-tunable quantum point contact, we observe quantized conduction in the superconducting, and electron-paired and unpaired regimes. In some devices highly nonlinear corrections to Zeeman splitting are observed, associated with strong pairing interactions. Shubnikov-de Haas-like oscillations, observed as a function of magnetic fields, are quantitatively linked to geometrical confinement in the quasi-1D limit; the increasingly precise conductance quantization with an increasing magnetic field is characteristic of chiral edge channels in the quantum Hall regime.

4.4.1 Device writing and geometry

Nanoscale devices investigated in this study were created by the c-AFM lithography technique in which conducting nanowires at the interface were created by applying a positive voltage to the AFM tip, and similarly created nanowire can also be erased by applying a negative voltage. A schematic of a sketched nano-constriction device is depicted in Figure 4-8. In this structure, a set of trapezoidal shape electrodes (created with +18 V to tip) were created to make the contacts between the patterned gold interface connected electrodes at one end, and the nano-constriction device at the other end through a set of conducting nanowires (created with +15 V to tip) which were used as current, and voltage sensing leads. The typical width of these nanowires is about 10 nm, as determined by analysis of local erasure experiments. In the next step, the active nano-constriction device is created comprised of a nanowire (created with +8 V to tip), and two resistive barriers embedded in it. The resistive barriers were created by applying a pulsed square wave signal of (+1.5/-5) V to the tip with a specific pulse duration.

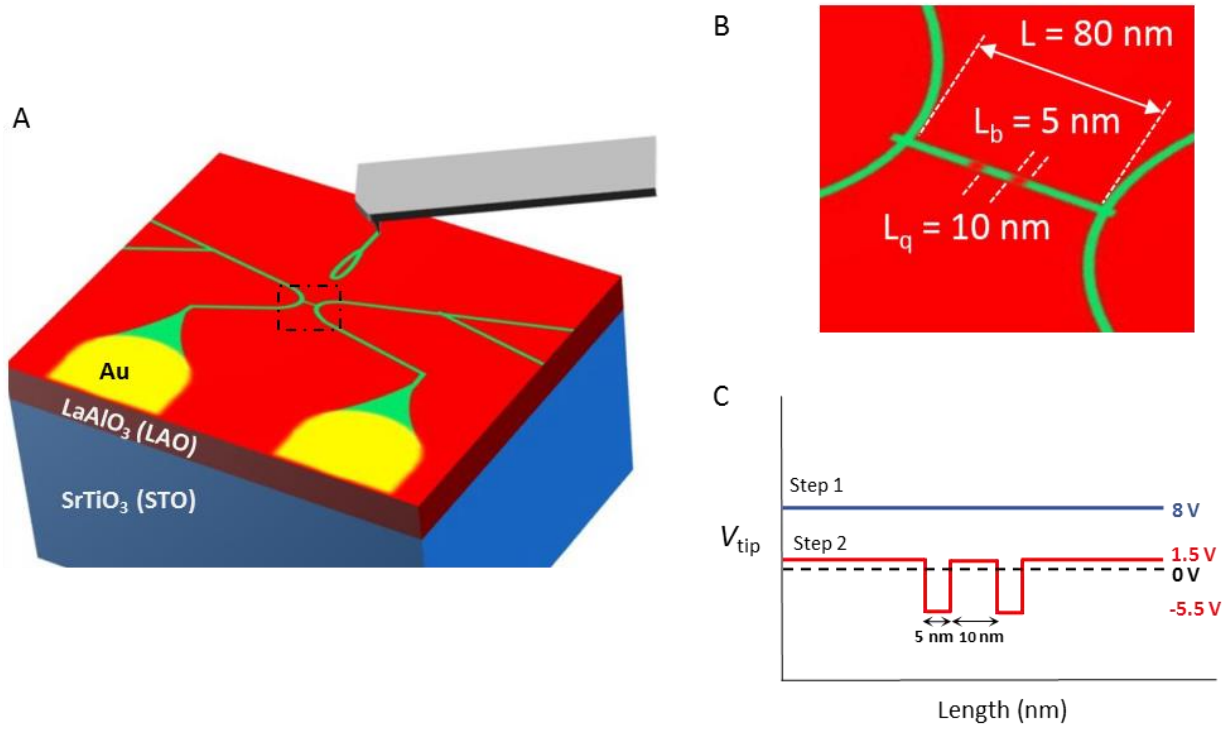

Figure 4-8 Device Schematic with c-AFM writing process. (a) Schematic picture of the $LaAlO_3/SrTiO_3$ device. Green pattern replica to conducting paths at the $LaAlO_3/SrTiO_3$ interface created by c-AFM lithography technique connects the patterned interface connected Au (yellow color) contacts. (b) Zoom-in view of the active nano-constriction of the device consists of a nanowire of length L, and two resistive barriers of length L_b separated by L_q. (c) A tip voltage sequence is applied to the AFM tip to create the device shown in (b).

4.4.2 Electrical characterization

After device-writing at room temperature, to perform transport experiments at cryogenic temperatures, samples were then transferred in the dark in to the Quantum Design-physical property measurement system (QD-PPMS) with a dilution unit capable of reaching 50 mK base temperature, and a 9 T magnetic field. Simultaneous sampling 24-bit data acquisition cards were used to source voltage and acquire amplified voltage signals which come from true differential

voltage amplifiers (Femto model DLPVA) with a one TΩ input impedance that can eliminate the current drawn between the voltage sensing contacts. I-V measurements were performed with low-frequency range (1.34-13.4 Hz) to minimize capacitive and inductive coupling. In order to perform gating experiments, we employed two distinct gates to perform the experiments: the back-gate, V_{bg}, is operated by applying voltage through $SrTiO_3$ substrate (0.5 mm thick); while the side-gate, V_{sg}, is operated by applying voltage to the conducting nanowire electrode written by c-AFM at the $LaAlO_3/SrTiO_3$ interface and placed about 800 nm away from the active nano-constriction. Such side-gate design enabled us to confine the gating effects predominantly on the nano-constriction device, and eliminate the charge leakage to the device from the side gate with leakage currents always below one pA. We note that the side gate offered less hysteresis effects in voltage sweeps and showed better performance when compared to the back-gate tuning.

4.4.3 Device tunability

The device schematic with an electrical measurement configuration is shown in Figure 4-9. Experiments were performed in a four-terminal geometry where the current is passed through source-drain nanowire leads, and four terminal voltage drop (V_{4t}) is measured across the active device nano-constriction, and a side gate is employed to tune the device. Since our measurements were performed in four-terminal geometry, the contact resistance issues have been eliminated in our experimental results. Though, due to the specific shapes we used to design the electrodes, a small geometrical correction to the conductance values might be expected. To verify this, we have designed devices with different geometry configurations (Figure 4-9A), and the qualitative quantization behavior is unaffected in these devices. In fact the characteristic of conductance quantization is that it is expected to be independent of device length and geometry provided by

long coherence lengths. In order to perform bias spectroscopy experiments with side-gates, the operating range of V_{sg} is determined from the I_{sd} vs. V_{sg} test. Figure 4-9B shows the obtained I_{sd} response with the V_{sg} measured at 100 mK for device A. For large negative V_{sg} values, the device can be pinched off with the I_{sd} through constriction approaching zero, and *I-V* characteristics in this range show an insulating behavior for the device as shown in Figure 4-9C. The sharp response of I_{sd} with a small sidegate range is a strong signature for the formation of nanoconstriction in our devices. As the V_{sg} increased towards positive values, for certain voltages, the current began to flow through the device, and eventually showed a conducting behavior for large positive V_{sg} values. As shown in Figure 4-9c-f, the device transforms from an insulating to a conducting state with intermediate tunneling characteristics, possibly arising when the transport is mediated by the barriers. We also note that at T = 100 mK, and for large positive V_{sg}, devices also show a weak superconducting state with a finite nonzero resistance, evident as a nonlinear I-V response near the zero bias in Figure 4-9e, f. From this test, we defined the operating range for V_{sg} as -40 to +70 mV for device A.

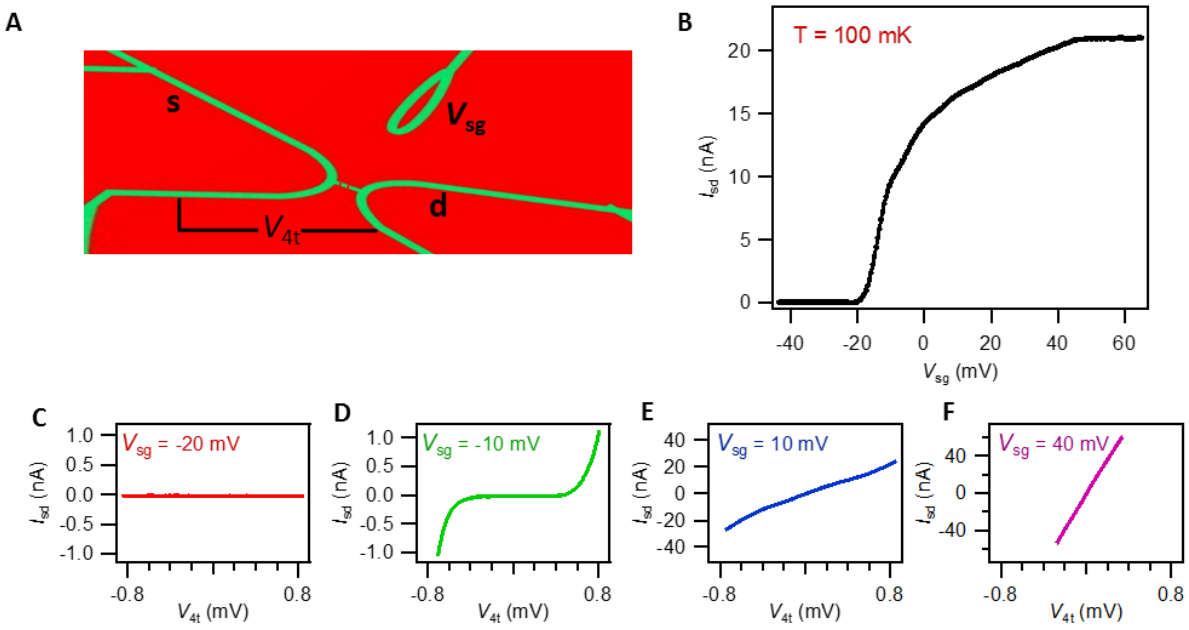

Figure 4-9 Device tunability and current-voltage characteristics. (a) Device schematic with electrical measurement configuration. The green segments are replicas to conducting paths at the $LaAlO_3/SrTiO_3$ interface. Current is applied through source and drain (I_{sd}), while V_{4t} is the four terminal voltage measured across active nano-constriction and V_{sg} is the side gate used to tune the device. (b) Variation in I_{sd} with applied V_{sg} measured at 100 mK for device A. (c-f) Current-Voltage (I-V) curves measured at various V_{sg} showing device tunability across insulating, tunneling, and conducting regions.

4.4.4 Quantized conductance plateaus

Voltage bias spectroscopy experiments on device A (L = 80 nm, L_b = 5 nm and L_q = 10 nm) are performed and presented in Figure 4-10b-d. The operating range of V_{sg} for the device is determined from the I_{sd} vs. V_{sg} test at -40 to +70 mV, for which the device can be tuned from an insulating to a conducting state (supplementary materials). Figure 4-10b, c shows the waterfall plots of the obtained differential conductance G versus a four-terminal voltage (V_{4t}) by varying V_{sg}, at B = 0 T and 9 T, respectively. At B = 0 T, especially at near zero bias ($V_{4t} \sim 0$ V), the traces

appear to converge to specific G values that are close to two, four and six e^2/h, whereas the traces converge to the G value of one, two and three e^2/h at B = 9 T. Moreover, we also notice that G appears to converge to specific values even for finite biases. To understand the plateau evolution better, the zero bias G as a function of V_{sg} and B is measured and plotted in Figure 4-10d. Here the first plateau-like feature in G appears slightly below the value of two e^2/h, and seems to have an overall plateau sequence of two, four, and six e^2/h at B = 0 T, albeit with a transmission (t) less than unity. Upon increasing the B to 9 T, the conductance plateaus are well quantized to one, two, three and four e^2/h and further appear to be splitting from the spin-degenerate plateaus two and four e^2/h, an indication for the lifting of spin-degeneracy in presence of B. The precise plateau behavior with G quantized to integer multiples of e^2/h ($G = Ne^2/h = NG_0$, N-even for spin-degenerate, even/odd for spin-resolved) observed at 9 T is a signature of conductance quantization in these devices. The observed conductance quantization at B = 0 T with $t < 1$ may have resulted from various possibilities including a reduced transmission (t <1) arising due to the resistive barriers, back scattering in the nanowires related to disorder and impurity, or an anomalous behavior that arises from spin mixing similar to one reported in semiconductor QPC devices[74]. Overall, the bias spectroscopy results shown here strongly suggest that these devices exhibit a 1D character, and resemble quantum point contacts (QPCs). It is quite challenging to observe quantized conductance as it requires a very clean system, without electronic disorder between leads that are far apart. The observed quantization behavior in our $LaAlO_3/SrTiO_3$ devices emphasizes the capability of creating high quality and clean devices with this c-AFM technique at nanoscales.

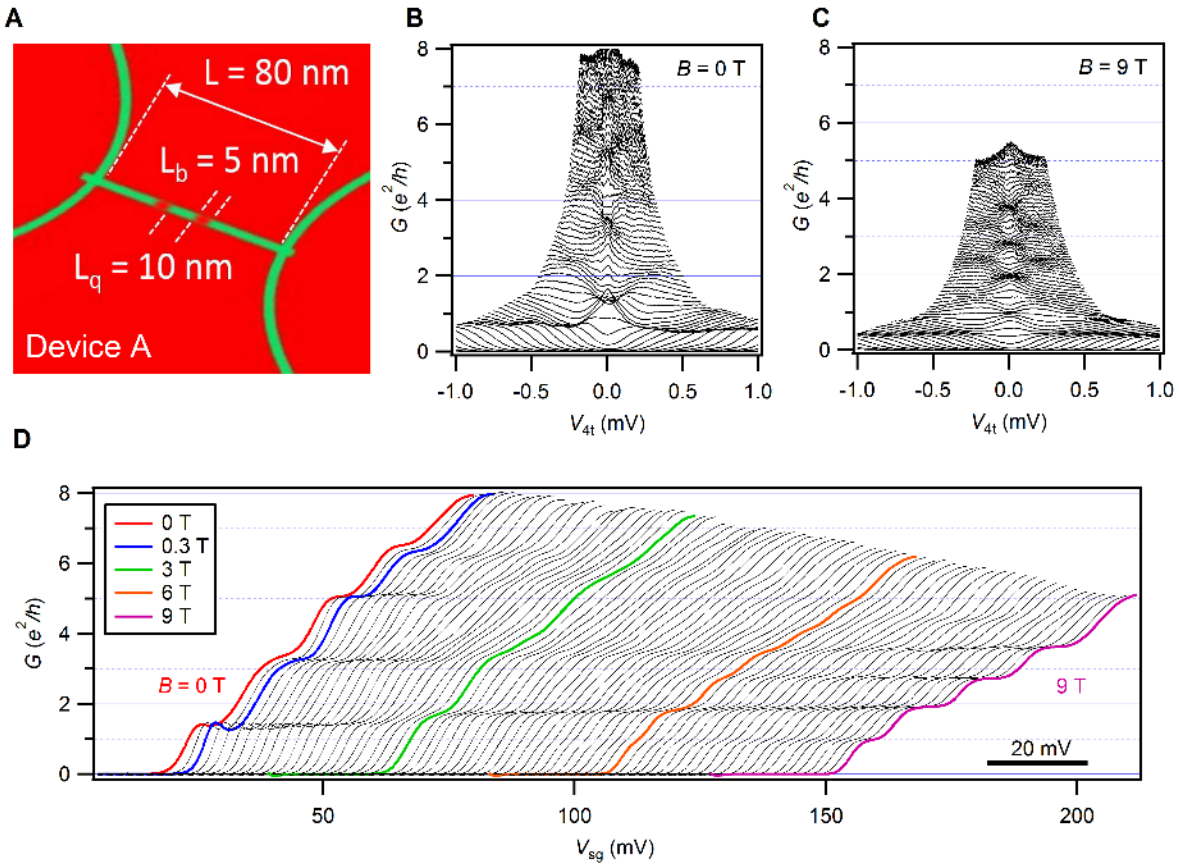

Figure 4-10 Device configuration and bias spectroscopy. (a), Schematic of the device written by c-AFM. Green lines are nanowires created on the interface by "writing" with positive AFM tip voltage on the sample surface, and the QPC nanoconstriction is written on the 80 nm long nanowire between two curved nanowires. (b and c), Differential conductance G versus voltage drop measured (V_{4t}) with different side-gates (V_{sg}) at B = 0 T, and an out of plane magnetic field B = 9 T, respectively. (d) Differential conductance G measured near zero bias as a function of V_{sg} with B varied from 0 to 9 T in steps of 0.3 T (for better representation, here each curve is shifted by 3 mV towards a positive V_{sg}). At B = 0 T, the device shows plateaus near 2, 4, and 6 e^2/h, While at B = 9 T, the device shows plateaus at 1, 2, 3 and 4 e^2/h precisely.

Of the conductance quantization behavior reproduced in numerous devices on different samples, all show signatures of quantization, but with differences in their evolution with a magnetic field. The results for various devices are summarized in Figure 4-11a-c. The most

contrasting quantization behavior is observed at B = 0 T. For device B, the plateaus are at 2, 6, 8 and 13 e^2/h approximately, where in the case of device C, they are at 4 and 8 e^2/h. This could be related to a superconductivity conductance plateau since the devices are in a superconducting state at B = 0 T (supplementary material). Devices A-C show well-quantized conductance plateaus at 1, 2 and 3 e^2/h at B = 9 T. To obtain more insight into such unconventional evolution of quantization with a magnetic field, we further extracted trans-conductance (dG/dV_{sg}) with respect to B. This is shown in Figure 2D for device A and the dG/dV_{sg} is represented in color scale, where each low/constant dG/dV_{sg} region corresponds to the plateau region in usual conductance plots and the high dG/dV_{sg} regions correspond to the transition between these plateaus. In a 1D sub-band energy picture, the high dG/dV_{sg} corresponds to a crossing of sub-band levels, where the Fermi level of the system falls in density of states (DOS) of the sub-band and the low/constant dG/dV_{sg} corresponds to Fermi level above DOS, but within a sub-band. In Figure 4-11d, the splitting of high dG/dV_{sg} regions is clearly evidence that it corresponds to the evolution of 1 and 3 e^2/h plateaus from the 2 and 4 e^2/h plateaus, validating the sub-band level splitting in presence of B as a consequence of lifting the spin-degeneracy. Interestingly, the splitting in high dG/dV_{sg} regions happen to take place at a certain B. In order to determine the critical B, we analyzed splitting strength in V_{sg} with B and plotted this in Figure 2E for the 1st and 2nd splitting. The splitting strength varies in a linear fashion with B and critical B for the splitting extracted by extrapolating the linear fit; these are about 1.2 T, 1.8 T for the 1st and 2nd splitting, respectively. We note that the superconducting critical field is around 0.3 T for the $LaAlO_3/SrTiO_3$ system, which is much smaller than the observed critical field values for the splitting. We assign these critical fields as the fields required to break the electron pairing. Above the critical field, the splitting resulted in evolution of spin-resolved plateaus with a magnetic field; its origin can be explained by

considering the Zeeman splitting of 1D sub-band energy levels. The induced Zeeman energy E_z in presence of the B is given by $E_Z = g\mu_B B$ which depends on the Landau g-factor, in this case equal to 0.52, as we estimated.

Furthermore, the strength of Zeeman splitting associated with a Landau g-factor can lead to non-linear correlations among the sub-bands and electronic states. Such an example is observed for device D and is shown in Figure 4-11f-g. This particular device shows a clear quantization at 1 and 3 e^2/h with a 2 e^2/h plateau missing at B = 9 T. The continuous plateau evolution with B is clearer in the trans-conductance plot shown in Figure 4-11g. The first two high dG/dV_{sg} regions at B = 0 T (corresponds to spin-degenerate states with G = 2 and 4 e^2/h) split when B > 2 T into spin-resolved states, i.e. 1↑, 1↓ and 2↑, 2↓ (1, 2, 3 and 4 e^2/h conductance respectively). The 1↓ and 2↑ states appear to recombine at B > 7 T leading to a plateau formation at 3 e^2/h with the absence of the 2 e^2/h plateau. A similar type of electron state recombination was recently observed in electron pairing without the superconductivity scenario in a $LaAlO_3/SrTiO_3$ system[69].

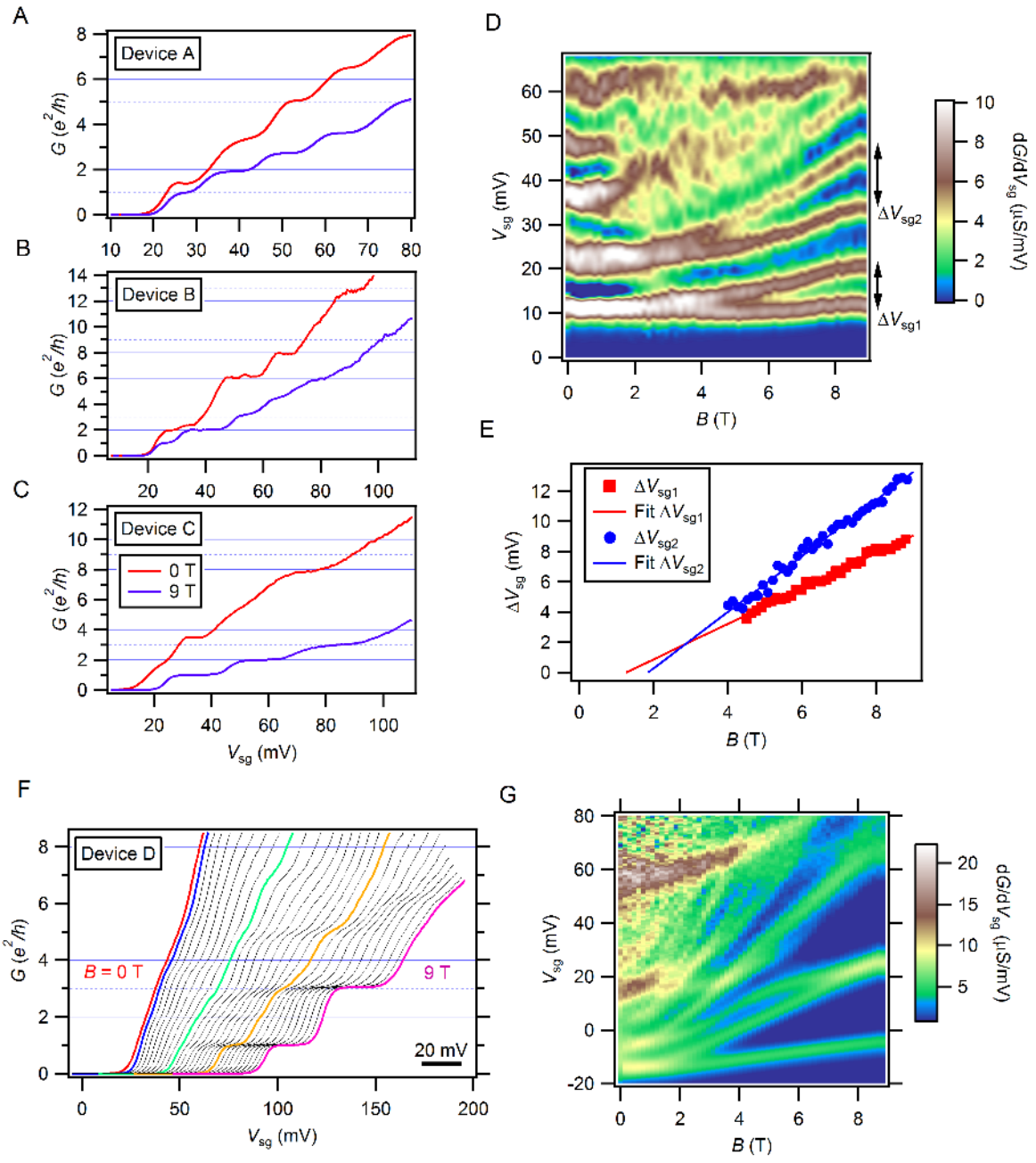

Figure 4-11 Evolution of conductance quantization. (a-c), Differential conductance G variation with V_{sg} at 0 and 9 T for devices A, B and C. (d), Color plot for extracted trans-conductance dG/dV_{sg} with V_{sg} and B, showing a clear splitting of plateaus 1 e^2/h from 2 e^2/h and 3 e^2/h from 4 e^2/h at a critical value of B. (e) Plots of ΔV_{sg} vs B for the device, the intercept gives the critical magnetic field at 1.3 T and 1.8 T, for first and second energy levels, respectively. (f) Differential conductance G measured near zero bias as a function of V_{sg} with B varied from 0 to 9 T in step of 0.3 T for device D. (g) Color plot for extracted trans-conductance dG/dV_{sg} with V_{sg} and B for device D.

Generally, for a strict 1D confinement, apart from the Zeeman splitting, the quantization is expected to be insensitive to *B*. However, in some of our devices, we have noticed that for a given V_{sg}, the sub-band level occupancy depends on the strength of the perpendicular *B* where the quantized levels are depopulated with an increase in *B*, suggesting that the perpendicular *B* coupled to the cyclotron motion of the electrons provides additional energy along with QPC confinement. Consequently, at a certain magnetic field strength (magnetic length smaller than device width), due to the cyclotron motion of electrons, the transport supposedly enters into a quantum Hall regime with a Landau level filling in the quasi-1D limit from the 1D transport. In order to verify this, a series of resistance (*R*) versus *B* curves obtained at various V_{sg}, and with background subtracted resistance ΔR with *B* at different V_{sg} is shown in Figure 4-12a. The variation in ΔR with *B* shows oscillatory behavior with each minima corresponding to a transition from *N* to *N*+1 quantized resistance plateaus, which can be interpreted as similar to the case of SdH oscillations in a quasi-1D case. The pattern shows more oscillations with increasing V_{sg}, obvious from the line cut profiles obtained at V_{sg} = 30, 50 and 70 mV as shown the bottom panels of Figure 4-12a . This effect is regarded as a depopulation of magnetic sub-bands in the presence of a perpendicular magnetic field in a quasi-1D limit, which also observed in semiconducting systems[75]. This can be explained by adding an additional term of magnetic energy ($\hbar\omega_c$) that arises from the cyclotron motion of the electron in a perpendicular magnetic field due to the dispersion of the waves. The resultant conductance can be given by an expression[75]:

$$G(B) = \frac{e^2}{h} N \qquad \text{with } N = \text{int}\left[\frac{E_f - eV_0}{\hbar\omega} + \frac{1}{2}\right],\ \omega = \sqrt{\omega_0^2 + \omega_c^2} \text{ and } \omega_c = \frac{eB}{m^*}$$

Here 'int' denotes the truncation to integer, ω is the resultant frequency, $\hbar\omega_0$ is the level separation energy, $\hbar\omega_c$ is the effective cyclotron energy due to the magnetic field, E_f is the Fermi level, V_0 is the chemical potential raised in QPC and m^* is the effective mass. Assuming the spin degeneracy is lifted, this equation suggests that the quantization will be preserved, but with a larger variation of V_{sg} to populate a new sub-band. With a large B and a shallow QPC confinement ($\omega_c >> \omega_0$), N is proportional to $1/B$ which is exactly the SdH effect. However when ω_0 is comparable to ω_c, N will not be proportional to $1/B$, and several similar behaviors have been reported. In order to verify this, Landau plots are shown in Figure 4-12b-d where a Landau index n (also corresponding to plateau numbers $N = R/R_0$ where $R_0 = h/e^2$) is assigned to each minimum and n is plotted against the $1/B$ at a minimum in ΔR. The red solid line interpolates between extracted minimum positions fitted to the data according to the model of Berggren *et al.*[76]. The fact that the variation in index filling with 1/B deviates from linearity, as is expected for a confined 2D case, strongly suggests that the lateral confinement is more 1D in nature.

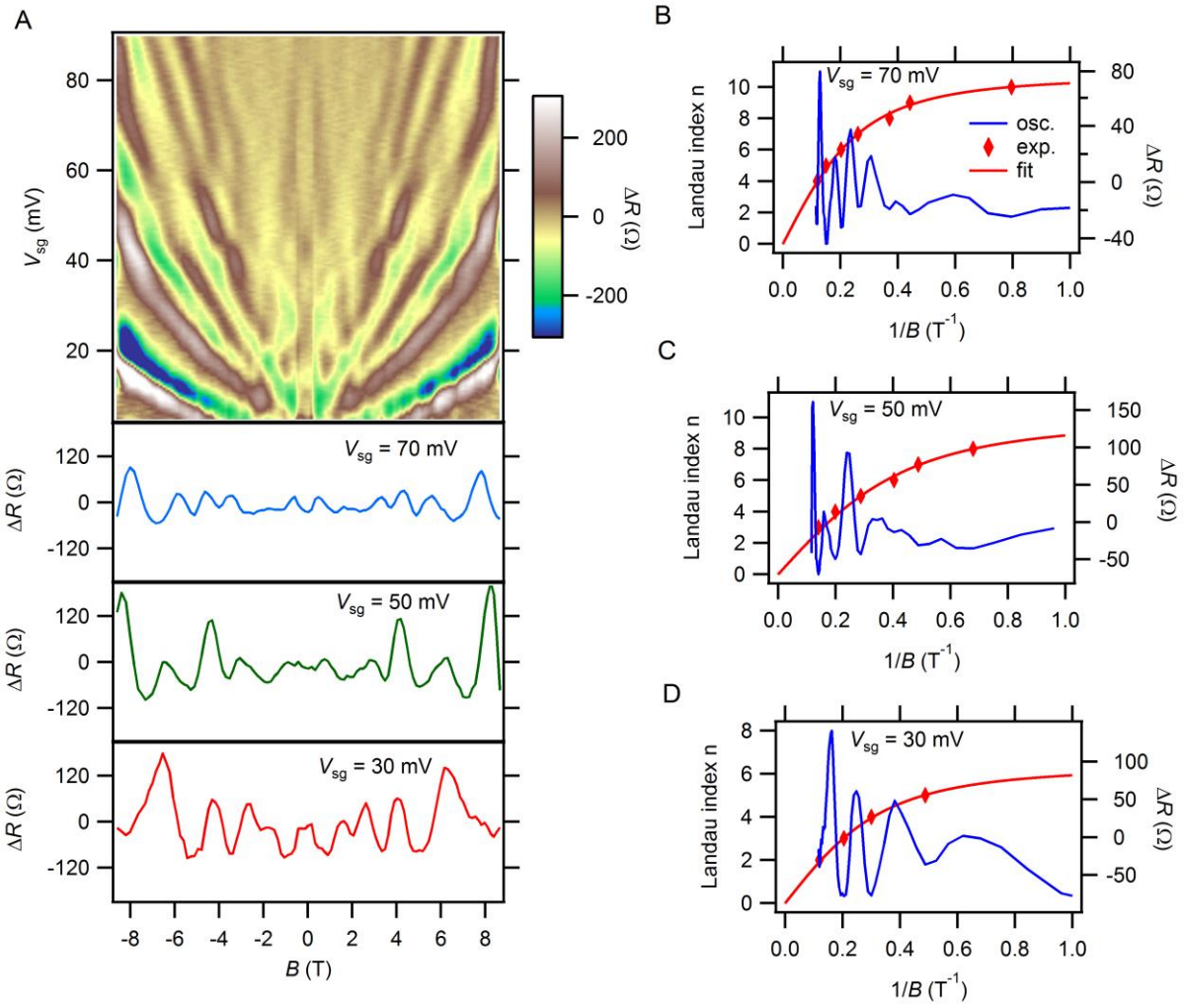

Figure 4-12 Quantum oscillations in magneto-resistance and a Landau fan-diagram analysis. (a), Color plot for the extracted Δ*R* with V_{sg} and *B*. The line cut of Δ*R* with *B* taken at a fixed V_{sg} = 30, 50 and 70 mV, respectively, showing a clear oscillatory behavior with extrema. The resistance minima here corresponds to the quantized resistance plateaus appearing in *R* vs. *B*. (b-d), Landau level index *n* and the corresponding Δ*R* variation with 1/*B* plots analyzed at V_{sg} = 30, 50 and 70 mV, respectively. The variation in *n* with 1/*B* is nonlinear, suggesting a 1D character for sub-bands.

Having established the 1D character with a well resolved sub-band structure, it is natural to inquire how ballistic the transport is. The characteristic of an ideal ballistic device is its length independent of electron transport. To estimate how far these 1D electron modes travel without

scattering can be done by preserving the quantization, that is, the mean free path length. We have constructed devices with various length scales. Figure 4-13a,b shows the G and dG/dV_{sg} as a function of V_{sg} at various B for a device of length 600 nm, consisting of two 10 nm barriers spaced by 20 nm, respectively. Significantly, the plateaus appear at $B = 9$ T with conductance quantization at 1, 2, 3 e^2/h suggesting a long free mean path in these devices. The mean free path l_{mfp} can be estimated by:

$$l_{mfp} = v_F \cdot \tau = \frac{\hbar k}{e^2 n \rho} \approx \frac{\hbar k}{e^2 n_s R w / l},$$

Here k is the Fermi wave vector, w is the width of the constriction, l is the device length and n_s is the two-dimensional carrier density. The resistance, R, is estimated by extracting the deviation from the ideal quantization of the $2e^2/h$ plateau which is about 300 Ω. The above formula with $w \sim 10$ nm, $l = 600$ nm and $n_s \sim 10^{13}$ cm^{-2} (from Hall measurements) yields l_{mfp} at about 100 μm, indicating that the transport in the channel is indeed ballistic.

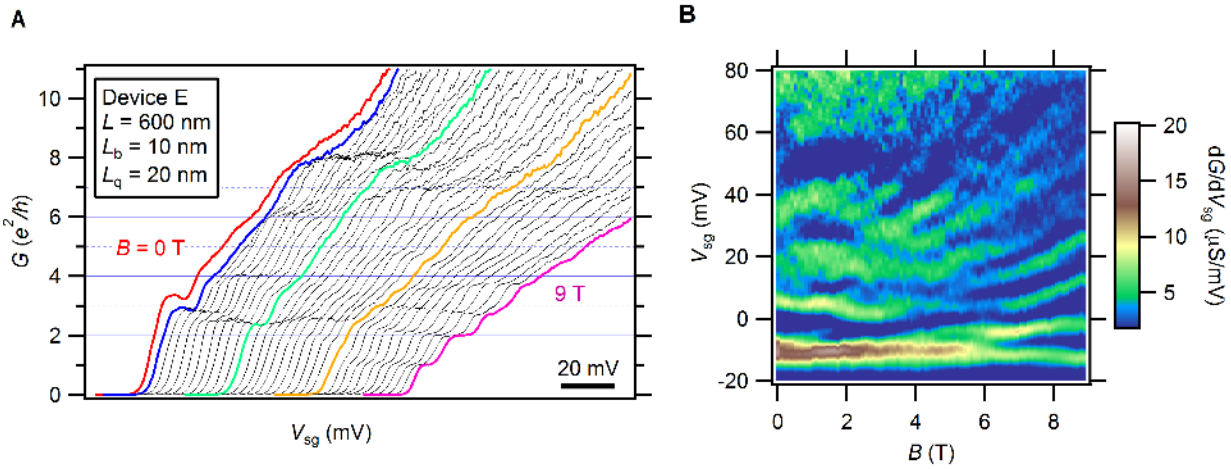

Figure 4-13 Conductance quantization in long channel device. (a), Differential conductance G measured near zero bias as a function of V_{sg} with B varied from 0 to 9 T in step of 0.3 T for 600 nm long channel in device E. (b), Color plot for extracted trans-conductance dG/dV_{sg} with V_{sg} and B for device E.

Although the quantization behavior with a 1D character has been seen in various metallic and semiconducting systems, the $LaAlO_3/SrTiO_3$ interface system with a 1D character presented here presents an exciting case with intrinsic properties such as superconductivity, magnetism and spin-orbit coupling. In fact, a peculiar conductance behavior in superconducting state (B = 0 T) and low magnetic fields could be the consequence of such combined effects. Generally, in a spin-degenerate case, the quantization for an electron is expected to follow 2, 4, 6 and 8 e^2/h. For device B the zero bias conductance plateau near B = 0 T is quite interesting since the plateau is quantized at about 2, 6, 8, 13 e^2/h, while the 4 and 10 e^2/h plateaus are missing. It is compelling to relate this to a coexistence of electrons in pairs along with individual electron states. In this pairing scenario, the conductance expected to be 4, 8, 12 and 16 e^2/h for electron pairs by considering the charge as $2e$ for a pair. Considering a Fermionic single electron and an electron pair as two non-interacting channels would explain the overall conductance of the device B with the missing 4 e^2/h plateau. As device C only shows 4 and 8 e^2/h at a zero field, which may indicate there are only electron pairs rather than single electrons in the system. The plateau evolutions for device D as described in Figure 4-11 also confirm that there is some mechanism driving electrons to pair together in $LaAlO_3/SrTiO_3$ system. Though similar confined nanostructures show different types of conductance plateau behaviors, they all fall into the four types described before, and the underlying physics need further investigation. Another aspect is that conductance plateaus with spin-degeneracy persist in elevated magnetic fields, and a sufficient magnetic field is needed to break this spin-degeneracy. The possible source of energy could be the strong spin-orbit coupling at the interfaces in $LaAlO_3/SrTiO_3$ systems, which require a significant magnetic field to break the degeneracy. Although, the small g-factor in our system[77-79] (<1) leading to a very small Zeeman

energy and making it less possible to resolve the splitting for low magnetic fields cannot be ruled out.

It is very significant to observe conductance quantization in the 600 nm channel device with well resolved quantized conductance at 9 T leading to a mean free path length as long as 100 μm. The typical mean free path length in 2D $LaAlO_3/SrTiO_3$ systems is only around 100 nm[80]; such a long coherence with spin-resolved transports observed in our nanowire devices strongly suggest evidence for chiral-edge states, and ballistic transport. The SdH-like oscillations as a function of the magnetic field as shown in Figure 4-12 support the chiral-edge channels in the quantum Hall region. Furthermore, these SdH-like oscillations are directly associated with the conductance plateaus as the oscillation minima coincide with the position of quantized resistance. This also suggests that the origin of the quantum Hall effect is related to zero-field quantization, and that the evolution of the quantum Hall effect can reduce the backscattering and explains the increasingly precise conductance quantization with increasing magnetic field and limited accuracy of the conductance quantization in zero field. Our results will stimulate research to investigate exotic phases of condense matter. Recent theoretical work suggests that the interplay of various electronic phases in reduced dimensions will give rise to predictions like helical wires and Majorana fermions. Particularly for the Majorana condition, the three, i.e. superconductivity, magnetism, spin-orbit coupling, of the necessary four ingredients are naturally inherent in the $LaAlO_3/SrTiO_3$ system. The fourth ingredient is to confine electrons in a 1D wire which is ballistic.

In summary, here we find ballistic transport through 1D nanowires with QPCs embedded on a $LaAlO_3/SrTiO_3$ interface. Furthermore, certain missing conductance plateaus at zero field and anomalous conductance plateaus at finite field due to electron pairing, suggest that the novel physics in this system need further investment.

4.5 CONCLUSION AND DISCUSSION

Two kinds of confined nanostructures created at $LaAlO_3/SrTiO_3$ interfaces show quite different phenomena. One has longer separation between ‘cuts’ and deeper barriers and behaves like a quantum dot which shows Coulomb diamond at a low gate bias regime. Remarkably, these diamonds do not split until magnetic field reach a splitting critical field B_p, one order higher than the superconducting critical field. This proves that electrons can pair without superconductivity. In the same structure at a higher gate bias regime, it shows Fabry-perot interference, in which electrons travel in a ballistic manner in the channel until they hit the barriers and are reflected. Then those forward and backward electrons form interference pattern. Another nanostructure with shorter separation and shallow barriers behaves like a quantum point contact and shows perfect conductance plateaus in transport measurements. Similar to QD, those conductance plateaus do not split until the magnetic field reaches a splitting critical field ~ 2 T. This again proves that electrons pair without superconductivity. Further magnetic population results reveal the 1D and 2D crossover of the channel meaning that the channel can be tuned into a 1D or a 2D transport. In conclusion, engineering the nanowire at $LaAlO_3/SrTiO_3$ interfaces with barriers, not only reveals electron pairing and the 1D ballistic transport nature of this system, but also provides a great platform for physics research such as finding Majorana fermions, and studying electron pairing mechanisms with and without superconductivity.

5.0 SDH OSCILLATIONS IN HIGH MOBILITY $AL_2O_3/SRTIO_3$ STRUCTURES

5.1 INTRODUCTION

As discussed in previous chapters, it is well established that a two-dimensional electron liquid (2DEL) can form at the interface of epitaxial grown semiconductor heterostructures, and by using c-AFM technique, nanostructures can be written at this interface[36] providing flexibility in making desired devices. The 2DEL at $Al_2O_3/SrTiO_3$ ($Al_2O_3/SrTiO_3$)[81-83] is nominally similar to those in semiconductor heterostructures, but supports additional phases, such as superconductivity and magnetism, which are not observed in a 2D electron system. Here we report that by using the same writing technique as used on $LaAlO_3/SrTiO_3$, i.e. c-AFM, we can also write nano structures on an amorphous $Al_2O_3/SrTiO_3$ interface with quite high electron mobility.

I was the sole person who collected the data and analyzed the results for this project.

5.2 DEVICE PREPARATION

5.2.1 Sample Growth and Processing

$Al_2O_3/SrTiO_3$ heterostructures are grown in a similar fashion to that of Lee *et al*.[81] by Sang Woo Lee's group in Harvard University. Electrical contacts are made to the $Al_2O_3/SrTiO_3$ interface by Ar+ etching (25 nm) followed by Ti/Au (2 nm/23 nm) sputter deposition. A second Au layer defines wire bonding pads and their leads, connecting them to the contacts from the first Au layer

for each “canvas”. Electrical contact is made between this second layer, and a chip carrier via gold wire bonds.

5.2.2 Device Writing

Nanoscale devices are written using c-AFM lithography. Before device writing, the entire canvas is erased by performing a tip voltage, V_{tip} = -10 V, in contact mode. The background resistance between adjacent electrodes (>0.5 GΩ at room temperature) increases by several orders of magnitude at low temperatures, eliminating the possibility of unwanted coupling between electrodes.

The resulting nanostructures are composed of rectangular bars with a width of ~10 nm and ~500 nm, as determined by analysis of local erasure experiments performed on the same canvas with the same AFM probe. Trapezoidal virtual electrodes contact the gold interface electrodes at one end, and taper down to contact the nanostructure at the other end, (Figure 5-1a). Upon completion of device-writing, the sample is transferred in the dark to the vacuum environment of a dilution refrigerator for cryogenic measurements within 5 minutes.

5.3 EXPERIMENTS

Transport experiments are carried out in Quantum Design dilution fridge with a 50 mK base temperature and a 9 T magnet. Simultaneous sampling 24-bit data acquisition cards are used to source voltage and acquire amplified voltage signals which come from true differential voltage amplifiers (Femto model DLPVA) with a one TΩ input impedance that can eliminate currents

drawn between the voltage sensing contacts. Low-frequency (~1 Hz) lock-in measurements are performed to minimize capacitive and inductive coupling. Back-gate tuning is achieved by applying voltage directly to the contact layer underneath the sample.

Four-terminal conductance is acquired by sourcing current I_{14} from lead 1 to 4 and simultaneously measuring the voltage V_{23} between leads 2 and 3 which is separated from the main current channel by 3 μm. The Hall mobility measurement is acquired by sourcing the current I_{14} from lead 1 to 4 and simultaneously measuring the Hall voltage V between leads 2 and 6, which is perpendicular to the main current channel.

5.4 RESULTS

Transport experiments are performed on wide Hall bar structures with 500 nm width and 3μm length, and on thin Hall bar structures with 10nm width and 3μm length. The wider hall bar structures are written multiple times with small amount offsets (~10 nm) in both vertical and horizontal directions. All of the results reported here have been reproduced qualitatively in multiple devices from the same $Al_2O_3/SrTiO_3$ sample.

Similar to our previous experiments on the $LaAlO_3/SrTiO_3$ system, the nanostructure can also be written at the $Al_2O_3/SrTiO_3$ interface. Figure 5-1b shows the Magnetic force microscopy (MFM)[84] image of the device immediately after completion of the writing. The transport measurements then were taken by measuring the channel resistance R_{xx} and the Hall resistance R_{xy}.

The 2D nature of the conduction in wide Hall bar structure is indicated by Shubnikov-de Haas (SdH) quantum oscillations which are superimposed on a large background of positive magnetoresistance R_{xx} (Figure 5-1c). The Hall resistance R_{xy} also shows oscillations but they are not obvious as in R_{xx} (Figure 5-1d). By taking the derivative of the channel resistance and the Hall resistance, the oscillation become more obvious, and there appears a correlation between oscillations of R_{xx} and R_{xy}.

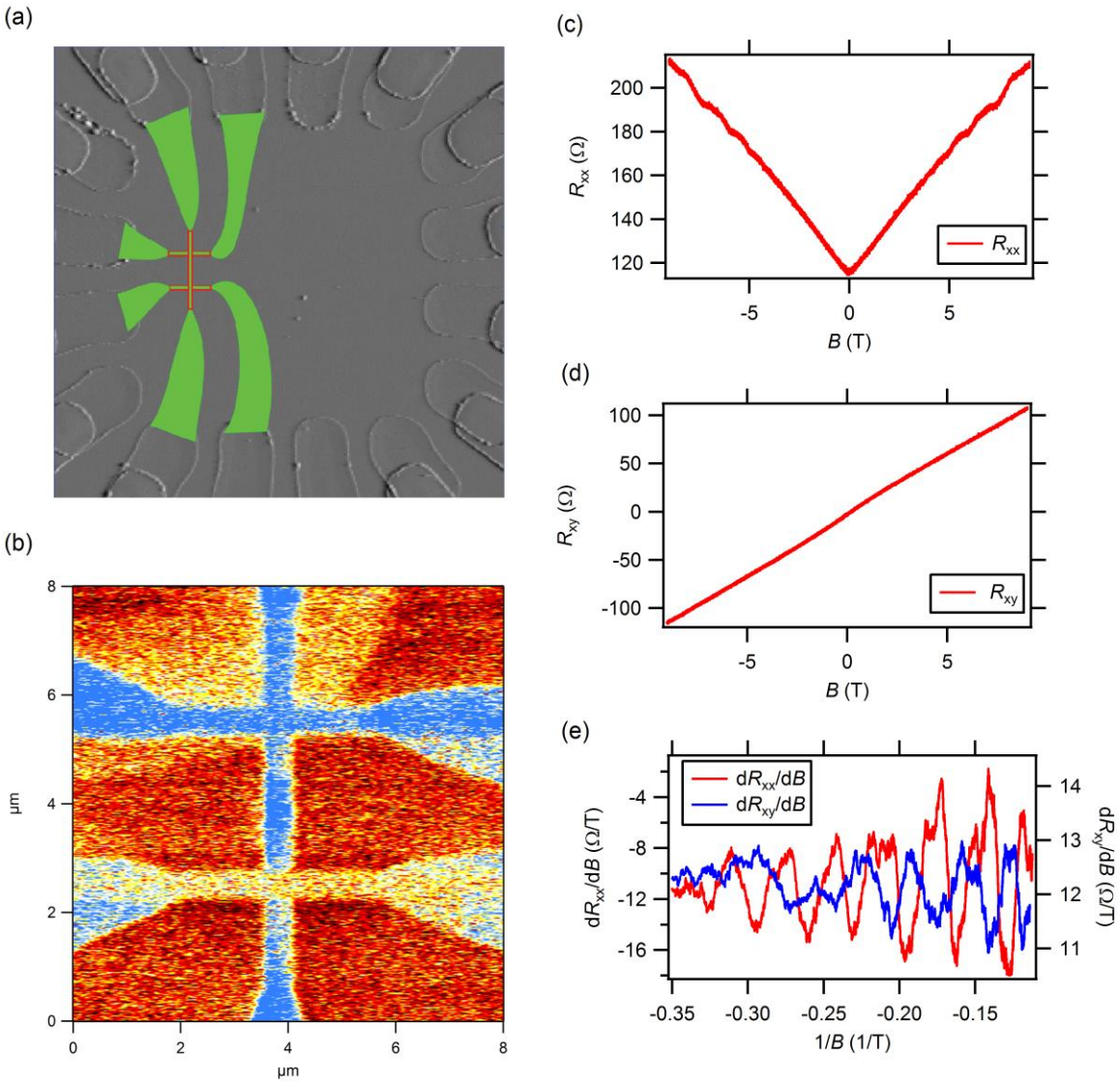

Figure 5-1 Device geometry and transport properties. (a), Device geometry. (b), MFM image of the device. (c), R_{xx} vs B. (d), R_{xy} vs B at V_{bg} = 0 V. (e), dR_{xx}/dB at dR_{xy}/dB shows that the oscillations are correlated.

By taking channel resistance with fields at different temperatures, and then subtracting the magneto-resistance background, the SdH oscillations become more obvious, and these oscillations show temperature dependence (Figure 5-2a). According to theory[85], the oscillation amplitude ΔR_{xx} can be described as:

$$\Delta R_{xx} = 4R_0 e^{-\alpha T_D} \alpha T / \sinh(\alpha T)$$

Where $\alpha = 2\pi^2 k_B/\hbar\omega_c$, $\omega_c = eB/m^*$ is the cyclotron frequency, e is the electron charge, m^* is the carrier effective mass, k_B is Boltzmann's constant and $\hbar$ is Planck's constant divided by 2π, R_0 is the channel resistance in zero field, $T_D = \hbar/2\pi k_B\tau$ is the Dingle temperature, and τ is the total scattering time. At a certain magnetic field, m^* can be deduced by fitting the temperature-dependent oscillation amplitude with $\Delta R_{xx}(T)/\Delta R_{xx}(T_0) = Tsinh(\alpha T_0)/T_0\sinh(\alpha T)$, where $T_0 = 50$ mK. At the largest peak position at 8.2 T, the fit leads to an effective mass of 1.32 m_e, where m_e is the free electron mass, consistent with reports of other $SrTiO_3$-based heterostructures. At a fixed temperature, T_D or τ can be extracted from the slope of the Dingle plot, which is $\ln[\Delta R_{xx}\sinh(\alpha T)/4R_0\alpha T]$ versus 1/B (Figure 5-2c, for T = 50 mK), which gives $\tau = 1.93 \times 10^{-12}$s or $T_D = 0.63$ K, corresponding to a quantum mobility $\mu_{SdH} = \frac{e\tau}{m^*} = 2.5 \times 10^3 \mathrm{cm^2V^{-1}s^{-1}}$.

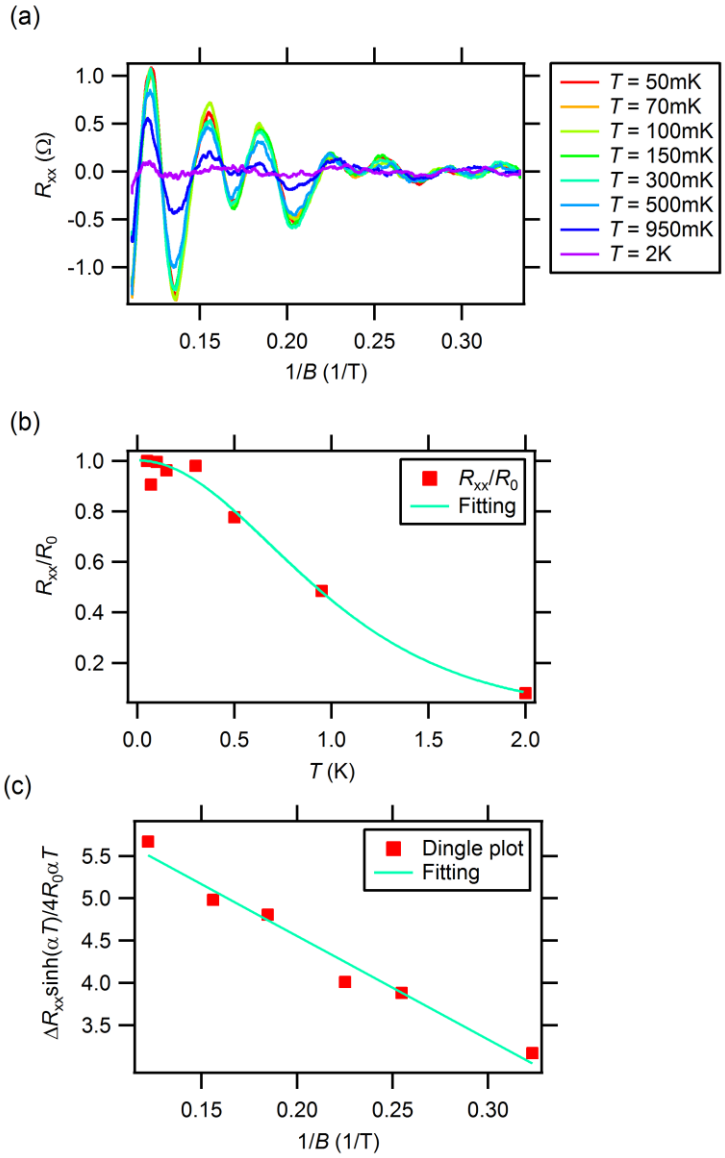

Figure 5-2 SdH oscillations analysis. (a), ΔR_{xx} vs $1/B$ at temperature range of 50 mK to 2 K. (b), R_{xx} peak at B = 8.2 T amplitude and theory fit. (c), Dingle plot and fit for the B = 8.2 T peak.

Figure 5-3a shows the ΔR_{xx} vs. $1/B$ at different back-gates, and surprisingly the Fourier transformation results show same peak positions for different back-gates, which means that the carriers that support the SdH oscillation have the same carrier density at different back-gates. As for the SdH oscillation theory, carrier density is $n = \frac{2 \cdot e}{\Delta(1/B) \cdot h}$ where two comes from spin-

degeneracy, e is electron charge, and h is Planck constant, which gives us $n = 1.33\times10^{12}$ cm^{-2}. By fitting the R_{xy} vs. B in Figure 5-1d and extracting R_{xx} from Figure 5-1c, the extracted Hall carrier densities are 5.0×10^{13} cm^{-2} and 6.5×10^{3} cm^2/V·s, respectively. When these two numbers are compared to the ones from SdH results fitting, the mobility from both methods are in the same order, however the Hall carrier density is 30 times larger than the carrier density calculated from the SdH oscillation. Even if we consider the six-fold degeneracy and if we assume a valley degeneracy of three and spin degeneracy of two, Hall carrier density and SdH carrier density still do not match, which may indicate that not all carriers shown in Hall measurements participate in SdH oscillations as it requires quite high mobility to support SdH oscillation. SdH measurements in 2DEL system from other experiments also shown this kind of disagreement between the Hall carrier density and the SdH carrier density.

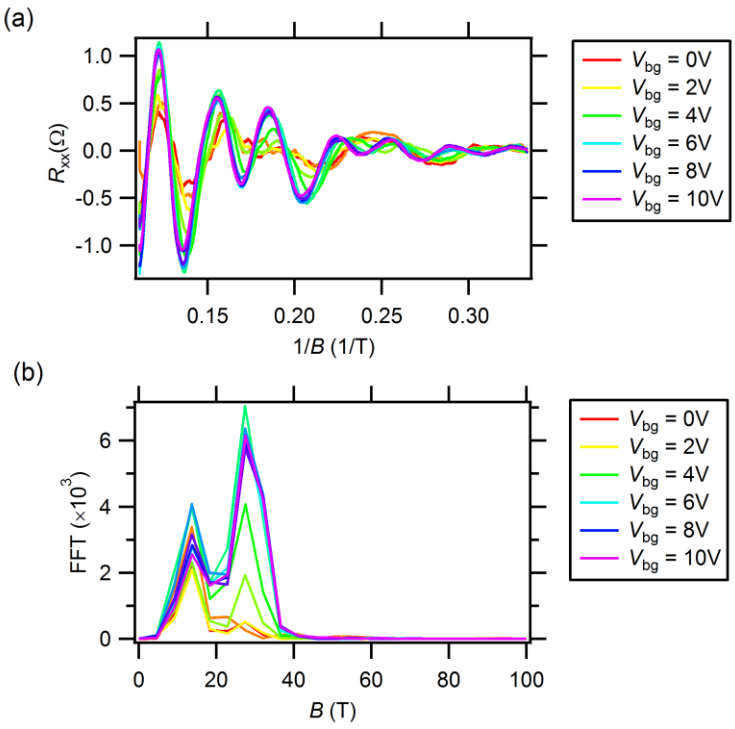

Figure 5-3 SdH oscillations at different back-gates. (a), R_{xx} vs $1/B$ at backgate range of 0 V to 10 V, the back-gate will shift the peak slightly, and change the peak amplitude. (b), Fourier transformation of the R_{xx} oscillations show the same peak position for different back-gates.

5.5 CONCLUSION AND DISCUSSION

As Al_2O_3 deposited by the atomic layer deposition is amorphous, the polar discontinuity-induced electronic reconstruction as expected in the crystalline $LaAlO_3/SrTiO_3$ interface is not applicable here. The metal-insulation transition may be explained by a model in which oxygen diffuses out from the $SrTiO_3$ surface, and introduces 2D electron gas at the interface. The high quantum mobility observed for the 2DEL at amorphous $Al_2O_3/SrTiO_3$ interfaces is comparable to the 2DEL at spinel/perovskite $\gamma - Al_2O_3/SrTiO_3$ oxide interfaces which provides a more

convenient and/or industry-friendly manner in which to grow ALO. This substance may also arise as a new material system for future spin-based devices.

6.0 SUMMARY AND OUTLOOK

Oxide semiconductors, especially $LaAlO_3/SrTiO_3$, show a wide range of emergent properties, such as metal-insulator transition, superconductivity, ferromagnetism, and spin-orbit coupling. Many high-performance novel devices are demonstrated in this platform.

In this thesis, we used AFM to create nanostructures at $LaAlO_3/SrTiO_3$ interfaces. 1D nanowires can be created, at this interface, which show remarkable anomalous phenomena. The room temperature/low temperature mobility enhancement for 1D nanowires at $LaAlO_3/SrTiO_3$ interfaces holds great promise for introducing this system for practical use. Additionally, the nonlocal transport results indicate that there might be spin transport involvement indicating that this system has great potential for next-generation spin devices. Besides these findings, the finding of nonlocal transport at superconducting states makes this system more complex, but also more attractive for physics researchers.

By engineering the nanowires a little further, two kinds of confined nanostructures can be created at $LaAlO_3/SrTiO_3$ interfaces. One nanostructure with longer separation between 'cuts' and deeper barriers behaves like a quantum dot, and the other, with shorter separation and shallow barriers, behaves like a quantum point contact. These two structures reveal electron pairing without superconductivity. These results and the 1D ballistic transport nature of this system makes $LaAlO_3/SrTiO_3$ a great platform for physics researches for studies such as finding Majorana fermions, studying electron pairing mechanism with and without superconductivity, studying true 1D transport systems, and using clean systems which require ballistic transport.

Finally, we also show that the c-AFM technique can apply to amorphous $Al_2O_3/SrTiO_3$ interfaces to create high mobility nanostructures. The high quantum mobility acquired 2DEL at

amorphous $Al_2O_3/SrTiO_3$ interfaces is comparable to the 2DEL at spinel/perovskite $\gamma - Al_2O_3/SrTiO_3$ oxide interfaces providing a more convenient and/or industry-friendly way to grow ALO. This may also arise as a new material system for future spin-based devices.

BIBLIOGRAPHY

1 Ohtomo, A. & Hwang, H. Y. A high-mobility electron gas at the $LaAlO_3/SrTiO_3$ heterointerface. *Nature* **427**, 423-426, (2004).

2 Chu, Y. Y. *et al.* Distribution of electronic reconstruction at the n-type LaAlO3/SrTiO3 interface revealed by hard x-ray photoemission spectroscopy. *Applied Physics Letters* **99**, (2011).

3 Liao, Y. C., Kopp, T., Richter, C., Rosch, A. & Mannhart, J. Metal-insulator transition of the $LaAlO_3$-$SrTiO_3$ interface electron system. *Physical Review B* **83**, 075402, (2011).

4 Cheng, G. *et al.* Anomalous Transport in Sketched Nanostructures at the $LaAlO_3/SrTiO_3$ Interface. *Physical Review X* **3**, 011021, (2013).

5 Smith, H. M. & Turner, A. F. Vacuum Deposited Thin Films Using a Ruby Laser. *Appl Optics* **4**, 147, (1965).

6 A. Y. Cho, J. R. A. Molecular beam expitaxy. *Progress in Solid State Chemistry* **10**, 157-191, (1975).

7 El Kazzi, M. *et al.* Photoemission (XPS and XPD) study of epitaxial LaAlO3 fiim grown on SrTiO3(001). *Mat Sci Semicon Proc* **9**, 954-958, (2006).

8 Podkaminer, J. P. *et al.* Creation of a two-dimensional electron gas and conductivity switching of nanowires at the $LaAlO_3/SrTiO_3$ interface grown by 90 degrees off-axis sputtering. *Applied Physics Letters* **103**, (2013).

9 Sbrockey, N. M. *et al.* $LaAlO_3/SrTiO_3$ Epitaxial Heterostructures by Atomic Layer Deposition. *J Electron Mater* **41**, 819-823, (2012).

10 Nakagawa, N., Hwang, H. Y. & Muller, D. A. Why some interfaces cannot be sharp. *Nature Materials* **5**, 204-209, (2006).

11 Siemons, W. *et al.* Origin of charge density at $LaAlO_3$ on $SrTiO_3$ heterointerfaces: Possibility of intrinsic doping. *Phys Rev Lett* **98**, (2007).

12 Kalabukhov, A. *et al.* Effect of oxygen vacancies in the $SrTiO_3$ substrate on the electrical properties of the $LaAlO_3/SrTiO_3$ interface. *Physical Review B* **75**, (2007).

13 Qiao, L., Droubay, T. C., Kaspar, T. C., Sushko, P. V. & Chambers, S. A. Cation mixing, band offsets and electric fields at $LaAlO_3/SrTiO_3$(001) heterojunctions with variable La:Al atom ratio. *Surface Science* **605**, 1381-1387, (2011).

14 Willmott, P. R. *et al.* Structural basis for the conducting interface between $LaAlO_3$ and $SrTiO_3$. *Phys Rev Lett* **99**, (2007).

15 Sulpizio, J. A., Shahal Ilani, Patrick Irvin, and Jeremy Levy. Nanoscale Phenomena in Oxide Heterostructures. *Annu. Rev. Mater. Res.* **44**, 117-149, (2014).

16 Thiel, S., Hammerl, G., Schmehl, A., Schneider, C. W. & Mannhart, J. Tunable quasi-two-dimensional electron gases in oxide heterostructures. *Science* **313**, 1942-1945, (2006).

17 Liao, Y. C., Kopp, T., Richter, C., Rosch, A. & Mannhart, J. Metal-insulator transition of the $LaAlO_3$-$SrTiO_3$ interface electron system. *Phys Rev B* **83**, (2011).

18 Ben Shalom, M., Sachs, M., Rakhmilevitch, D., Palevski, A. & Dagan, Y. Tuning Spin-Orbit Coupling and Superconductivity at the $SrTiO_3/LaAlO_3$ Interface: A Magnetotransport Study. *Phys Rev Lett* **104**, (2010).
19 Caviglia, A. D. *et al.* Tunable Rashba Spin-Orbit Interaction at Oxide Interfaces. *Phys Rev Lett* **104**, (2010).
20 Reyren, N. *et al.* Superconducting interfaces between insulating oxides. *Science* **317**, 1196-1199, (2007).
21 Caviglia, A. D. *et al.* Electric field control of the $LaAlO_3/SrTiO_3$ interface ground state. *Nature* **456**, 624-627, (2008).
22 Koga, T., Nitta, J., Akazaki, T. & Takayanagi, H. Rashba spin-orbit coupling probed by the weak antilocalization analysis in InAlAs/InGaAs/InAlAs quantum wells as a function of quantum well asymmetry. *Phys Rev Lett* **89**, (2002).
23 Brinkman, A. *et al.* Magnetic effects at the interface between non-magnetic oxides. *Nature Materials* **6**, 493-496, (2007).
24 Ariando *et al.* Electronic phase separation at the LaAlO3/SrTiO3 interface. *Nat Commun* **2**, (2011).
25 Bert, J. A. *et al.* Direct imaging of the coexistence of ferromagnetism and superconductivity at the $LaAlO_3/SrTiO_3$ interface. *Nat Phys* **7**, 767-771, (2011).
26 Li, L., Richter, C., Mannhart, J. & Ashoori, R. C. Coexistence of magnetic order and two-dimensional superconductivity at $LaAlO_3/SrTiO_3$ interfaces. *Nature Physics* **7**, 762-766, (2011).
27 Lee, J. S. *et al.* Titanium d_{xy} ferromagnetism at the $LaAlO_3/SrTiO_3$ interface. *Nature Materials* **12**, 703-706, (2013).
28 Dikin, D. A. *et al.* Coexistence of Superconductivity and Ferromagnetism in Two Dimensions. *Phys Rev Lett* **107**, (2011).
29 Bi, F. *Scanning probe microscopy investigation of complex-oxide heterostructures* Ph.D. thesis, University of Pittsburgh, (2015).
30 Binnig, G. K. Atomic-Force Microscopy. *Physica Scripta* **T19a**, 53-54, (1987).
31 Klinov, D. & Magonov, S. True molecular resolution in tapping-mode atomic force microscopy with high-resolution probes. *Applied Physics Letters* **84**, 2697-2699, (2004).
32 Lauritsen, J. V. & Reichling, M. Atomic resolution non-contact atomic force microscopy of clean metal oxide surfaces. *Journal of Physics-Condensed Matter* **22**, (2010).
33 Kenton, B. J., Fleming, A. J. & Leang, K. K. Compact ultra-fast vertical nanopositioner for improving scanning probe microscope scan speed. *Review of Scientific Instruments* **82**, (2011).
34 Huo, F. W. *et al.* Polymer pen lithography. *Science* **321**, 1658-1660, (2008).
35 Xie, Y. W., Bell, C., Yajima, T., Hikita, Y. & Hwang, H. Y. Charge Writing at the $LaAlO_3/SrTiO_3$ Surface. *Nano Lett* **10**, 2588-2591, (2010).
36 Cen, C. *et al.* Nanoscale control of an interfacial metal-insulator transition at room temperature. *Nature Materials* **7**, 298-302, (2008).
37 Hellberg, D. Nitric oxide and cervical dysplasia. *Acta Obstet Gyn Scan* **88**, 1057-1057, (2009).
38 Rijnders, G. J. H. M., Koster, G., Blank, D. H. A. & Rogalla, H. In situ monitoring during pulsed laser deposition of complex oxides using reflection high energy electron diffraction under high oxygen pressure. *Applied Physics Letters* **70**, 1888-1890, (1997).

39 van der Marel, D., van Mechelen, J. L. M. & Mazin, I. I. Common Fermi-liquid origin of T-2 resistivity and superconductivity in n-type SrTiO3. *Physical Review B* **84**, (2011).
40 Zheng, G. F., Lu, W., Jin, S. & Lieber, C. M. Synthesis and fabrication of high-performance n-type silicon nanowire transistors. *Advanced Materials* **16**, 1890-+, (2004).
41 Cui, Y., Zhong, Z. H., Wang, D. L., Wang, W. U. & Lieber, C. M. High performance silicon nanowire field effect transistors. *Nano Lett* **3**, 149-152, (2003).
42 Willardson, R. K. & Beer, A. C. *Semiconductors and semimetals*. (Academic Press, 1966).
43 Landau, L. P. *Phy. Z.* **10**, (1936).
44 Kaveh, M. One-Dimensional Electron-Electron Scattering. *J Phys C Solid State* **13**, L611-L618, (1980).
45 Veazey, J. P. *et al.* Oxide-based platform for reconfigurable superconducting nanoelectronics. *Nanotechnology* **24**, (2013).
46 Cadden-Zimansky, P. & Chandrasekhar, V. Nonlocal Correlations in Normal-Metal Superconducting Systems. *Phys Rev Lett* **97**, 237003, (2006).
47 Seidel, J. *et al.* Conduction at domain walls in oxide multiferroics. *Nat Mater* **8**, 229-234, (2009).
48 Kane, C. L. & Mele, E. J. Quantum spin Hall effect in graphene. *Physical Review Letters* **95**, (2005).
49 Hughes, T. L., Bazaliy, Y. B. & Bernevig, B. A. Transport equations and spin-charge propagating mode in a strongly confined two-dimensional hole gas. *Physical Review B* **74**, (2006).
50 Valenzuela, S. O. & Tinkham, M. Direct electronic measurement of the spin Hall effect. *Nature* **442**, 176-179, (2006).
51 Garlid, E. S., Hu, Q. O., Chan, M. K., Palmstrom, C. J. & Crowell, P. A. Electrical Measurement of the Direct Spin Hall Effect in Fe/InxGa1-xAs Heterostructures. *Physical Review Letters* **105**, (2010).
52 Kato, Y. K., Myers, R. C., Gossard, A. C. & Awschalom, D. D. Observation of the Spin Hall Effect in Semiconductors. *Science* **306**, 1910-1913, (2004).
53 Abanin, D. A. *et al.* Giant Nonlocality Near the Dirac Point in Graphene. *Science* **332**, 328-330, (2011).
54 Fidkowski, L., Jiang, H. C., Lutchyn, R. M. & Nayak, C. Magnetic and superconducting ordering in one-dimensional nanostructures at the LaAlO3/SrTiO3 interface. *Physical Review B* **87**, (2013).
55 Arutyunov, K. Y., Auraneva, H. P. & Vasenko, A. S. Spatially resolved measurement of nonequilibrium quasiparticle relaxation in superconducting Al. *Physical Review B* **83**, (2011).
56 Hubler, F., Lemyre, J. C., Beckmann, D. & Von Lohneysen, H. Charge imbalance in superconductors in the low-temperature limit. *Physical Review B* **81**, (2010).
57 Tinkham, M. (Dover Publications, Mineola, N.Y., 2004).
58 Clarke, J. Experimental Observation of Pair-Quasiparticle Potential Difference in Nonequilibrium Superconductors. *Phys Rev Lett* **28**, 1363-1366, (1972).
59 Veazey, J. P. *et al.* Oxide-based platform for reconfigurable superconducting nanoelectronics. *Nanotechnology* **24**, 375201, (2013).
60 Russo, S., Kroug, M., Klapwijk, T. M. & Morpurgo, A. F. Experimental observation of bias-dependent nonlocal Andreev reflection (vol 95, pg 027002, 2005). *Physical Review Letters* **95**, (2005).

61 Melin, R. & Feinberg, D. Sign of the crossed conductances at a ferromagnet/superconductor/ferromagnet double interface. *Physical Review B* **70**, (2004).
62 Lin, X., Zhu, Z., Fauqué, B. & Behnia, K. Fermi surface of the most dilute superconductor. *Physical Review X* **3**, 021002, (2013).
63 Eagles, D. M. Possible pairing without superconductivity at low carrier concentrations in bulk and thin-film superconducting semiconductors. *Phys Rev* **186**, 456, (1969).
64 Schooley, J. F., Hosler, W. R. & Cohen, M. L. Superconductivity in semiconducting $SrTiO_3$. *Phys Rev Lett* **12**, 474-475, (1964).
65 Binnig, G., Baratoff, A., Hoenig, H. E. & Bednorz, J. G. Two-band superconductivity in Nb-doped $SrTiO_3$. *Phys Rev Lett* **45**, 1352-1355, (1980).
66 Hanson, R., Kouwenhoven, L. P., Petta, J. R., Tarucha, S. & Vandersypen, L. M. K. Spins in few-electron quantum dots. *Reviews of Modern Physics* **79**, 1217-1265, (2007).
67 Liang, W. J. *et al.* Fabry-Perot interference in a nanotube electron waveguide. *Nature* **411**, 665-669, (2001).
68 Kretinin, A. V., Popovitz-Biro, R., Mahalu, D. & Shtrikman, H. Multimode Fabry-Perot Conductance Oscillations in Suspended Stacking-Faults-Free InAs Nanowires. *Nano Lett* **10**, 3439-3445, (2010).
69 Cheng, G. *et al.* Electron pairing without superconductivity. *Nature* **521**, 196-199, (2015).
70 Oreg, Y., Refael, G. & von Oppen, F. Helical Liquids and Majorana Bound States in Quantum Wires. *Phys Rev Lett* **105**, 177002, (2010).
71 Kalisky, B. *et al.* Locally enhanced conductivity due to the tetragonal domain structure in $LaAlO_3/SrTiO_3$ heterointerfaces. *Nature Materials* **12**, 1091-1095, (2013).
72 Honig, M. *et al.* Local electrostatic imaging of striped domain order in $LaAlO_3/SrTiO_3$. *Nature Materials* **12**, 1112-1118, (2013).
73 Giamarchi, T. Theoretical framework for quasi-one dimensional systems. *Chem Rev* **104**, 5037-5055, (2004).
74 Thomas, K. J. *et al.* Possible spin polarization in a one-dimensional electron gas. *Phys Rev Lett* **77**, 135-138, (1996).
75 Vanwees, B. J. *et al.* Quantum Ballistic and Adiabatic Electron-Transport Studied with Quantum Point Contacts. *Physical Review B* **43**, 12431-12453, (1991).
76 Berggren, K. F., Roos, G. & Vanhouten, H. Characterization of Very Narrow Quasi-One-Dimensional Quantum Channels. *Physical Review B* **37**, 10118-10124, (1988).
77 van Weperen, I., Plissard, S. R., Bakkers, E. P. A. M., Frolov, S. M. & Kouwenhoven, L. P. Quantized Conductance in an InSb Nanowire. *Nano Lett* **13**, 387-391, (2013).
78 Daneshvar, A. J. *et al.* Enhanced g factors of a one-dimensional hole gas with quantized conductance. *Physical Review B* **55**, 13409-13412, (1997).
79 Graham, A. C. *et al.* Interaction effects at crossings of spin-polarized one-dimensional subbands. *Physical Review Letters* **91**, (2003).
80 Chang, J. W. *et al.* Quantum Electrical Transport in Mesoscopic LaAlO3/SrTiO3 Heterostructures. *Applied Physics Express* **6**, (2013).
81 Lee, S. W., Liu, Y. Q., Heo, J. & Gordon, R. G. Creation and Control of Two-Dimensional Electron Gas Using Al-Based Amorphous Oxides/SrTiO3 Heterostructures Grown by Atomic Layer Deposition. *Nano Lett* **12**, 4775-4783, (2012).
82 Lee, S. W., Heo, J. & Gordon, R. G. Origin of the self-limited electron densities at Al2O3/SrTiO3 heterostructures grown by atomic layer deposition - oxygen diffusion model. *Nanoscale* **5**, 8940-8944, (2013).

83 Chen, Y. Z. *et al.* A high-mobility two-dimensional electron gas at the spinel/perovskite interface of gamma-Al2O3/SrTiO3. *Nature Communications* **4**, (2013).
84 Martin, Y. & Wickramasinghe, H. K. Magnetic Imaging by Force Microscopy with 1000-a Resolution. *Applied Physics Letters* **50**, 1455-1457, (1987).
85 Ben Shalom, M., Ron, A., Palevski, A. & Dagan, Y. Shubnikov-De Haas Oscillations in SrTiO3/LaAlO3 Interface. *Phys Rev Lett* **105**, (2010).